Temperature-dependent phonon states of some ionic compounds by first principles calculations

SONG YUXI

Contents

Chapter 1

General introduction

1.1 Research background

Tremendous achievements have been made in the characterization and fabrication for diverse materials in the research field of materials science. However, experiments can be very challenging due to the expensive cost, and even be impossible at some extreme conditions. In addition to the necessary guidance for efficiently carrying out the experiments, the comprehensively understanding of the underlying mechanisms existing in variously interesting properties of the materials is also highly demanded. Thanks to the big leap in the computational algorithms and power, an abundant of the methodologies and numerical simulations have been established for the scientific research of the materials in parallel to the experiments. For example, the molecular dynamics (MD)-based calculations are widely used for understanding the movements of the atoms and molecules with an extra temperature or pressure condition given a classically dynamic evolution of a system [1]. Not only the computational complexity and cost but also the deficiency in describing the microscopic level of the electronic properties impede the applications of MD-based method to a large amount of complex and novel materials [2,3]. The first-principles based calculations within the framework of density functional theory (DFT) [4,5] are suitable for deriving the microscopic physical properties in the quantum mechanics principles, by which the accuracy of the calculated results is comparable to that of the experiment. The first-principles based methods are now practical in modern quantum physics fields such as the electronics [6,7], spintronics [8] and lattice dynamics [9], since they are straightforward and efficient for explaining the experimental results and very powerful for further designing the novel materials with desired physical properties.

Phonons are quantum mechanical properties of the collective excitations in a crystal, which are responsible for many lattice dynamical and thermal properties involved events such as the phase

transitions, the thermal expansion and the resistance to the heat transport [10]. Since phonons are the major heat carriers in semiconductors and insulators, it is critical to describe the atomic vibrations accurately for understanding the interesting phonon-driven phenomena, which is useful for predicting the thermodynamic stability of the materials and for assessing the related performance of the applications and devices [11]. To date, the first-principles phonon calculations become universal in computational materials science [12–21], especially universally applied with a harmonic approximation, which is simply assumed that the Taylor series of the crystal potential surface up to just the second-order derivative regarding the equilibrium atomic positions. Despite this approximation is successful for describing the non-interacting phonons and obtaining the well-defined harmonic phonon spectra, it alone produces the imaginary phonon frequencies in some highly anharmonic materials [22], and fails to explain many thermodynamic phenomena such as the finite phonon lifetimes and thermal transport involves the phonon-phonon interactions, and the temperature-dependent phonon properties originated from the lattice anharmonicity. The quasiharmonic approximation (QHA) is then adopted for calculating the thermodynamic properties depended on the crystal volume as a function of the temperature, which its implementations are generally based on the harmonic phonon properties. Even though QHA is well established and performed on many cases [15,23–25], it has limitations that a breakdown occur in those crystal structures dynamically unstable at 0 K since a lack of direct account for the temperature dependency, and moreover it is also inaccessible to any dynamical properties depended on the phonon scattering events [26–28].

To enhance the ability of the phonon calculations beyond the harmonic level, many efforts have been made to improve the numerical method by including the high-order anharmonic terms in the crystal potential expansion and treating them with, in general, the perturbative [29–41] or the nonperturbative [42–50] way. The perturbative theory is based on the restriction that the anharmonic effects are small enough to be a perturbation of the harmonic terms, where the phonon scattering process is dominated by the three-phonon interactions by introducing the third-order term [51–54]. For those compounds of which the perturbative condition is not satisfied, the anharmonic effects are better to be treated in a non-perturbative way such as the MD-based approach [55–61], where the potential surface can be accurately sampled at finite temperatures. The disadvantages of this method are computationally expensive and time-consuming since the accuracy depends on the length of the time interval. Moreover, it is inaccurate when dealing with the quantum zero-point motion due to the classical feature of this method. For example, Souvatzis *et al*. proposed the self-consistent ab initio lattice dynamics approach (SCAILD), which the atomic forces are computed by several atomic displacements generated by the classical thermal mean-square displacement matrix with the fixed vibrational amplitudes [62,63]. Later, an improved approach based on SCAILD where then the atomic displacements are generated using the full quantum mean-square thermal displacement matrix [64].

These approaches are conceptually based on the self-consistent phonon (SCP) theory formulated firstly and developed by Born and Hooton, where the anharmonic phonon frequencies are renormalized iteratively by computing the atomic forces generated by a collection of displaced configurations [65–69]. In this way, the effective harmonic force constants are obtained and consequently the self-consistent anharmonic phonon spectra are well defined. The temperature dependent effective potential (TDEP) constructed by Hellman *et al*., a fitting approach based on ab initio molecular dynamics (AIMD) simulations, provides a iterative way to extract the effective force constants at finite temperatures [57,58,70–74]. Furthermore, Errea *et al*. developed the stochastic self-consistent harmonic approximation (SSCHA) is also a SCP-based approach in which the free energy is minimized regarding an initially trial harmonic density matrix [46–48,75]. Recently, Tadano *et al*. proposed a SCP-based approach where the quartic-order force constants are included in the renormalized process [62,76,77] and can be accurately estimated through an efficient method of compressed sensing lattice dynamics (CSLD) [78–80]. The impact of the high-order anharmonic effects such as the quartic anharmonicity have been considered and incorporated into the lattice dynamics and thermal transport properties [81–88]. In spite of the formalism for the quartic anharmonicity has been well constructed [89–92], the issues of the accuracy and complexity of the numerical process still hinders the expansion to the anharmonic terms higher than the third order. Therefore, to develop a robust and efficient approach is a significant subject in lattice dynamical calculations especially when systematically investigating the numerous materials and thoroughly exploring the unknown materials with target properties.

Over the past several decades, the rocksalt-type binary compounds, which are mostly semiconductors and insulators of the group I-VII and II-VI, have been attracted both scientific and technological attentions [92–107]. In a rocksalt structure, the cations and anions, which locate in their respective face-centered cubic lattice, form the octahedral blocks where each ion has a coordination number of six. These compounds with a simple structure display various mechanical, electronic, optical and thermal properties, which are widely utilized in many scientific and technical applications. Despite substantial achievements on the thermodynamics of the rocksalt binary structures, several questions still open. For example, according to the previous study [109,110], the conventional first-principles phonon calculations are insufficient to describe the phonon dispersion and related thermal properties of the rocksalt-type sodium chloride at room temperature, since the thermal expansion estimated by the quasiharmomic approximation is much larger than the measured one. The failure of the quasiharmonic approximation is mainly due to the improper treatment of the lattice anharmonicity arising from the high temperature. On the other hand, the prediction for the lattice thermal conductivity, which is crucial for evaluating the performance of the modern devices such as the thermoelectric generators and converters and the photovoltaic cells, should be improved with a higher precision [111–

113]. Some theoretical studies proposed that the quartic and even higher anharmonicity should be considered into the phonon frequencies, lifetimes and lattice thermal conductivities for these [109,110,114]. These methods indeed lead to a good match between the calculated data and the measurements, which are useful for understating the impact of strong anharmonic on the lattice dynamical and thermal properties of the rocksalt binary compounds while the drawback is the apparently computational cost.

The ABX_3-type perovskite family has been extensively investigated owing to its outstanding physical and chemical properties such as distinguished photovoltaic effect, high dielectric constant, ferroelectric and ferromagnetic polarization, piezoelectricity and superconductivity, which possess shining prospects in diverse applications and devices such as memories, sensors, capacitors and other related energy converters [115–117]. The perovskite structure was firstly considered to draw many attentions in scientific field thanks to the discovery of calcium titanate ($CaTiO_3$) by Perovski. Generally, the perovskite materials share a common chemical formula of ABX_3, where A and B are the metal cations and X is the anion usually oxides or halogens, respectively. Each central cation B surrounded with six anions X in octahedral coordination forms the basic BX_6 octahedral in the ABX_3 structure. These BX_6 octahedral blocks are linked in a corner-sharing structural configuration, where the cation A is located in the space between two BX_6 octahedrons to maintain the charge neutrality of the structure. Among the perovskites, the oxide-based compounds have attracted the huge attentions for the diversely novel devices benefited from their excellent ferroelectric, ferromagnetic, piezoelectric, thermoelectric and photocatalytic characteristics of these materials [118–120]. In the perovskite-type oxides ABO_3, the cation A is usually an alkaline- or rare-earth element, and the cation B is 3*d*, 4*d*, and 5*d* transition metal elements, which indeed allows the development of various engineered materials by manipulate different cations embedded in the structure. A wide variety of distorted structural configurations in perovskite oxides can be observed regarding the combinations of elements and the phase transitions at finite temperatures [121,122]. Among these variants, the cubic phase of perovskite oxides is generally stable at high temperature. Some of the perovskite oxides with an ideal cubic structure undergo a phase transition away from the ideal one when the temperature decreases since the occurrence of the atomic displacements or the octahedral distortions, while some of the perovskite oxides remain the cubic stability without any structural distortions in spite of the low temperature.

Taking barium titanate ($BaTiO_3$) as an example, its bulk structure possess one of four crystal symmetries with a phase sequence of cubic, tetragonal, orthorhombic and rhombohedral crystal structure from the high to low temperature [123]. All of these phases except high temperature cubic phase exhibit the ferroelectricity. Another case is strontium titanate ($SrTiO_3$) where the A cation of barium is then replaced with strontium, which consequently has a completely different phase diagram

regarding temperature. Previous research have shown that $SrTiO_3$, an intrinsic quantum paraelectric, is stable with the cubic phase at high temperature [124–126]. With decreasing temperature below 105 K, it undergoes a structural phase transition to a tetragonal structure due to the rotation of the oxygen octahedral block along the *c*-axis. However, the existence of zero-point quantum fluctuations at very low temperatures suppresses the long-range ferroelectric order temperatures and forces the structure remains paraelectric, which makes it so-called incipient ferroelectric.

The phase transition characteristics with respect to the finite temperatures for the perovskite oxides distinctly vary by the compounds. It is of great importance to find the relationship between the structural stability and the temperature among different compounds. Up to now, with the development of the first-principles electronic and phonon calculations, the qualitatively and quantitatively descriptions of various properties become much easier, which indeed provides a guidance for the materials synthesis and fabrications. The first-principles calculations are considered accurate in describing the intrinsic properties of materials at ground state. When the structural configuration is stable at 0 K, there is no problem to directly utilize this ground-state calculation tool. However, in the first-principles phonon calculations, most of the cubic perovskite oxides such as $BaTiO_3$ and $SrTiO_3$, which are mechanically and dynamically unstable at 0 K, show the imaginary phonon branches in dispersion curves. In addition, the lattice thermal conductivity is essential for defining conversion efficiency of a thermoelectric device. Unfortunately, it is less well studied for the cubic perovskite structures due to the limited performance of the first-principles harmonic phonon calculations at high temperatures. Only a few of theoretically calculated data obstruct the comprehensive knowledge of the various thermodynamic properties observed experimentally. Therefore, for those materials whose room- or high-temperature phase is not the dynamically stable structure in the ground state, it is urgent to improve the numerical approach by incorporating the finite-temperature effects into the phonon calculations better to describe their lattice dynamical properties. Furthermore, it is useful to develop a robust and efficient way for a large amount of perovskite compounds, in order to access to their lattice thermal conductivities, which motivate us to explore the advanced materials with the tunable and desirable properties.

1.2 Outline of thesis

In Chapter 2, the theory of quantum mechanics such as the evolution of many-body Schrödinger equations to the single-particle equations are introduced. The theory of lattice dynamics are elaborated, including the harmonic and anharmonic phonon properties, and the thermal transport properties. For example, the concept of phonon, the phonon band structures and phonon density of states, the lattice

thermal expansion, Helmholtz free energy and the lattice thermal conductivity, etc. A series of related approximation for dealing the above problems are adopted such as the adiabatic approximation, single-particle approximation, harmonic approximation, quasihamornic approximation and single-mode relaxation time approximation, *etc*. In terms of the numerical approach, one of a routine choice is solving the Kohn-Sham equations within the framework of density functional theory as implemented in Vienna *ab initio* simulation package (VASP) [127–130]. After obtaining the forces from the electronic calculations, the harmonic and anharmonic phonon properties, and the lattice thermal conductivity can be further obtained by first-principles lattice dynamics calculations as implemented in Phonopy [9] and Phono3py [40] packages, which are numerical approaches to solve the vibrational problems at the atomic scale. Apart from the fundamental theory of the phonon calculations, an improved method of temperature-dependent phonon calculations was developed since the conventional harmonic phonon calculations are inadequate for the highly anharmonic structures and the failure of correctly describing the phonon properties at finite temperatures to agree with the measured data. Not only the physical theory but also the mathematical process are introduced, and the whole workflow are presented in order to make a clear understanding about the process of this simple and accurate method.

In Chapter 3, in order to test the validity and applicability of the temperature-dependent phonon approach as mentioned above, the calculations of the 32 rocksalt compounds, including the alkali halides comprised of the group I-VII elements and the alkaline-earth chalcogenides comprised of the group II-VI, are performed within the proposed method. To test the robustness of the phonon calculations, the calculations with different factors such as the lattice parameters, exchange correlation potentials and sampling mesh in Brillouin zone, which may influence the phonon calculations, are also conducted. After the determination of all calculated parameters, the phonon band structures and densities of states, and the lattice thermal conductivities of all these rocksalt compounds are predicted by the phonon calculations. In particular, the results of the lattice thermal conductivity are discussed through the frequency dependence of the mode-dependent lattice thermal conductivity, and the phonon lifetime and scattering rates due to the anharmonic phonon-phonon interactions. It is found that a good agreement between the calculated results and available experimental data, which identifies the validity of our temperature dependence of phonon calculations. The analyses of the high-throughput results provide a deep insight to investigate systematically the phonon and thermal transport properties of the materials, which thereby offer a powerful approach and fundamental guidance for experiment to explore more and more new thermal materials with desired properties.

In Chapter 4, the temperature-dependent phonon calculations are performed on the cubic perovskite-type oxides ABO_3 compounds, where the cation A and B are alkaline earth and transition metals. It is urgent to systematically investigate their lattice dynamical and thermal properties, since the breakdown

of the harmonic calculations may happen when computing the phonon properties of the structure with a high-temperature cubic phase, which hinders the prediction of their thermodynamic properties. Through the temperature-dependent phonon approach introduced in this work, the effective force constants including the temperature information are generated, which as a consequent the self-consistent phonon band structures and density of states are obtained. In particular, for those dynamically stable compounds at finite temperatures, their lattice thermal conductivities at finite temperatures can also be calculated with well-converged second- and third-order forces constants. The good match between calculated and measured phonon frequencies and lattice thermal conductivities further demonstrate the universal applicability of the temperature-dependent phonon calculations to a wide type of the structures for evaluating their lattice dynamical and thermodynamics properties at finite temperatures.

In Chapter 5, a general conclusion is given for all the calculated results and discussions in this work.

Finally, all the references and the final acknowledgement are presented in the end of this thesis.

Chapter 2

Temperature-dependent phonon calculations

2.1 Introduction

2.1.1 Adiabatic approximation

In a crystal, the motion of all ions and electrons in a large supercell can be studied within a unit cell by considering the periodic boundary conditions taking advantage of the translational lattice symmetry, which reduces the problem to the dynamics of atoms in a relatively small system. However, it should be further simplified by other approximations. In quantum mechanical theory [131,132], the Hamiltonian of a system of ions and electrons obtained from a many-body Schrödinger equation, contains the kinetic and potential energy due to interactions between particles,

$$\mathcal{H} = -\sum_{I}\frac{\hbar^2}{2M_I}\nabla_{\boldsymbol{R}_I}^2 - \sum_{I}\frac{\hbar^2}{2m_i}\nabla_{\boldsymbol{r}_i}^2 - \sum_{iI}\frac{Z_I\,e^2}{|\boldsymbol{R}_I-\boldsymbol{r}_i|} + \frac{1}{2}\sum_{ij(i\neq j)}\frac{e^2}{|\boldsymbol{r}_i-\boldsymbol{r}_j|} + \frac{1}{2}\sum_{IJ(I\neq J)}\frac{Z_I Z_J\,e^2}{|\boldsymbol{R}_I-\boldsymbol{R}_J|} \quad (2.1)$$

In Eqn. (2.1), $\boldsymbol{R}_I$ and $\boldsymbol{r}_i$ are the positions of ions and electrons, e is the elementary charge, $\hbar$ is Planck's constant divided by 2π, M_I and m_i are the mass of ions and electrons. The first and second term are kinetic energy of the ions and electrons, respectively. The third, fourth and fifth term are the ionic potential experienced by every electron, the potential caused by repulsion between the electrons, and the potential caused by repulsion between the ions.

Normally, the ions are moving slowly and the electrons are instantaneously responding to any moment of the ionic states due to the huge difference of the mass between these two kinds of particles, leading to the former behave like the classical particles. Therefore, it is available that the motion of the ions and the electrons can be separately considered, which is known as adiabatic approximation.

In fact, the motion of electrons is determined by the equilibrium state of the ions, meanwhile the motion of the ions is dependent of the potential field generated by surrounding electrons. With motionlessness of the ions, the kinetic energy of the ions can be omitted and the potential energy between ions can be a constant. Then, Eqn. (2.1) can be simplified as,

$$\mathcal{H} = -\sum_{I} \frac{\hbar^2}{2m_i} \nabla_{\boldsymbol{r}_i}^2 - \sum_{iI} \frac{Z_I\, e^2}{|\boldsymbol{R}_I - \boldsymbol{r}_i|} + \frac{1}{2} \sum_{ij(i\neq j)} \frac{e^2}{|\boldsymbol{r}_i - \boldsymbol{r}_j|} = \mathcal{T} + \mathcal{V} \tag{2.2}$$

where $\mathcal{T}$ and $\mathcal{V}$ are kinetic and potential energy of the system in this approximation, respectively.

2.1.2 Single-particle description

It is extremely hard to solve a many-body Schrödinger equation though it is simplified as shown in Eqn. (2.2), since the wavefunctions involving complex interactions between particles [131,132]. Hartree *et al*. proposed that the state of a system is assumed as a non-interacting way, which leads to the wavefunctions Ψ is separated into a series of the individual electronic states,

$$\Psi(\boldsymbol{r}_1, \boldsymbol{r}_2, \ldots, \boldsymbol{r}_N) = \phi_1(\boldsymbol{r}_1)\, \phi_1(\boldsymbol{r}_2) \cdots \phi_1(\boldsymbol{r}_N) \tag{2.3}$$

where $\phi_i(\boldsymbol{r}_i)$ is the *i*-th single electronic state in site $\boldsymbol{r}_i$. The single-particle equations then can be constructed, which is called the Hartree approximation,

$$\left[-\frac{\hbar \nabla_{\boldsymbol{r}}^2}{2m_i} + V_{ion}(\boldsymbol{r}) + e^2 \sum_{ij\,(i\neq j)} \left\langle \phi_j \left| \frac{1}{|\,\boldsymbol{r} - \boldsymbol{r}'|} \right| \phi_j \right\rangle \right] \phi_i(\boldsymbol{r}) = \epsilon_i\, \phi_i(\boldsymbol{r}) \tag{2.4}$$

However, the simple treatment of wavefunctions expressed in Eqn. (2.3) is not appropriate for indistinguishable particles, for which the antisymmetry of the electronic wavefunctions in quantum mechanics is ignored by Hartree approximation. Therefore, representing the wavefunctions of system in a form of Slater determinant,

$$\Psi(\boldsymbol{r}_1, \boldsymbol{r}_2, \ldots, \boldsymbol{r}_N) = \frac{1}{\sqrt{N!}} \begin{vmatrix} \phi_1(\boldsymbol{r}_1) & \phi_1(\boldsymbol{r}_2) & \cdots & \phi_1(\boldsymbol{r}_N) \\ \phi_2(\boldsymbol{r}_1) & \phi_2(\boldsymbol{r}_2) & \cdots & \phi_2(\boldsymbol{r}_N) \\ \vdots & \vdots & \ddots & \vdots \\ \phi_N(\boldsymbol{r}_1) & \phi_N(\boldsymbol{r}_2) & \cdots & \phi_N(\boldsymbol{r}_N) \end{vmatrix} \tag{2.5}$$

By establishing the variational principle, the single-particle equations can be improved in the Hartree-Fock approximation,

$$\left[-\frac{\hbar}{2m_i}\nabla_{\boldsymbol{r}}^2 + V_{ion}(\boldsymbol{r}) + V_i^{HF}(\boldsymbol{r})\right]\phi_i(\boldsymbol{r}) = \epsilon_i\,\phi_i(\boldsymbol{r}) \tag{2.6}$$

where $V_i^{HF}(\boldsymbol{r})$ is consisted of Hartree potential $V_i^{H}(\boldsymbol{r})$ and exchange potential $V_i^{X}(\boldsymbol{r})$,

$$V_i^{HF}(\boldsymbol{r}) = V_i^{H}(\boldsymbol{r}) + V_i^{X}(\boldsymbol{r}) = e^2\int\frac{\rho(\boldsymbol{r}') - \rho_i(\boldsymbol{r}')}{|\boldsymbol{r}-\boldsymbol{r}'|}d\boldsymbol{r}' - e^2\int\frac{\rho_i^X(\boldsymbol{r},\boldsymbol{r}')}{|\boldsymbol{r}-\boldsymbol{r}'|}d\boldsymbol{r}' \tag{2.7}$$

with total densities $\rho(\boldsymbol{r})$, single electronic densities $\rho_i(\boldsymbol{r})$ and single electronic exchange densities $\rho_i^X(\boldsymbol{r},\boldsymbol{r}')$,

$$\begin{aligned}\rho_i(\boldsymbol{r}) &= |\phi_i(\boldsymbol{r})|^2\\ \rho(\boldsymbol{r}) &= \sum_i \rho_i(\boldsymbol{r})\\ \rho_i^X(\boldsymbol{r},\boldsymbol{r}') &= \sum_{i\neq j}\frac{\phi_i(\boldsymbol{r}')\,\phi_i^*(\boldsymbol{r})\,\phi_j(\boldsymbol{r})\,\phi_j^*(\boldsymbol{r}')}{\phi_i(\boldsymbol{r})\,\phi_i^*(\boldsymbol{r})}\end{aligned} \tag{2.8}$$

In this way, the quantum mechanical exchange and correlation interactions between electrons are included.

Furthermore, Kohn *et al*. developed a new approach exactly treating the single-particle equations instead of using the trial wavefunctions in Hartree-Fock approximations, namely Density Functional Theory (DFT) [4,5]. In this method, the total energy of a system can be defined as a function of the charge density $\rho(\boldsymbol{r})$ and the single-particle equations, so-called Kohn-Sham equations, written as

$$\left[-\frac{\hbar}{2m_i}\nabla_{\boldsymbol{r}}^2 + V_{eff}\big(\boldsymbol{r},\rho(\boldsymbol{r})\big)\right]\phi_i(\boldsymbol{r}) = \epsilon_i\,\phi_i(\boldsymbol{r}) \tag{2.9}$$

where ϵ_i is the orbital energy of the corresponding Kohn–Sham orbital ϕ_i. The effective potential energy V_{eff} consists of the external potential, the Coulomb interaction and the exchange-correlation potential,

$$V_{eff}\big(\boldsymbol{r},\rho(\boldsymbol{r})\big) = V(\boldsymbol{r}) + e^2\int\frac{\rho(\boldsymbol{r}')}{|\boldsymbol{r}-\boldsymbol{r}'|}d\boldsymbol{r}' + \frac{\delta\,E^{XC}[\rho(\boldsymbol{r})]}{\delta\,\rho(\boldsymbol{r})} \tag{2.10}$$

By dealing with the unknown exchange-correlation functional within some approximations, the Kohn-Sham equations are solved iteratively, which results in the self-consistent density, orbitals and the minimum of the total energy for the electronic ground state.

2.2 Lattice dynamics

2.2.1 Harmonic approximation

Here, we restrict the discussion to a two-body interaction where the interatomic potential $U(\boldsymbol{R})$ is a function of the interatomic distance $\boldsymbol{R}$ between a pair as shown in Figure 2.1. Each atom in the ideal crystalline solid experiences the same potential due to the other atoms in the material. It is found that the location of the minimum of the potential well is the equilibrium position of the atom. In this potential, individual atoms will vibrate about their equilibrium positions with the amplitude of their vibration being determined by the total energy [133].

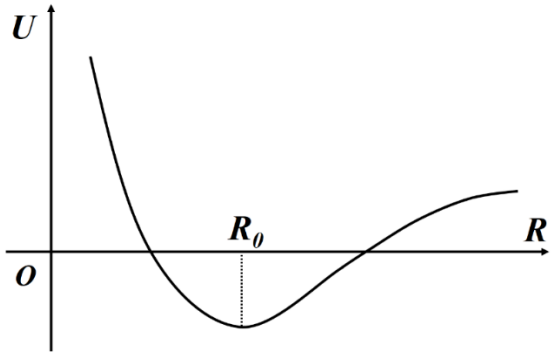

Figure 2.1. A schematic of interatomic potential U with respect to the interatomic distance $\boldsymbol{R}$. $\boldsymbol{R}_0$ is the distance between two atoms in their equilibrium positions, which leads to the minimum of the potential energy.

It is assumed that the atoms vibrate around their positions $\boldsymbol{R}_0(\boldsymbol{l\kappa})$ with displacements $\boldsymbol{u}(\boldsymbol{l\kappa}) = \boldsymbol{R}(\boldsymbol{l\kappa}) - \boldsymbol{R}_0(\boldsymbol{l\kappa})$, where $\boldsymbol{l}$ and $\boldsymbol{\kappa}$ are the labels of the unit cells and the atoms in that unit cell. Then, the total potential energy V can be demonstrated as an analytic function of the displacements $\boldsymbol{u}(\boldsymbol{l\kappa})$ in a Taylor expansion,

$$V = V_0 + V_1 + V_2 + \cdots$$

$$= V_0 + \sum_{\boldsymbol{l\kappa}} \sum_{\alpha} \Phi_{\alpha}(\boldsymbol{l\kappa})\, u_{\alpha}(\boldsymbol{l\kappa}) + \frac{1}{2} \sum_{\boldsymbol{l\kappa},\boldsymbol{l'\kappa'}} \sum_{\alpha\beta} \Phi_{\alpha\beta}(\boldsymbol{l\kappa}, \boldsymbol{l'\kappa'})\, u_{\alpha}(\boldsymbol{l\kappa})\, u_{\beta}(\boldsymbol{l'\kappa'}) + \cdots \qquad (2.11)$$

where α, β, … denote the Cartesian indices. V_0 is an arbitrary constant, which can be ignored in dynamical calculations for convenience. V_1 vanishes because of the zero-value forces at the equilibrium state and the 0 K. $\Phi_\alpha(\boldsymbol{l\kappa})$ and $\Phi_{\alpha\beta}(\boldsymbol{l\kappa}, \boldsymbol{l'\kappa'})$ are the first and second order force constants, respectively,

$$\Phi_{\alpha\beta}(\boldsymbol{l\kappa}, \boldsymbol{l'\kappa'}) = \left. \frac{\partial^2 V}{\partial u_\alpha(\boldsymbol{l\kappa})\, \partial u_\beta(\boldsymbol{l'\kappa'})} \right|_0 \tag{2.12}$$

Furthermore, the potential energy can be defined as consists of the only second order term but higher order terms, which is known as harmonic approximation, and Eqn. (2.11) then can be simplified as

$$V_{harm} = \frac{1}{2} \sum_{\boldsymbol{l\kappa}, \boldsymbol{l'\kappa'}} \sum_{\alpha\beta} \Phi_{\alpha\beta}\,(\boldsymbol{l\kappa}, \boldsymbol{l'\kappa'})\, u_\alpha(\boldsymbol{l\kappa})\, u_\beta(\boldsymbol{l'\kappa'}) \tag{2.13}$$

Once the crystal potential is obtained, the dynamics of the atomic degrees of freedom are determined by the quantum Hamiltonian composed of kinetic energy T and harmonic potential energy V_{harm},

$$H_{harm} = T + V_{harm} = \sum_{i=1}^{N} \sum_{s=1}^{3} \frac{p_{i,s}^2}{2M_i} + \frac{1}{2} \sum_{\boldsymbol{l\kappa}, \boldsymbol{l'\kappa'}} \sum_{\alpha\beta} \Phi_{\alpha\beta}\,(\boldsymbol{l\kappa}, \boldsymbol{l'\kappa'})\, u_\alpha(\boldsymbol{l\kappa})\, u_\beta(\boldsymbol{l'\kappa'}) \tag{2.14}$$

where M_i is the mass of i-th atom $(\boldsymbol{l}, \boldsymbol{\kappa})$ in the supercell containing N atoms, $s = \{\alpha, \beta, \gamma\}$ is the Cartesian index, and $p_{i,s}$ is the momentum operator of the i-th atom along the direction s. The equation of motion now can be written as

$$m_{\boldsymbol{\kappa}}\, \ddot{u}_\alpha(\boldsymbol{l\kappa}) = -\sum_{\boldsymbol{l'\kappa'}\beta} \Phi_{\alpha\beta}\,(\boldsymbol{l\kappa}, \boldsymbol{l'\kappa'})\, u_\beta(\boldsymbol{l'\kappa'}) \tag{2.15}$$

Consider that lattice translational symmetry and infinitesimal translational invariance of the force constants, Eqn. (2.15) can be rewritten as

$$m_{\boldsymbol{\kappa}}\, \ddot{u}_\alpha(\boldsymbol{l\kappa}) = -\sum_{\boldsymbol{l'\kappa'}\beta} \Phi_{\alpha\beta}\,(\boldsymbol{0\kappa}, \boldsymbol{l'\kappa'})\, u_\beta(\boldsymbol{l'\kappa'}) \tag{2.16}$$

The trial solution of Eqn. (2.16) can be set as

$$u_\alpha(\boldsymbol{l\kappa}) = \frac{1}{\sqrt{m_{\boldsymbol{\kappa}}}} \sum_{\boldsymbol{q}} U_\alpha\,(\boldsymbol{\kappa}, \boldsymbol{q})\, e^{i[\boldsymbol{q} \cdot \boldsymbol{R}(\boldsymbol{l}) - \omega t]} \tag{2.17}$$

where $\boldsymbol{q}$ and $\boldsymbol{R}(\boldsymbol{l\kappa})$ are the wave vector and the position vector of the unit cell $\boldsymbol{l}$, respectively. Applying Eqn. (2.17) to Eqn. (2.16) leads to

$$\omega^2 U_\alpha(\boldsymbol{\kappa}, \boldsymbol{q}) = \sum_{\kappa'\beta} D_{\alpha\beta}\,(\boldsymbol{\kappa\kappa'}, \boldsymbol{q})\; U_\beta(\boldsymbol{\kappa'}, \boldsymbol{q}) \tag{2.18}$$

with

$$D_{\alpha\beta}(\boldsymbol{\kappa\kappa'}, \boldsymbol{q}) = \frac{1}{\sqrt{m_{\boldsymbol{\kappa}} m_{\boldsymbol{\kappa'}}}} \sum_{\boldsymbol{l'}} \Phi_{\alpha\beta}\,(\boldsymbol{0\kappa}, \boldsymbol{l'\kappa'})\; e^{i\boldsymbol{q}\cdot\boldsymbol{R}(\boldsymbol{l'})} \tag{2.19}$$

Note that $\boldsymbol{D}$ is Hermitian and its eigenvalues $\omega_{\boldsymbol{q}j}^2$ are real. By solving Eqn. (2.18), we can get $3n_a$ eigenvalues $\omega_{\boldsymbol{q}j}^2$ with eigenvectors $\boldsymbol{e}_{\boldsymbol{q}j}$, where n_a is the number of atoms in a unit cell and j = 1, 2, … , $3n_a$ is the band index. The components of eigenvectors are orthonormal and complete as demonstrated in Eqn. (2.20) and Eqn. (2.21), respectively,

$$\sum_{\boldsymbol{\kappa\alpha}} {e_{\boldsymbol{qj}}^{\boldsymbol{\kappa\alpha}}}^{*}\, e_{\boldsymbol{qj}}^{\boldsymbol{\kappa\alpha}} = \delta_{jj'} \tag{2.20}$$

$$\sum_{j} {\boldsymbol{e}_{\boldsymbol{qj}}^{\boldsymbol{\kappa'\beta}}}^{*}\, \boldsymbol{e}_{\boldsymbol{qj}}^{\boldsymbol{\kappa\alpha}} = \delta_{\alpha\beta}\delta_{\boldsymbol{\kappa\kappa'}} \tag{2.21}$$

Therefore, Eqn. (2.18) can be rewritten as

$$\omega_{\boldsymbol{q}j}^2\; e_{\boldsymbol{qj}}^{\boldsymbol{\kappa\alpha}} = \sum_{\boldsymbol{\kappa'\beta}} D_{\alpha\beta}^{\boldsymbol{\kappa\kappa'}}(\boldsymbol{q})\, e_{\boldsymbol{qj}}^{\boldsymbol{\kappa'\beta}} \tag{2.22}$$

Normally, $\boldsymbol{e}_{\boldsymbol{q}j}$ denotes the vibration of the atom with the vibrational mode $(\boldsymbol{q}, j)$, and it is normalized as $\sum_{\alpha\boldsymbol{\kappa}} \left|e_{\boldsymbol{qj}}^{\boldsymbol{\kappa\alpha}}\right|^2 = 1$, which represents the collective motion of all atoms.

2.2.2 Phonon calculations

Density functional theory gives one access to the crystal potential of a system, which the harmonic force constants from the second derivatives of the crystal energy with respect to atomic displacements can be easily obtained by the implementation force calculations [132,133]. Forces acting on the atoms are given by the expectation value of the gradient of the electronic Hamiltonian in the ground state,

$$\boldsymbol{f}_I = -\left\langle \Psi_0 \left| \frac{\partial \mathcal{H}}{\partial \boldsymbol{R}_I} \right| \Psi_0 \right\rangle \tag{2.23}$$

This is so-called Hellmann-Feynman force. Consider that an atom is displaced and the force in harmonic approximation will act on this atom as followings,

$$f_\alpha(\boldsymbol{l\kappa}) = -\frac{\partial V}{\partial u_\alpha(\boldsymbol{l\kappa})} = -\sum_{\boldsymbol{l'\kappa'}\beta} \Phi_{\alpha\beta}(\boldsymbol{l\kappa}, \boldsymbol{l'\kappa'})\, u_\beta(\boldsymbol{l'\kappa'}) \tag{2.24}$$

and Eqn. (2.4) becomes

$$\Phi_{\alpha\beta}(\boldsymbol{l\kappa}, \boldsymbol{l'\kappa'}) = \frac{\partial^2 V}{\partial u_\alpha(\boldsymbol{l\kappa})\, \partial u_\beta(\boldsymbol{l'\kappa'})} = -\frac{\partial f_\beta(\boldsymbol{l'\kappa'})}{\partial u_\alpha(\boldsymbol{l\kappa})} \tag{2.25}$$

which represents the negative force on atom $(\boldsymbol{l}, \boldsymbol{\kappa})$ along the direction α is caused by the displacement of atom $(\boldsymbol{l'}, \boldsymbol{\kappa'})$ along the direction β. Normally, the force on each atom in a unit cell will be zero when system in an equilibrium state, whereas the net force exists when atoms vibrate. Therefore, the phonon frequencies of different normal modes defined in Eqn. (2.22) can be obtained after the force constants and dynamical matrix are clearly understood.

Typically, the periodicity of the system can be clearly demonstrated the Fourier space. It is appropriate for the displacement $\boldsymbol{u}$ and momentum $\boldsymbol{p}$ in Hamiltonian expressed in the Fourier transform to be represented as a function of the normal phonon modes with the wave vector $\mathbf{q}$ instead of the real-space coordinates of atoms. The number of normal phonon modes is same as the number of particles.

$$\boldsymbol{u}(\boldsymbol{l\kappa}) = \frac{1}{\sqrt{\Omega}} \sum_{\boldsymbol{q}} \mathcal{Q}_{\boldsymbol{q}}(\boldsymbol{\kappa})\, e^{i\boldsymbol{q}\cdot\boldsymbol{l}} \tag{2.26}$$

$$\boldsymbol{p}(\boldsymbol{l\kappa}) = \frac{1}{\sqrt{\Omega}} \sum_{\boldsymbol{q}} \Pi_{\boldsymbol{q}}(\boldsymbol{\kappa})\, e^{-i\boldsymbol{q}\cdot\boldsymbol{l}} \tag{2.27}$$

where Ω, $\mathcal{Q}$ and Π are the volume of the crystal, normal coordinate operators of $\boldsymbol{u}$ and $\boldsymbol{p}$, respectively. Meanwhile, we can obtain the following derivations,

$$\mathcal{Q}_{\boldsymbol{q}}^{\dagger}(\boldsymbol{\kappa}) = \mathcal{Q}_{-\boldsymbol{q}}(\boldsymbol{\kappa}) = \frac{1}{\sqrt{\Omega}} \sum_{\boldsymbol{l}} \boldsymbol{u}(\boldsymbol{l\kappa})\, e^{i\boldsymbol{q}\cdot\boldsymbol{l}} \tag{2.28}$$

$$\Pi_{\boldsymbol{q}}^{\dagger}(\boldsymbol{\kappa}) = \Pi_{-\boldsymbol{q}}(\boldsymbol{\kappa}) = \frac{1}{\sqrt{\Omega}} \sum_{\boldsymbol{l}} \boldsymbol{p}(\boldsymbol{l}\boldsymbol{\kappa})\, e^{-i\boldsymbol{q}\cdot\boldsymbol{l}} \tag{2.29}$$

In addition, by utilizing second quantization technique, the Hamiltonian in (2.14) can be rewritten as,

$$H_{harm} = \sum_{\boldsymbol{q},j} \hbar\omega_{\boldsymbol{q}j} \left(b_{\boldsymbol{q}j}^{\dagger}\, b_{\boldsymbol{q}j} + \frac{1}{2} \right) \tag{2.30}$$

where j, $b_{\boldsymbol{q}j}$ and $b_{\boldsymbol{q}j}^{\dagger}$ denotes the band index, boson creation and annihilation operator, respectively,

$$b_{\boldsymbol{q}j} = \sqrt{\frac{m_{\boldsymbol{\kappa}}\omega_{\boldsymbol{q}j}}{2\hbar}} \left(\mathcal{Q}_{\boldsymbol{q}j} + \frac{i}{m_{\boldsymbol{\kappa}}\omega_{\boldsymbol{q}j}} \Pi_{-\boldsymbol{q}j} \right) \tag{2.31}$$

$$b_{\boldsymbol{q}j}^{\dagger} = \sqrt{\frac{m_{\boldsymbol{\kappa}}\omega_{\boldsymbol{q}j}}{2\hbar}} \left(\mathcal{Q}_{-\boldsymbol{q}j} - \frac{i}{m_{\boldsymbol{\kappa}}\omega_{\boldsymbol{q}j}} \Pi_{\boldsymbol{q}j} \right) \tag{2.32}$$

Note that the polarization vector $e_{\boldsymbol{q}j}^{\boldsymbol{\kappa}}$ satisfies the orthonormality shown in Eqn. (2.20), is introduced in $\mathcal{Q}_{\boldsymbol{q}}(\boldsymbol{\kappa})$ and $\Pi_{\boldsymbol{q}}(\boldsymbol{\kappa})$ and the relationship between $\mathcal{Q}_{\boldsymbol{q}}(\boldsymbol{\kappa})$ and $\mathcal{Q}_{\boldsymbol{q}j}$, $\Pi_{\boldsymbol{q}}(\boldsymbol{\kappa})$ and $\Pi_{\boldsymbol{q}j}$ are shown in Eqn. (2.33) and Eqn. (2.34), respectively,

$$\mathcal{Q}_{\boldsymbol{q}j} = \sum_{\boldsymbol{\kappa}} \sqrt{m_{\boldsymbol{\kappa}}}\, e_{\boldsymbol{q}j}^{\boldsymbol{\kappa}\,*} \cdot \mathcal{Q}_{\boldsymbol{q}}(\boldsymbol{\kappa}) \tag{2.33}$$

$$\Pi_{\boldsymbol{q}j} = \sum_{\boldsymbol{\kappa}} \frac{1}{\sqrt{m_{\boldsymbol{\kappa}}}}\, e_{\boldsymbol{q}j}^{\boldsymbol{\kappa}} \cdot \Pi_{\boldsymbol{q}}(\boldsymbol{\kappa}) \tag{2.34}$$

From the quantum treatment of the Hamiltonian shown in Eqn. (2.30), we consequently obtain the eigenvalues, or phonon energy of the system as

$$E_{ph} = \sum_{\boldsymbol{q},j} \hbar\omega_{\boldsymbol{q}j} \left(\bar{n}_{\boldsymbol{q}j} + \frac{1}{2} \right) \tag{2.35}$$

with phonon occupation number $\bar{n}_{\boldsymbol{q}j}$ as

$$\bar{n}_{\boldsymbol{q}j} = \langle b_{\boldsymbol{q}j}^{\dagger}\, b_{\boldsymbol{q}j} \rangle = \frac{1}{e^{\hbar\omega_{\boldsymbol{q}j}/k_B T} - 1} \tag{2.36}$$

where k_B and T is Boltzmann's constant and temperature, respectively. Eqn. (2.36) is known as the Bose-Einstein distribution. It should be noticed that even the system is in the ground state without any vibration, the phonon energy still exists generated by the zero-point motion in quantum mechanics.

Phonon density of states (DOS) is one of the important properties in lattice dynamics, which is defined as the number of the phonon modes between the frequencies ω and $\omega + d\omega$, or between $\boldsymbol{q}$ and $\boldsymbol{q} + d\boldsymbol{q}$. With a linear tetrahedron method, phonon DOS is demonstrated as,

$$g(\omega) = \frac{1}{N} \sum_{\boldsymbol{q},j} \delta\left(\omega - \omega_{\boldsymbol{q}j}\right) \tag{2.37}$$

where N is the number of unit cells. The integral over the Brillouin zone goes over all $3n_a$ phonon bands with n_a the number of atoms in the unit cell. The partial (or projected) phonon density of states is defined as the contribution of a specified atom in cell to the total phonon DOS, which allows us to understand the origin of various branches in the phonon dispersion. The contribution to the partial density of states of an atom, from each phonon band j, is evaluated by

$$g_{\boldsymbol{\kappa}}(\omega) = \frac{1}{N} \sum_{\boldsymbol{q},j} \delta\left(\omega - \omega_{\boldsymbol{q}j}\right) \left| e_{\boldsymbol{q}j}^{\boldsymbol{\kappa}s} \right|^2 \tag{2.38}$$

where $\boldsymbol{e}_{\boldsymbol{q}j}$ is the polarization vector corresponding to the phonon frequency $\omega_{\boldsymbol{q}j}$.

According to the statistical mechanics, as far as the phonon energy of a system is obtained, the thermodynamic properties can be determined. For example, the Helmholtz free energy can be calculated as,

$$F_H = -k_B T \ln Z \tag{2.39}$$

where the partition function of harmonic phonon is

$$Z = e^{-\frac{U}{k_B T}} \prod_{\boldsymbol{q},j} \sum_{\boldsymbol{i}} e^{-\frac{E_{\boldsymbol{q},j,i}}{k_B T}} = e^{-\frac{U}{k_B T}} \prod_{\boldsymbol{q},j} e^{-\frac{\hbar\omega_{\boldsymbol{q}j}}{2k_B T}} \sum_{\bar{n}_{\boldsymbol{q}j}} \left(e^{-\frac{\hbar\omega_{\boldsymbol{q}j}}{k_B T}} \right)^{\bar{n}_{\boldsymbol{q}j}}$$

$$= e^{-\frac{U}{k_B T}} \prod_{\boldsymbol{q},j} \frac{e^{-\frac{\hbar\omega_{\boldsymbol{q}j}}{2k_B T}}}{1 - e^{-\frac{\hbar\omega_{\boldsymbol{q}j}}{k_B T}}} = e^{-\frac{U}{k_B T}} e^{-\frac{E_0}{2k_B T}} \prod_{\boldsymbol{q},j} \frac{1}{1 - e^{-\frac{\hbar\omega_{\boldsymbol{q}j}}{k_B T}}} \tag{2.40}$$

In Eqn. (2.40), U is the static energy of the crystal equilibrium and E_0 is the total vibrational zero point energy of the system,

$$E_0 = \frac{1}{2}\sum_{\boldsymbol{q},j}\hbar\omega_{\boldsymbol{q}j} \tag{2.41}$$

Then Eqn. (2.39) can be rewritten as,

$$F = U + \frac{1}{2}\sum_{\boldsymbol{q},j}\hbar\omega_{\boldsymbol{q}j} + k_B T\sum_{\boldsymbol{q},j} ln\left[1 - e^{-\frac{\hbar\omega_{\boldsymbol{q}j}}{k_B T}}\right] \tag{2.42}$$

In conclusion, we show that the second order term in crystal potential is sufficient to describe the system accurately where the anharmonic effects are negligible. In many cases, the atomic displacements are small so that the harmonic approximation is valid and useful for obtaining the phonon properties. However, it fails to describe many important properties generated by the lattice anharmonicity such as the thermal expansion, the lattice thermal conductivity (LTC), and the temperature or volume dependences of the phonon frequencies, for which we must go beyond the harmonic approximation.

2.2.3 Lattice anharmonicity

It is obvious that the harmonic term in the Hamiltonian gives the description of the independent phonons without interactions. In fact, the phonons are coupling and the naïve harmonic picture of the crystal vibrations sometimes breaks down. Lattice anharmonicity will generate the intrinsic phonon-phonon interactions and the lattice thermal expansion, which thereby plays an essential role in the thermal transport properties of system [10,133,134].

Concerning the thermal expansion, it is typically treated with the quasiharmonic approximation (QHA), where the anharmonicity is considered as a weak effect. In QHA, both the static energy U and phonon frequency $\omega_{\boldsymbol{q}j}$ are the functions of crystal volume V, which thus the Helmholtz free energy F is a function of both temperature T and volume V. The equation of state including state parameters p, V, and T is

$$p = \left(\frac{\partial F}{\partial V}\right)_T \tag{2.43}$$

With the replacement of the free energy demonstrated in Eqn. (2.42), Eqn. (2.43) can be written as,

$$p = -\frac{dU}{dV} - \sum_{\boldsymbol{q},j}\left(\frac{1}{2} + \frac{1}{e^{\frac{\hbar\omega_{\boldsymbol{q}j}}{k_B T}} - 1}\right)\hbar \cdot \frac{d\omega_{\boldsymbol{q}j}}{dV} \tag{2.44}$$

Furthermore, it is convenient to deal with the derivative of the phonon frequency as,

$$\gamma = -\frac{d\omega_{\boldsymbol{q}j}}{dV} = -\frac{\omega_{\boldsymbol{q}j}}{V}\frac{d\, ln\, \omega_{\boldsymbol{q}j}}{d\, ln\, V} \tag{2.45}$$

where γ is the mode Grüneisen constant showing that phonon frequency increases as volume decreasing and the rate of inverse proportion is nearly a constant. To generalize the problem, the simple vibrational system of the diatomic linear chain is considered, which the eigenvalue is

$$\omega_{qj}^2 = C\left(\frac{1}{m_\kappa} + \frac{1}{m_{\kappa'}}\right) \pm C\left[\left(\frac{1}{m_\kappa} + \frac{1}{m_{\kappa'}}\right)^2 - \frac{4}{m_\kappa m_{\kappa'}} sin^2\, qa\right]^{\frac{1}{2}} \tag{2.46}$$

Eqn. (2.45) and (2.46) can be combined into a form of

$$\gamma = -\frac{a\, \ddot{V}(a)}{2\, \dot{V}(a)}, \tag{2.47}$$

where $V(a)$ is the potential energy of the lattice constant *a*, and γ is related to the third order term of the potential energy as shown in Eqn. (2.47). If the anharmonic effect does not exist in lattice vibration, γ vanishes and there is no thermal expansion happen. From the above analyses, the anharmonicity indeed leads to the thermal expansion and can be treated with quasiharmonic approximation in which the thermal expansion is determined by the minimization of the *F* as a function of the cell volume at each temperature. This is one of the root cause of the anharmonic crystal showing the non-linear change of the phonon dispersion regarding the crystal volume.

Apart from the thermal expansion as discussed above, the anharmonicity also plays an important role in phonon scattering as the temperature changes, which results in the finite thermal conductivity, or equivalent, the thermal resistance. Phonons are the primary heat carriers for the nonmetallic crystalline solids where the heat is almost transferred by phonons. Generally, the phonon-phonon interactions can be considered as a perturbation to the harmonic system. For instance, the cubic and quartic term as in the first- and second-order perturbation leads to the three-phonon and four phonon interactions, respectively. The former is widely used for studying the phonon scattering events, which has large achievements in explaining the thermodynamic behavior of materials such as the lattice thermal

conductivity. The relaxation time approach solving the linearized phonon Boltzmann equation and the Green's function approach based on the fundamental quantum statistical mechanics, are two pictures of the popular understanding of the lattice thermal conductivity. In this work, we mainly focus on the former way of solving the linearized phonon Boltzmann equation. The original phonon Boltzmann equation is in the form of

$$\left.\frac{\partial n_{\boldsymbol{qj}}}{\partial t}\right|_{diff} + \left.\frac{\partial n_{\boldsymbol{qj}}}{\partial t}\right|_{scatt} = 0 \tag{2.48}$$

where $n_{\boldsymbol{qj}}$ is the occupation function of the phonon wave vector $\boldsymbol{q}$ of band index j. The gradient of the spatial dependent temperature, i.e., $T = T(\boldsymbol{r})$, gives rise to the diffusion at the rate of

$$\left.\frac{\partial n_{\boldsymbol{qj}}}{\partial t}\right|_{diff} = -\boldsymbol{v}_{\boldsymbol{qj}} \cdot \nabla T \, \frac{\partial n_{\boldsymbol{qj}}}{\partial T} \tag{2.49}$$

where $\boldsymbol{v}_{\boldsymbol{qj}}$ is the phonon group velocity of mode $\boldsymbol{qj}$ definded as $\boldsymbol{v}_{\boldsymbol{qj}} = \nabla_{\boldsymbol{q}}\, \omega_{\boldsymbol{qj}}$. The Eqn. (2.49) shows that the total rate of change of $n_{\boldsymbol{qj}}$ involving phonon diffusion and scattering mechanisms will vanish during the steady state of heat flow through the solid. To simplify the complicated Eqn. (2.48), the linearized phonon Boltzmann equation can be derived from taking the Taylor expansion of $n_{\boldsymbol{qj}}$ around the equilibrium distribution $\bar{n}_{\boldsymbol{qj}}$ into account. The single-mode relaxation-time approximation (abbreviate as SMRTA) provides the simplest description of the phonon interactions, where the relaxation rate of a phonon mode is on the assumption of all other phonon modes treated with their equilibrium states. In this approximation, the lattice thermal conductivity tensor is obtained from

$$\kappa = \frac{1}{NV_0} \sum_{\boldsymbol{qj}} C_{\boldsymbol{qj}} \boldsymbol{v}_{\boldsymbol{qj}} \otimes \boldsymbol{v}_{\boldsymbol{qj}} \tau_{\boldsymbol{qj}}^{SMRTA} \tag{2.50}$$

where V_0 and N are the volume of the each unit cell and the total number of the unit cells in crystal. The mode heat capacity $C_{\boldsymbol{qj}}$ depends only on the phonon frequency $\omega_{\boldsymbol{qj}}$ and the temperature T, which is given by

$$C_{\boldsymbol{qj}} = k_B \left(\frac{\hbar\omega_{\boldsymbol{qj}}}{k_B T}\right)^2 \frac{e^{\frac{\hbar\omega_{\boldsymbol{qj}}}{k_B T}}}{\left(e^{\frac{\hbar\omega_{\boldsymbol{qj}}}{k_B T}} - 1\right)^2} \tag{2.51}$$

In Eqn. (2.50), all these phonon properties except $\tau_{\boldsymbol{q}j}^{SMRTA}$ can be calculated using harmonic phonon calculations, while $\tau_{\boldsymbol{q}j}^{SMRTA}$ must go beyond harmonic approximation and take into account of the phonon-phonon interactions [22,52]. Here, an approximation of $\tau_{\boldsymbol{q}j}^{SMRTA} = \tau_{\boldsymbol{q}j}$ is used where the left- and right- side term are the single-mode relaxation time and phonon lifetime, respectively. By replacing the suffix $\lambda = (\boldsymbol{q}, j)$ and thus $-\lambda = (-\boldsymbol{q}, j)$, the phonon lifetime $\tau_{\boldsymbol{q}j} = \tau_\lambda$ can be calculated by

$$\tau_\lambda = \frac{1}{2\,\Gamma_\lambda(\omega)} \tag{2.52}$$

with imaginary part of the self-energy in a form analogous to the Fermi's golden rule as [52],

$$\Gamma_\lambda(\omega) = \frac{18\pi}{\hbar^2}\sum_{\lambda\lambda'}\Delta(-\boldsymbol{q}+\boldsymbol{q}'+\boldsymbol{q}'')\{(1+n_{\lambda'}+n_{\lambda''})\delta(\omega-\omega_{\lambda'}-\omega_{\lambda''}) + (n_{\lambda'}-n_{\lambda''})[\delta(\omega+\omega_{\lambda'}-\omega_{\lambda''})-\delta(\omega-\omega_{\lambda'}+\omega_{\lambda''})]\}\,|\Phi_{-\lambda\lambda'\lambda''}|^2 \tag{2.53}$$

where n_λ is the phonon occupation number at equilibrium state. $\Phi_{\lambda\lambda'\lambda''}$ is the strength of the interaction among the three phonons in the scattering process. $\Delta(\boldsymbol{q}+\boldsymbol{q}'+\boldsymbol{q}'')$ is a function whose value is one when $\boldsymbol{q}+\boldsymbol{q}'+\boldsymbol{q}''$ equals a reciprocal lattice vector $\boldsymbol{G}$, and zero otherwise. From Eqn. (2.50) to (2.53), it is obvious that the lattice thermal conductivity directly affected by the phonon lifetime arising from the three-phonon scattering. Other methods such as directly solving the linearized phonon Boltzmann equation (LBTE) proposed by Chaput can be found in reference [135].

In addition to the intrinsic phonon-phonon interactions, the phonon-isotope scattering is also crucial to the lattice thermal conductivity especially in some compounds its order of magnitude is same or even larger. The phonon-isotope scattering rate for a phonon mode λ is expressed as

$$\frac{1}{\tau_\lambda^{iso}(\omega)} = \frac{\pi}{2N}\omega_\lambda^2\sum_{\lambda'}\delta(\omega_\lambda-\omega_{\lambda'})\cdot\sum_\kappa g_\kappa\left|\sum_\alpha W_\alpha(\kappa,\lambda)W_\alpha^*(\kappa,\lambda')\right|^2 \tag{2.54}$$

where the mass variance parameter g_κ is

$$g_\kappa = \sum_i f_i\cdot\left(1-\frac{m_{i\kappa}}{\bar{m}_\kappa}\right) \tag{2.55}$$

The variables $m_{i\kappa}$ being the mole fraction and the mass of the *i*-th isotope of the atom κ in the each unit cell. The total scattering rate including both phonon-isotope and intrinsic phonon-phonon scattering rates are given by

$$\frac{1}{\tau_\lambda^{tot}(\omega)} = \frac{1}{\tau_\lambda(\omega)} + \frac{1}{\tau_\lambda^{iso}(\omega)} \tag{2.56}$$

By this way, the calculated lattice thermal conductivity is naturally incorporated the isotopes if the contribution of the phonon isotopes is considered.

In the above discussion, the lattice anharmonicity has the significant effects on the thermal expansion and lattice thermal conductivity at finite temperatures, and the temperature-dependent properties of anharmonic compounds can be treated with different approximations from low to high. In quasiharmonic approximations, the anharmonicity is considered as a weak effect and the phonon properties are computed considering only the thermal expansion effect. Generally, the calculations of the quasiharmonic approximation are simplified by using harmonic approximation at each crystal volume, which consequently obtains the volume dependence of the phonon properties. The self-consistent phonon (SCPH), or equivalently self-consistent harmonic approximation (SCHA), is applied to the strong anharmonic materials, which the phonon frequency from the quartic anharomonicity at a given temperature is renormalized self-consistently according to the SCPH equations [66,67],

$$\Omega_q^2 = \omega_q^2 + 2\Omega_q \sum_{q_1} I_{qq_1} \tag{2.57}$$

where the ω and Ω are the harmonic phonon frequency and renormalized frequency including temperature effects, respectively. I_{qq_1} is related to the Ω and the quartic harmonic term $\Phi^{(4)}$,

$$I_{qq_1} = \frac{\hbar}{8N} \frac{\Phi^{(4)}(q, -q, q_1, -q_1)}{\Omega_q \Omega_{q_1}} \left[1 + 2n\left(\Omega_{q_1}\right)\right] \tag{2.58}$$

It is apparent that Ω and I are mutually dependent, and the self-consistent results can be obtained by solving these two equations iteratively. Despite it is improve the accuracy of describing the strong phonon coupling system, the calculation of the quartic term is quite cumbersome and rarely be examined.

As we know, if a crystal with displaced atoms is dynamically stable against the finite lattice vibrations, it is manifested by all phonons with real and positive frequencies, or positive phonon bands under the harmonic approximation. The appropriate atomic displacements can reduce the potential energy of the atomic positions nearby that of equilibrium state. However, the phonon frequency becomes imaginary value evidently reflected as the negative one appeared in phonon band structures, which indicates dynamical instability of the system due to the incensement of the potential energy of the displacive

system. A phonon mode of which the frequency is going down due to some extra conditions such as temperature and pressure, and eventually becoming zero, is called soft mode with the process called by “phonon softening”. This phenomenon describes the vibration of the corresponding phonon mode becomes "frozen" under that external conditions, which thereby deforms the original structure and produces a more stable one with another symmetry.

Initially, the concept of the soft mode was proposed to describe the mechanism of the ferroelectric structural phase transitions. For instance, barium titanate ($BaTiO_3$) exists four polymorphs depending on temperature. With the temperature decreasing, the crystal symmetry of the four polymorphs becomes cubic, tetragonal, orthorhombic and rhombohedral. All these structures exhibit the ferroelectricity except the cubic state (paraelectric structure). In particular, the frequency of the lowest transverse optical branch in the cubic phase becomes lower when the temperature decreases to the critical temperature, which eventually makes the compound change to the tetragonal structure as the soft mode frozen. Therefore, it is very useful to analyze the imaginary mode appeared in the displacive phase transition. As normal DFT and phonon calculations on the conditions of 0 K, the phonon results of some structures with a certain symmetry stable at extreme high temperatures will show imaginary phonon frequencies denoting the dynamical instability. Imaginary phonons should be treated with the self-consistent phonon method rather than simple perturbation approach, which explicitly incorporates the temperature effect on the harmonic force constants. Furthermore, some studies demonstrated that it is important to renormalize the phonons with the effects of higher-order term such as quartic anharmonicity, and even to use the molecular dynamics simulations including all orders of the anharmoncity. These approaches indeed improve the accuracy of the calculation results while they are too computationally costly to some degree, which it is thereby urgent to develop an efficient and accurate approach making a balance between the computational cost and accuracy.

2.3 Temperature-dependent phonon calculations

To address the failure of the harmonic phonon calculations in describing the lattice dynamical properties of the structures with strong vibrational anharmonicity, an improved numerical way of the temperature-dependent phonon calculations is introduced in this work, where the force constants can be accurately fitted by a large amount of the force-displacement datasets including the temperature information. In this way, the well-converged phonon properties and related thermal properties can be acquired after certain iterative steps. The present approach is conceptually similar to the stochastic self-consistent harmonic approximation (SSCHA) [42] based on the self-consistent harmonic approximation (SCHA) [66,67] or equivalently self-consistent phonon theory (SCPH). In SCHA, a

quantum variational principle in the free energy can be established by a trial (harmonic) density matrix $\rho_{\mathcal{H}}$ in which $\mathcal{H}$is a trial Hamiltonian defined as $\mathcal{H} = T + \mathcal{V}$,

$$F_H \leq \mathcal{F}_H(\mathcal{K}) = F_{\mathcal{H}} + tr[\rho_{\mathcal{H}}(V - \mathcal{V})] \tag{2.59}$$

where the equality is obtained if $H = \mathcal{H}$. The vibrational free energy can be calculated by minimizing the functional $\mathcal{F}_H(\mathcal{K})$ with respect to the trial harmonic Hamiltonian $\mathcal{K}$ containing the atomic configuration $\mathcal{R}$ and the force constants matrix $\Phi(\mathcal{R})$ satisfying the self-consistent equation as

$$\Phi_{ab}(\mathcal{R}) = \left\langle \frac{\partial^2 V}{\partial R^a \partial R^b} \right\rangle_{\tilde{\rho}_{\mathcal{R},\Phi(\mathcal{R})}} \tag{2.60}$$

When the gradient of the free energy vanishes, the best approximation of the free energy thus can be obtained and the corresponding $\mathcal{H}$ is the final harmonic Hamiltonian that minimized it.

More recently, another approach is based on the self-consistent *ab initio* lattice dynamics (SCAILD) [62] approach, so-called QSCAILD [64,136], where the thermal mean-square displacement matrix computed under a classical assumption is replaced by the SSCHA density matrix with quantum statistics. For each iteration and each atomic configuration, the atomic forces f are fitted to a harmonic force-constants matrix Φ through solving the least squares minimization problem of

$$S = \sum_{k,n} \left(s_k^{(n)} \right)^2 \tag{2.61}$$

with

$$s_k^{(n)} = f_k^{(n)} + \sum_l \Phi_{kl} u_l^{(n)} \tag{2.62}$$

where k, l, n are the atom, Cartesian and configuration indices, respectively. To minimize the atomic forces, it requires for each $i, j, \frac{\partial S}{\partial \Phi_{ij}} = 0$. Combined with the above three equations, it is obtained that

$$\sum_n \left(f_i^{(n)} - f_{\mathcal{H}_i^{new}}^{(n)} \right) u_j^{(n)} = 0 \tag{2.63}$$

where $\mathcal{H}^{new}$ is the effective harmonic Hamiltonian of the next iteration and $f_{\mathcal{H}_i^{new}} = -\sum_i \Phi_{ij} u_j$ is the new set of forces. In the limit of an infinite number of atomic configurations, it is acquired that

$$\int_{\mathbb{R}^{3N}} \left[\left(f_i - f_{\mathcal{H}_i^{new}} \right) u_j \right] \rho_{\mathcal{H}}(u) du = 0 \tag{2.64}$$

Eqn. (2.64) is the self-consistent equation needed to be solved in this approach. The converged results obtained by the QSCAILD and SSCHA method have been verified in the sense of equivalent [136]. Our temperature-dependent approach refers to the minimization of forces and quantum thermal mean-square displacement matrix in QSCAILD. In particular, the calculation of the thermal mean square displacement matrix in temperature-dependent phonon calculations is using the method of random displacements from the canonical ensemble of harmonic oscillators, which the theoretical and numerical details are demonstrated as followings.

The probability to find the system with the atomic displacements $\boldsymbol{u}$ based on the harmonic approximation is given by [64],

$$\rho(\boldsymbol{u}) = C \cdot exp\left(-\frac{1}{2} \boldsymbol{u}^T \boldsymbol{\Sigma}^{-1} \boldsymbol{u} \right) \tag{2.65}$$

where C is a coefficient and $\boldsymbol{\Sigma}$ is the quantum covariance matrix as,

$$\boldsymbol{\Sigma}_{u_{\kappa\alpha}\, u_{\kappa'\beta}} = \frac{1}{2\sqrt{m_{\kappa} m_{\kappa'}}} \sum_{\boldsymbol{q},j} \sigma_{\boldsymbol{q}j}^2 \cdot e_{\boldsymbol{q}j}^{\boldsymbol{\kappa}\alpha}\, e_{\boldsymbol{q}j}^{\boldsymbol{\kappa}'\beta\,*} \tag{2.66}$$

which represents the variance of any two elements, i.e., displacements of the atom $\boldsymbol{\kappa}$ and $\boldsymbol{\kappa'}$ along direction α and β, respectively. $m_{\boldsymbol{\kappa}}$ and $e_{\boldsymbol{q}j}^{\boldsymbol{\kappa}\alpha}$ are the atomic mass and the eigenvectors of the phonon mode $(\boldsymbol{q}, j)$. $\sigma_{\boldsymbol{q}j}^2$ is the square of the normal length of mode $(\boldsymbol{q}, j)$ written as,

$$\sigma_{\boldsymbol{q}j}^2 = \frac{\hbar}{\omega_{\boldsymbol{q}j}} \left(1 + 2n_{\boldsymbol{q}j} \right) \tag{2.67}$$

where $\omega_{\boldsymbol{q}j}$, and $n_{\boldsymbol{q}j}$ are the eigenvalues of the phonon mode $(\boldsymbol{q}, j)$ and the Bose-Einstein distribution mentioned in Eqn. (2.36), respectively. Then we can obtain the probability distribution function, namely density matrix, by

$$\rho(\boldsymbol{u}) = C \cdot exp\left(- \sum_{\alpha\beta\boldsymbol{\kappa}\boldsymbol{\kappa}'j} \frac{\sqrt{m_{\kappa} m_{\kappa'}}}{2\sigma_{\boldsymbol{q}j}^2}\, e_{\boldsymbol{q}j}^{\boldsymbol{\kappa}\alpha}\, e_{\boldsymbol{q}j}^{\boldsymbol{\kappa}'\beta}\, u_{\alpha}(\boldsymbol{\kappa})\, u_{\beta}(\boldsymbol{\kappa}') \right) \tag{2.68}$$

Therefore, the atomic configurations can be sampled according to the probability distribution function in Eqn. (2.68). In this work, the sampling of atomic displacements in present temperature-dependent phonon calculations is processed by a convenient numerical way. It is found that $\mathcal{Q}_{\boldsymbol{q}j}$ is complex with real and imaginary parts denoted by $Re[\mathcal{Q}_{\boldsymbol{q}j}]$ and $Im[\mathcal{Q}_{\boldsymbol{q}j}]$, respectively, and there exists the relations of the normal coordinates at $\boldsymbol{q}$ and $-\boldsymbol{q}$ shown as followings,

$$\begin{aligned} \mathcal{Q}_{\boldsymbol{q}j} + \mathcal{Q}^{*}_{\boldsymbol{q}j} &= 2Re[\mathcal{Q}_{\boldsymbol{q}j}] \\ \mathcal{Q}_{\boldsymbol{q}j} - \mathcal{Q}^{*}_{\boldsymbol{q}j} &= 2i\, Im[\mathcal{Q}_{\boldsymbol{q}j}] \\ Re[\mathcal{Q}_{\boldsymbol{q}j}] &= Re[\mathcal{Q}_{-\boldsymbol{q}j}] \\ Im[\mathcal{Q}_{\boldsymbol{q}j}] &= -Im[\mathcal{Q}_{-\boldsymbol{q}j}] \end{aligned} \tag{2.69}$$

where $Re[\mathcal{Q}_{\boldsymbol{q}j}]$, $Re[\mathcal{Q}_{-\boldsymbol{q}j}]$, $Im[\mathcal{Q}_{\boldsymbol{q}j}]$ and $Im[\mathcal{Q}_{-\boldsymbol{q}j}]$ are real. The atomic displacements expressed in Eqn. (2.26) with another phase convention is

$$\boldsymbol{u}(\boldsymbol{l\kappa}) = \frac{1}{\sqrt{\Omega}} \sum_{\boldsymbol{q},j} \mathcal{Q}_{\boldsymbol{q}j}(\boldsymbol{\kappa})\, e^{\boldsymbol{\kappa}}_{\boldsymbol{q}j} \cdot e^{i\boldsymbol{q}\cdot\boldsymbol{R}(\boldsymbol{l\kappa})} \tag{2.70}$$

The calculation of a certain configuration can be performed at two main regions where the set of wave vectors is separated as shown in figure 2.2. It is seen that the two sets of wave vectors in Brillouin zone are A region including $\boldsymbol{q} = \frac{\boldsymbol{G}}{2}$ (Brillouin zone boundary) and center (Γ point), and B region including the half of the set of commensurate q-points (either $\boldsymbol{q}$ or $-\boldsymbol{q}$) except that in A region. Note that $\boldsymbol{G}$ is the reciprocal lattice of the crystal and the relations between it and direct lattice $\boldsymbol{R}$ are constructed as,

$$\begin{aligned} \boldsymbol{a}_i \cdot \boldsymbol{b}_j &= \boldsymbol{\delta}_{ij} \\ \boldsymbol{R} &= n_1\boldsymbol{a}_1 + n_2\boldsymbol{a}_2 + n_3\boldsymbol{a}_3 \\ \boldsymbol{G} &= m_1\boldsymbol{b}_1 + m_2\boldsymbol{b}_2 + m_3\boldsymbol{b}_3 \end{aligned} \tag{2.71}$$

where the Kronecker delta $\boldsymbol{\delta}_{ij}$ equals one when $i = j$ and is zero otherwise. The coefficients of n and m are integers defining the vertex, and the three primitive translation vectors $\boldsymbol{a}_i$ and $\boldsymbol{b}_j$ of the direct and reciprocal lattice, respectively.

If the wave vectors $\boldsymbol{q}$ in Brillouin zone boundary of A region, the phase in Eqn. (2.70) is simplified as,

$$e^{i\boldsymbol{q}\cdot\boldsymbol{R}} = e^{i\pi n} = cos(\pi n) + i \cdot sin(\pi n) = cos(\pi n) \quad n = 1,2,\ldots \tag{2.72}$$

Combined with the relations in Eqn. (2.69) and (2.72), the atomic displacements of the system, which is expressed in Eqn. (2.70), therefore can be given by,

$$\boldsymbol{u}(\boldsymbol{l\kappa}) = \frac{1}{\sqrt{\Omega}} \left\{ \sum_{\boldsymbol{q}\in A} \mathcal{Q}_{\boldsymbol{qj}} e_{\boldsymbol{qj}}^{\boldsymbol{\kappa}} \cos\left(\boldsymbol{q}\cdot\boldsymbol{R}(\boldsymbol{l\kappa})\right) \right.$$

$$+ \frac{1}{\sqrt{2}} \sum_{\boldsymbol{q}\in B} \left[\left(Re[\mathcal{Q}_{\boldsymbol{qj}}] + iIm\left[\mathcal{Q}_{\boldsymbol{qj}}\right] \right) e_{\boldsymbol{qj}}^{\boldsymbol{\kappa}} e^{i\boldsymbol{q}\cdot\boldsymbol{R}(\boldsymbol{l\kappa})} \right.$$

$$\left. \left. + \left(Re[\mathcal{Q}_{\boldsymbol{qj}}] - iIm\left[\mathcal{Q}_{\boldsymbol{qj}}\right] \right) e_{\boldsymbol{qj}}^{\boldsymbol{\kappa}\,*} e^{-i\boldsymbol{q}\cdot\boldsymbol{R}(\boldsymbol{l\kappa})} \right] \right\}$$

$$= \frac{1}{\sqrt{\Omega}} \left\{ \sum_{\boldsymbol{q}\in A} \mathcal{Q}_{\boldsymbol{qj}} e_{\boldsymbol{qj}}^{\boldsymbol{\kappa}} \cos\left(\boldsymbol{qR}(\boldsymbol{l\kappa})\right) + \sqrt{2} \sum_{\boldsymbol{q}\in B} Re[\mathcal{Q}_{\boldsymbol{qj}}] Re\left[e_{\boldsymbol{qj}}^{\boldsymbol{\kappa}}\, e^{i\boldsymbol{q}\cdot\boldsymbol{R}(\boldsymbol{l\kappa})}\right] - Im\left[\mathcal{Q}_{\boldsymbol{qj}}\right] Im\left[e_{\boldsymbol{qj}}^{\boldsymbol{\kappa}}\, e^{i\boldsymbol{q}\cdot\boldsymbol{R}(\boldsymbol{l\kappa})}\right] \right\}$$

(2.73)

It should be noticed that the calculations in B region can be chosen at any regions B_1 or B_2 owing to the symmetry of B_1 and B_2 region. Here, we restrict our attention to the q-space for the sampling of the harmonic oscillators and it is straightforward to obtain the normal distribution of $Re[\mathcal{Q}_{\boldsymbol{qj}}]$ or $Im[\mathcal{Q}_{\boldsymbol{qj}}]$ from the following expression as,

$$P\left(Re[\mathcal{Q}_{\boldsymbol{qj}}]\right) = P\left(Im[\mathcal{Q}_{\boldsymbol{qj}}]\right) = \frac{1}{\sqrt{2\pi\sigma_{\boldsymbol{qj}}^2}}\, e^{-\frac{\left(Re[\mathcal{Q}_{\boldsymbol{qj}}]\right)^2}{2\sigma_{\boldsymbol{qj}}^2}} \tag{2.74}$$

where

$$\sigma_{\boldsymbol{qj}}^2 = \langle \left| \mathcal{Q}_{\boldsymbol{qj}} \right|^2 \rangle = \langle \left(Re[\mathcal{Q}_{\boldsymbol{qj}}] \right)^2 \rangle = \langle \left(Im[\mathcal{Q}_{\boldsymbol{qj}}] \right)^2 \rangle = \frac{\hbar}{\omega_{\boldsymbol{qj}}} \left(1 + 2n_{\boldsymbol{qj}}\right) \tag{2.75}$$

Obviously, Eqn. (2.75) and (2.67) are equivalent, which means the covariance matrix for real and imaginary part of the displacement are same. With the normal distribution expressed in Eqn. (2.71), the real and imaginary part of the displacements can be separately sampled from canonical ensemble of harmonic oscillators, and be combined as the random displacements, which allows for simultaneous update of both phonon frequencies and eigenvectors, mimicking well the real situation where a crystal system is thermally populated at the finite temperatures.

The workflow of the temperature-dependent phonon calculations in this work is sketched in figure 2.3. Initially, the phonon calculations without temperature are performed based on the set of the ground state forces acting on some displaced atoms obtained from the *ab initio* calculation engine. This is the usual and simple phonon calculations as before, so-called harmonic phonon calculations. Then, in next steps of the phonon calculations at finite temperatures, a new set of displaced configurations with random displacements are generated from the probability distribution of normal coordinates at $\boldsymbol{q}$ space described by the phonon frequencies and eigenvectors computed at commensurate points. Once the atomic configurations with displacements are constructed, the forces calculations for all atoms in each configuration are performed with *ab initio* calculations. With the new set of force-displacement data, the force constants in current step can be constructed, which results in the eigenvalues and eigenvectors of the phonon modes. In this way, the anharmonicity is renormalized into the harmonic phonon frequencies and thus the effective harmonic force constants can be computed iteratively from the atomic forces and the corresponding atomic displacements.

Phonopy [137] is an open source package for the phonon calculations within the harmonic and quasi-harmonic approximations based on the finite-difference supercell approach [37,138,139]. In terms of the force constants calculator in Phonopy, only one atom is displaced in each supercell to obtain forces in the supercell and many supercells with different configurations of displacements are required to satisfy the degrees of freedom of force constants under the symmetry (see figure 2.4 (a)). The default value of the finite displacement for an atom is 0.01 Å in Phonopy. However, by using random displacements introduced in this work, all atoms can be displaced simultaneously in each supercell (see figure 2.4 (b)). With all these snapshots of atomic displacements, the sets of forces are then computed via first-principles calculations.

For a better fitting of the force constants with a number of force-displacement datasets, an external fitting engine for the force constants based on the supercell approach, so-called ALM [140], is suggested to be utilized instead of the default force constants calculator used in Phonopy. Combined with the group theory, an irreducible set of force constants are extracted from the symmetrically independent elements in the force constants and the constraints of translational and rotational invariance between them. The fitting method of least squares in ALM is used to estimate the effective harmonic force constants by minimizing the atomic forces according to the Eqn. (2.58). Note that at each step, it is better to use as many force-displacement datasets as possible to improve the fitting ability.

The total energy and force calculation can be performed at any external first-principles energy-force calculation engines, such as VASP package [127–130] used in this work. It should be emphasized that it is more difficult to fit the force constants since the lack of the crystal symmetry and seriously crystal

distortion. This is happened if there exists strongly random displacements at the extremely higher temperatures, which results in more calculation iterations and computationally expensive to obtain the converged phonon dispersions. Additionally, to release the computational stress, it is suggested that the force calculations can be started with less displaced configurations until the calculations are converged under the criteria [45]. Based on the initially converged results, the calculations are continued to be performed with more sets of the displaced configurations to improve the accuracy of the calculations. On the other hand, by using the reweighting technique, the calculations can be accelerated with the previous atomic configurations as mentioned in SSCHA approach. In present method, a simple way is adopted instead of using the reweighting one. The sets of forces-displacements in previous steps are introduced into that of the current step according to a mixing (memory) parameter, which results in a well-converged result by a quickly self-consistent process.

Owing to the better treatment of the effective force constants and anharmonic phonon frequencies generated by the temperature effect, the temperature-dependent phonon calculations introduced in this work allows us to assess the structural stability at finite temperatures, which are expected to be an efficient and robust approach for systematical investigations of the lattice dynamics of abundant materials. Furthermore, the conventional approach for calculating the lattice thermal conductivity is accurate enough in terms of weakly anharmonic materials, whereas it collapses for those materials are dynamically unstable at 0 K. Therefore, it is necessary to develop the temperature-dependent phonon calculations, which is highly demanded for predicting the thermal transport properties at finite temperatures, especially for a high-efficiency high-throughput screening of materials, and for evaluating the related performance in potential applications and devices.

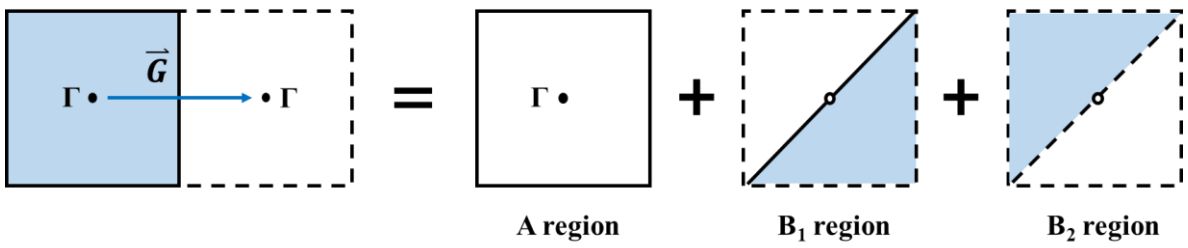

Figure 2.2. A simple schematic of the Brillouin zone (left side) which can be separated into two regions, i.e., A and B regions (right side). In A region, the calculations would be performed with the wave vectors $\boldsymbol{q}$ at the center point (black circle) or the Brillouin zone boundary (black borders). In B regions made of the equivalent B1 and B2 region, the calculations would be performed with the wave vectors $\boldsymbol{q}$ at any half of the B regions (blue area) including the diagonal. The reciprocal lattice denoted as $\boldsymbol{G}$ represents the vector pointing from the Γ center of a Brillouin zone to another one.

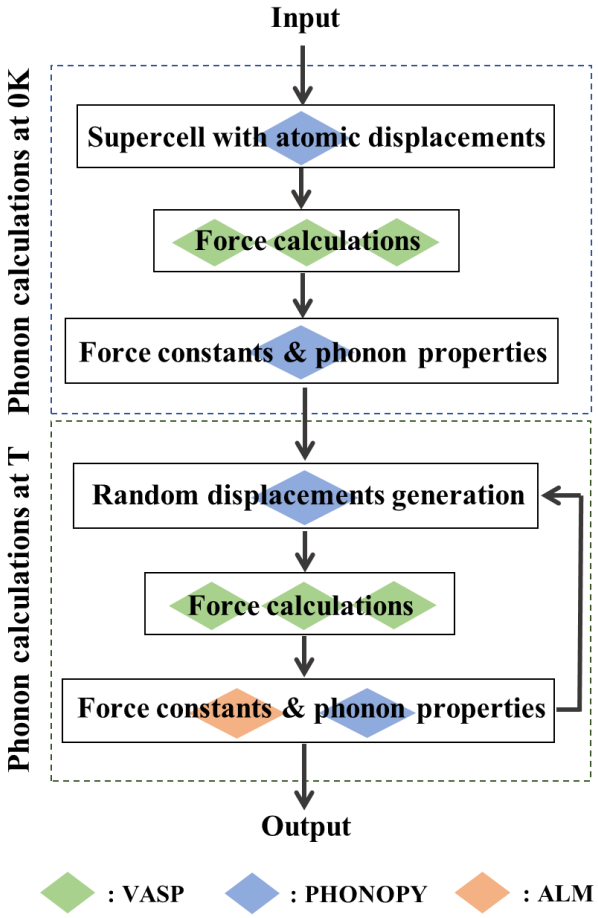

Figure 2.3. Sketch of the temperature-dependent phonon calculations in this work. The green, blue and red diamond box denote the different calculation tools, i.e., VASP, Phonopy and ALM. The steps in blue dashed box and green dashed box are the harmonic and temperature-dependent phonon calculations, respectively.

Figure 2.4. Sketch of the displaced patterns where the atomic displacements generated by (a) finite-displacement supercell approach and (b) random displacement approach. In the former case, only one atomic displacement is generated in one displaced pattern illustrated as the red circle with an arrow denoting the displacement. In the latter case, multiple atomic displacements are occurred simultaneously due to the finite temperatures.

Chapter 3

Lattice dynamics of rocksalt-type halides and chalcogenides

3.1 Introduction

Thanks to the development of computing power and advanced algorithms, the physical methodologies of *ab initio* calculations for electronic ground states and lattice vibrational states are improved rapidly, which is of great importance in its powerful prediction of electronic, optic, magnetic and dynamic properties of the target materials [1–21]. The rocksalt-type binary compounds are structurally simple and mostly semiconductors or insulators with large electronic band gaps, which are the desirable materials for fabricating the novel microelectronic and optical devices [92–107]. Meanwhile, they have been widely studied owing to their strikingly distinctive lattice thermal conductivities, which draws extensive research attentions to understand theoretically and experimentally the underlying mechanisms of the vibrational and the heat transfer phenomena.

Most of the alkali halides, with the chemical formula MX where M-site elements are the monovalent alkali metals and X-site elements are the halogens, belong to the family of the rocksalt structures. In these bulk crystals, each ion is surrounded by six ions with the opposite charges, which forms the octahedral coordination geometry. Apart from the structural simplicity and shining prospects for the electronic devices, their thermodynamic properties and heat transport performance have gained a huge interest. As a representative, the sodium chloride, namely NaCl with the space group of $Fm\bar{3}m$, is well known for its high melting temperature of about 1074 K and stable phase up to a pressure of about 30 GPa. A large number of the experimental and theoretical information have been collected for examining the thermodynamic behavior of NaCl-like structure. However, it still remains the challenge

of a comprehensive understanding of the microscopic mechanisms behind some thermodynamic phenomena. Previous studies have shown that NaCl is a strongly anharmonic crystal with weak ionic bonds and is usually stable at room temperature [109,110]. It has relatively large thermal expansion, which in turn results in the low thermal conductivity due to its light atomic mass. Unfortunately, both of the harmonic and quasiharmonic approximation are insufficient to describe the anharominicity of NaCl at finite temperatures, which is manifested by the large discrepancies between the measurements and the conventional phonon calculations of the phonon frequencies and the lattice thermal conductivities. On the other hand, vigorous attempts have been made to study the II-VI binary compounds MX with the simple rocksalt structure consisted of a chalcogen X and a divalent alkaline-earth metal M. Most of these materials are potential candidates for the electronic, optic and thermal applications. For instance, the experimentally well-characterized magnesium oxide (MgO) which belongs to the rocksalt-type oxides, have been extensively studied for many applications on electric devices, catalysis and thin film depositions as a substrate [24,56,141]. However, the reports on the vibrational phenomena and the thermodynamics of the II-VI rocksalt structures are very scarce.

Therefore, it is necessary to improve the phonon calculation tool for obtaining the accurate vibrational properties and the thermal properties. In this work, the temperature-dependent approach based on the first-principles phonon calculations is derived, which the mathematical details of the calculation procedure have been demonstrated in Chapter 2, and is adopted on NaCl compound firstly. Many efforts have been devoted to comprehensively understand the lattice dynamical properties of the simple and useful rocksalt structures, which a large amount of available data can be compared with that of the improved phonon calculations. Therefore, it is useful to conduct the high-throughput screening of the selected binary rocksalt compounds, not only for systematically investigating the thermodynamic behavior of these compounds at room temperature, but also for checking the validity and applicability of the temperature-dependent phonon calculations.

In Chapter 3, a class of compounds for 32 binary rocksalt-type compounds of which the elements come from the group I, II, VI, and VII, are systematically investigated in order to study their lattice dynamics and thermal transport properties by means of our developed approach of temperature-dependent phonon calculations as mentioned in Chapter 2. The computational details such as the physical and mathematical theory and the setting parameters used in the calculations are introduced in section 3.2. To prove the robustness of the parameters chosen in first-principles and high-throughput calculations, an example of NaCl compound is carefully examined by a series of calculations using different potential factors and convergence criteria, such as the energy cutoff, exchange-correlation functional, supercell size and sampling points, etc. After the determination of all calculation parameters, the application of the improved first-principles phonon calculations are performed for all selected rocksalt-

type compounds. In section 3.3, the calculated results of the basic phonon properties, i.e. phonon band structures and phonon density of states, are discussed firstly. Furthermore, the lattice thermal conductivity of these compounds are computed based on the fitted force constants incorporating the temperature information. The numerical results are also compared with available experimental data and other calculation results. To find the common and distinctive features of the lattice thermal conductivities among all these compounds, the mode contributions of the lattice thermal conductivity and the distributions of phonon lifetime and scattering are analyzed in details. Finally, a conclusion of the work in this chapter will be presented.

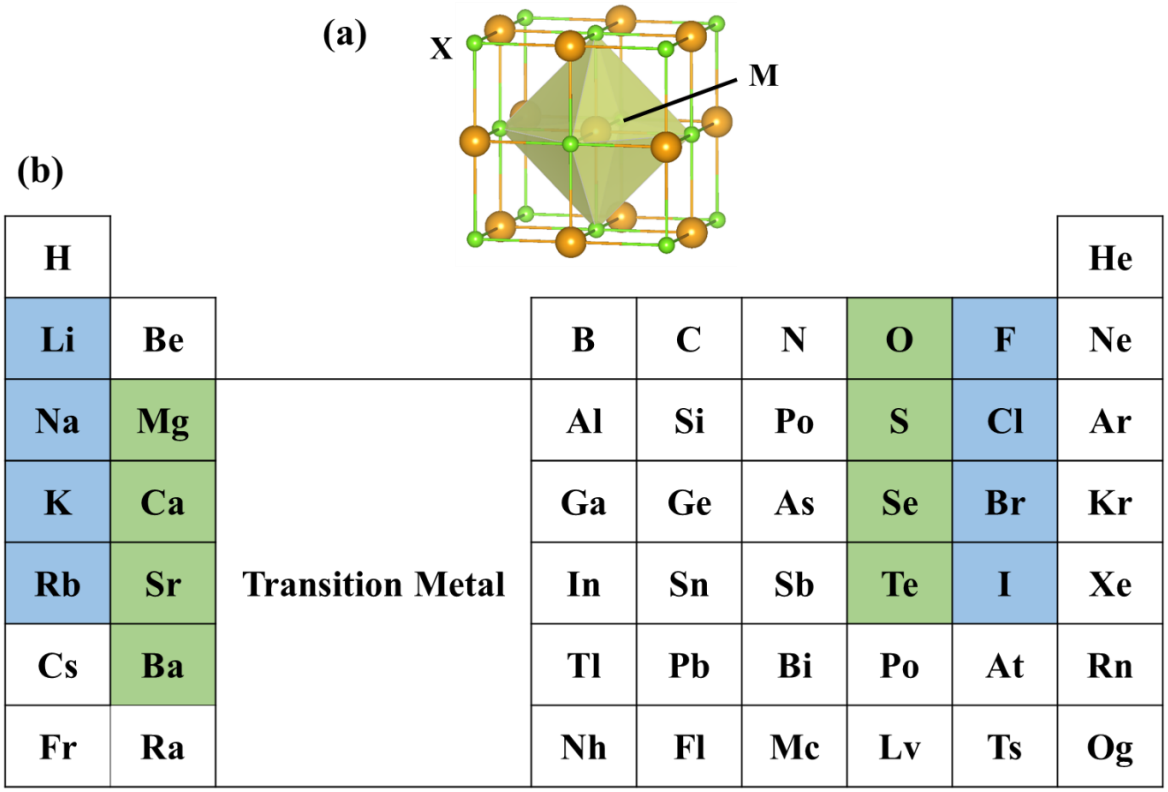

Figure 3.1. (a) Crystal structure model of the binary rocksalt compound MX, where the cation M and anion X are denoted as orange and green balls, respectively. (b) A simple periodic table. The elements selected for combinations of 32 rocksalt crystal structures MX are denoted by blue area. The element M is from group I and II, and element X is from group VII and VI.

3.2 Methods

3.2.1 Computational details

To compare with the available experimental data of the vibrational and thermal dynamical properties of the rocksalt structure, 32 binary compounds MX with rocksalt structure were examined, where the elements are chosen from the group I-VII (M = Li, Na, K, Rb; X = F, Cl, Br, I) and group II-VI (M = Mg, Ca, Sr, Ba; X = O, S, Se, Te), respectively. As shown in figure 3.1 (b), the crystal configuration of binary rocksalt-type structure can be considered easily as two interpenetrating face-centered cubic lattices, where each ion has a coordination number of six.

The first-principles calculations were carried out within thee framework of density functional theory using the projector-augmented wave (PAW) [142] potentials as implemented in Vienna *ab initio* simulation package (VASP) [127–130]. The generalized gradient approximation (GGA) [143,144] of Perdew, Burke, and Ernzerhof revised for solids (PBEsol) [145] was employed in the treatment of the exchange correlation functional because of its excellent performance to predict the lattice constants for a wide class of materials, which is important for the accuracy of the next phonon calculations. In each force calculation, the total energy of each system was minimized until the energy difference between two consecutive electronic steps becomes less than 10^{-8} eV.

In order to make a balance between the computational cost and accuracy, the related parameters, i.e., supercell size, *k*-point mesh and kinetic energy cutoff, used in force calculations were carefully evaluated. The details of the calculation parameters are in section 3.2.2. As the evaluation of the parameters, it is found that the 520 eV energy cutoff for the plane-wave basis set and the Brillouin zone was sampled by 2 × 2 × 2 *k*-point mesh centered at the Γ point generated by Monkhorts-Pack scheme, predicted almost the same qualitative and quantitative phonon properties as the combinations of the other parameters. In addition, compared with the phonon band structures using other supercell sizes, 2 × 2 × 2 supercell size containing 64 atoms was sufficient to obtain the accurate results. It should be noticed that the lattice constant of the each compound was obtained from the experimental results (see Table 3.1 and 3.2) [146–154], which thereby incorporates the volume effect of the lattice thermal expansion regarding the temperature. However, it is necessary to examine the difference of the lattice constants from the calculations and experiments in case of the lack of the available experimental data. The examinations of the different lattice parameters optimized using different exchange correlation potentials are also presented in section 3.2.2. In this work, if the experimental date unfortunately were unavailable, the lattice constants were selected from that optimized by DFT calculations with the exchange correlation potential of PBEsol. In particular, the elastic constants and bulk modulus were

also calculated to examine the mechanical stability of compounds. For each structure with or without strain effect, it was fully relaxed until both of the force and energy reach their convergence thresholds of 10^{-3} eV/Å and 10^{-3} eV, respectively. The theory of elastic constants and bulk modulus are presented in section 3.2.3.

In phonon calculations at 0 K, the second-order force constants were computed through the supercell approach with finite-displacement method as implemented in Phonopy [9]. Then the phonon calculations at ambient temperature were started from the second-order force constants at 0 K with the 100 atomic configurations sampled by the random displacements approach, where the anharmonic effect of the temperature was incorporated. Both of the theoretical analyses and numerical workflow have been illustrated in section 2.3. The effective harmonic force constants were computed self-consistently by rebuilding another new 100 displaced configurations in each iteration. These iterative calculations would be stopped until the free energy convergence becomes less than 1 meV/atom, which results in the well-converged phonon band structures and densities of states. The phonon band structures computed by different number of the displaced configurations per iteration have been tested. In figure 3.2 (d), it is evident that the phonon band structures are almost identical, which is independent of the number of sampled configurations. Considering the ionic polarization of the compounds, the non-analytical term correction to the harmonic dynamical matrix was included to treat the LO-TO splitting around the Γ point. In the ionic crystals, the dynamical matrix can be separated into two parts with and without analytic dependence of the wave vector $\boldsymbol{q}$. The physical theory and technical details of the non-analytic correction are discussed in section 3.2.4.

Furthermore, the lattice thermal conductivities (LTC) of these compounds were studied as implemented in the Phono3py package [40]. In this work, both the second- and the third-order force constants were estimated via the ALM interface in Phono3py using the force-displacement datasets. The LTC values were computed by solving the linearized phonon Boltzmann transport equation with single-mode relaxation time approximation (SMRTA). As a comparison, the calculated LTC values obtained from the fully direct solutions to the linearized phonon Boltzmann transport equation (LBTE) and from experiments in previous studies are also presented in this work. It should be noticed that the natural phonon-isotope scattering was also incorporated in the LTC calculations.

The q-point mesh of 28 × 28 × 28 sampled in Brillouin zone were set for the LTC calculations for all the crystal structures. The lattice constants used for the calculations mentioned as before were selected from the experimental values if available, or from ones optimized by the PBEsol pseudopotential otherwise. The second- and third-order force constants were extracted from the force-displacement datasets by the ALM [77] interface after the temperature-dependent phonon calculations converged well. Here, the force constants fitting algorithm in ALM rather than the default one in Phonopy and

Phono3py was used because of the better fitting results with the less noise through the former way. Before these parameters were determined, a series of calculations were conducted to examine the impact of the different variables on thermal conductivity, which are demonstrated in section 3.2.2.

Table 3.1. Lattice constants [146–149], volumes of the unit cells, calculated and experimental [155] bulk modulus of the rocksalt compounds in the group I-VII chosen in the present work.

I-VII	a (Å)	V (Å^3)	*B* (GPa)	
			This work	Expt.
LiF	4.030	16.36	70.18	67.10
LiCl	5.056	32.31	36.17	29.80
LiBr	5.490	41.37	24.73	23.80
LiI	6.022	54.60	18.07	17.20
NaF	4.620	24.65	51.29	46.50
NaCl	5.645	44.97	24.00	24.00
NaBr	5.961	52.95	20.40	19.90
NaI	6.473	67.80	15.17	15.10
KF	5.348	38.24	35.89	30.50
KCl	6.292	62.29	17.23	17.50
KBr	6.601	71.91	15.32	14.80
KI	7.066	88.20	11.80	11.70
RbF	5.657	45.26	29.63	26.30
RbCl	6.577	71.14	16.81	15.60
RbBr	6.889	81.72	13.77	13.00
RbI	7.336	98.71	10.90	10.50

Table 3.2. Lattice constants [150–154], volumes of the unit cells, calculated and experimental [155] bulk modulus of the rocksalt compounds in the group II-VI chosen in the present work.

II-VI	a (Å)	V (Å^3)	*B* (GPa)	
			This work	Expt.
MgO	4.210	18.65	162.66	165.00
MgS	5.190	34.95	77.79	
MgSe	5.460	40.69	65.54	
MgTe	6.020	54.54	41.26	
CaO	4.811	27.84	104.83	114.00
CaS	5.689	46.03	56.02	
CaSe	5.916	51.76	48.42	
CaTe	6.348	63.95	37.48	
SrO	5.160	34.35	89.17	88.00
SrS	6.024	54.65	49.14	
SrSe	6.234	60.57	43.38	
SrTe	6.660	73.85	33.31	
BaO	5.540	42.51	76.25	61.00
BaS	6.387	65.14	44.28	
BaSe	6.595	71.71	38.98	
BaTe	7.007	86.01	30.02	

3.2.2 Influence of the choices of the calculation parameters

The first-principles phonon calculations may influenced by many factors such as the choices of the lattice parameter, supercell size, plane wave energy cutoff, exchange correlation potential and sampling mesh in reciprocal space. Therefore, it is necessary to check these potential factors before applied to all the other structures. Taking NaCl compound as an example, a 2 × 2 × 2 supercell was constructed and the atomic forces were calculated with atomic displacements of 0.01 Å at 0 K. For the different energy cutoff from 350 eV to 520 eV, the 2 × 2 × 2 *k*-point mesh was fixed, and for the different *k*-point sampling meshes from 2 to 6, the energy cutoff of 520 eV was fixed in each calculation (600 eV for LiF compound), respectively. The results are illustrated in figure 3.2 (a) and (b). It is obvious that there are subtle changes of the phonon band structures among the force calculations with different *k*-

grids and energy cutoff. It should be emphasized that the plane-wave energy cutoff was specified to be at least 20% higher than the recommended "ENMAX" values in PAW datasets according to the suggestions in previous study, which is considered as a significant impact on the LTC values. Here, the plane-wave cutoff energy of 520 eV was fixed for the DFT calculations for all of the compounds except LiF (600 eV was the default value in this work), since this value is high enough to obtain the accurate result.

In terms of the supercell size, the 2 × 2 × 2 and 4 × 4 × 4 supercells were constructed, respectively, with the energy cutoff of 520 eV and 2 × 2 × 2 *k*-point mesh. From figure 3.2 (c), it is found that both of the phonon band structures with two sizes of the supercells are almost overlapped with only slight discrepancies happened during some symmetry paths. Therefore, in all of the force calculations, the compounds were enlarged as 2 × 2 × 2 supercells, the kinetic energy cutoff of 520 eV and Γ-centered Monkhorst-Pack grids of 2 × 2 × 2 division of the reciprocal unit cell were set, which avoid the expensive computational costs while maintaining enough accuracy of the results.

Furthermore, the different exchange correlation functionals, i.e., LDA, PBE and PBEsol, in force calculations using experimental lattice constants were evaluated with fixed settings as mentioned above. The phonon band structures computed by different potentials at 0 K and 300 K are displayed in figure 3.2 (e) and (f). It is clearly seen that the phonon frequencies of LDA functional are systematically lower than that of PBE and PBEsol functionals. Beyond the above potentials, there are lots of accurate exchange-correlation functionals can be measured such as hybrid functional and van der Waals density functionals, which results in very expensive electronic calculations. Generally, the main purpose of choosing different exchange correlation potentials is to obtain the well-predicted lattice parameter of the given structure at ground state. Considering the structures were built with experimental lattice constants in this work, the exchange correlation functional of PBEsol was thereby chosen as it can average the effect of the other two estimation results, which leads to more accurate phonon properties with respect to that of the experiment. Comparing the figure 3.2 (e) and (f), for each calculated result within a certain functional, the occurred phonon frequency shifting from 0 K to 300 K demonstrates that the anharmonic phonon-phonon interactions play the critical role in temperature-dependent phonon calculations, which cannot be simply solved by the method for the volume-dependent phonon calculations such as quasiharmonic approximation.

Although the lattice constants used for the first-principles phonon calculations were selected from the experimental values in this work, it is critical to see the differences of the results with different choices of the lattice parameters. In geometry optimization, using high-energy cutoff of 520 eV and 5 × 5 × 5 *k*-point mesh samplings, all 2 × 2 × 2 supercell structures calculated with LDA, PBE and PBEsol functionals, were fully relaxed until the Hellmann–Feynman force on each atom was less than 10^{-5}

eV/Å. The difference of the phonon band structures at finite temperatures between the calculated and the experimental results [156] are illustrated in figure 3.3 (a). It is apparent that phonon frequencies of the optical branches and that of the acoustic branches in the paths of Γ–X and Γ–L–W computed by LDA potential are generally higher than other calculated results, whereas phonon frequencies computed by PBE are the lowest during most of the high-symmetry paths. The phonon band structures computed by PBEsol potential are roughly in the middle of the other two band structures. At Γ point, the experimental measurement of LO and TO branches are close to calculated results of PBEsol and of PBE potential, respectively. At X point, the optical branches calculated by the PBE functional rather than other functionals agrees well with measurement. Other phonon branches at high-symmetry points computed by PBE and PBEsol functionals are in a relatively good match with experimental data.

In addition, the phonon band structures calculated using the experimental lattice constant with different exchange correlation functionals are also compared with experimental measurement. As presented in figure 3.3 (b), the band structures calculated by LDA and PBE functionals are different from those in panel (a) of which the phonon frequencies of LDA calculation become systematically higher than that of PBE calculation. It should be emphasized that the comparison between calculated and experimental data is mainly to verify the validity of this approach. In fact, the small discrepancies of the results using different functionals are not necessary if we using the same functional for all calculations where the effects are considered to be exerted on all results. Therefore, PBEsol functional was determined to use in this work for the next high-throughput investigations of all rocksalt-type compounds.

In figure 3.3 (c), the available experimental data of 80 K [156] are shown as a comparison with calculated data using the experimental lattice constants with PBEsol functional. According to the experimental data of 80 K and few of 300 K at X, L and Γ point, the phonon frequencies of NaCl compound show a small extent of softening as the temperature increases. Compared with the experimental data, it is obviously seen that both of the two calculated phonon band structures using PBEsol potential at 80 K and 300 K are in good agreement with the measurements, especially at L point in Brillouin zone, respectively.

As mentioned before, the exchange correlation potential has an impact on the structural optimization, which further influences the phonon properties and the LTC. Here, all of the lattice constants optimized by different potentials are listed in table 3.3. As we found, the lattice constants and the static volumes of the unit cells optimized by the different exchange correlation functionals follow the trends of $a_{LDA} < a_{PBEsol} < a_{Expt.} < a_{PBE}$ and $V_{LDA} < V_{PBEsol} < V_{Expt.} < V_{PBE}$, respectively. This is similar to the usual performance that the LDA functional underestimates the static volume of structure whereas the PBE functional overestimates it. The PBEsol functional, to some degree, makes a balance between these two kinds of functionals.

It is interesting to see how much difference of the LTC values using the different lattice constants. In order to improve the accuracy of the calculations, the number of the sampling q-point mesh in reciprocal space should be carefully checked at first. For the rocksalt structures considered here, the thermal conductivity tensor can be described by a single component, i.e., $\kappa_{xx} = \kappa_{yy} = \kappa_{zz} = \kappa$ and the off-diagonal terms are zero. In figure 3.4, the LTC values of the NaCl compound with respect to the number of sampled q-points are illustrated. As seen from the figure, the trend of these two well-converged curves is identical and the values of SMRTA method are lower than that from LBTE method. Since both of the two curves become flatten with more than 2×10^4 samplings, it is appropriate and enough to choose 28 × 28 × 28 q-point mesh denoted as red circles in both of the two curves, for obtaining the well-converged LTC values.

Then, the calculated LTC values at room temperature using the lattice constants from the first-principles calculations and from the experimental data are presented in table 3.3 from comparison. It is evident that the larger LTC values are obtained by the exchange correlation potentials given smaller lattice constants, i.e., $\kappa_{PBE} < \kappa_{Expt.} < \kappa_{PBEsol} < \kappa_{LDA}$ as $a_{LDA} < a_{PBEsol} < a_{Expt.} < a_{PBE}$. However, if using the experimental lattice constants, the trend of the calculated LTC values becomes $\kappa_{LDA} < \kappa_{PBEsol} < \kappa_{PBE}$ as $a_{LDA} < a_{PBEsol} < a_{PBE}$. For NaCl coumpound, the calculated LTC using SMRTA method with PBEsol potentials are in a very good agreement with the experimental data. Therefore, all the calculations in this work were performed with their experimental lattice constants and the PBEsol functional to be expected to obtain the LTC values comparable to the measurements.

Table 3.3. Experimental and calculated lattice constants using different exchange correlation potentials, volumes of each unit cells, and the LTC values at room temperature with the different lattice constants and the exchange correlation potentials. The experimental data are also presented in the parentheses.

	a (Å)	V (Å^3)	κ_{xx} (W/m-K)	
			SMRTA	LBTE
Calc. / LDA	5.465	163.26	10.68	11.91
Calc. / PBE	5.693	184.46	6.97	7.96
Calc. / PBEsol	5.604	175.99	8.34	9.35
Expt. / LDA	5.645	179.88	6.21	6.95
Expt. / PBE	-	-	8.09	9.17
Expt. / PBEsol	-	-	7.12	8.00
				(7.10)

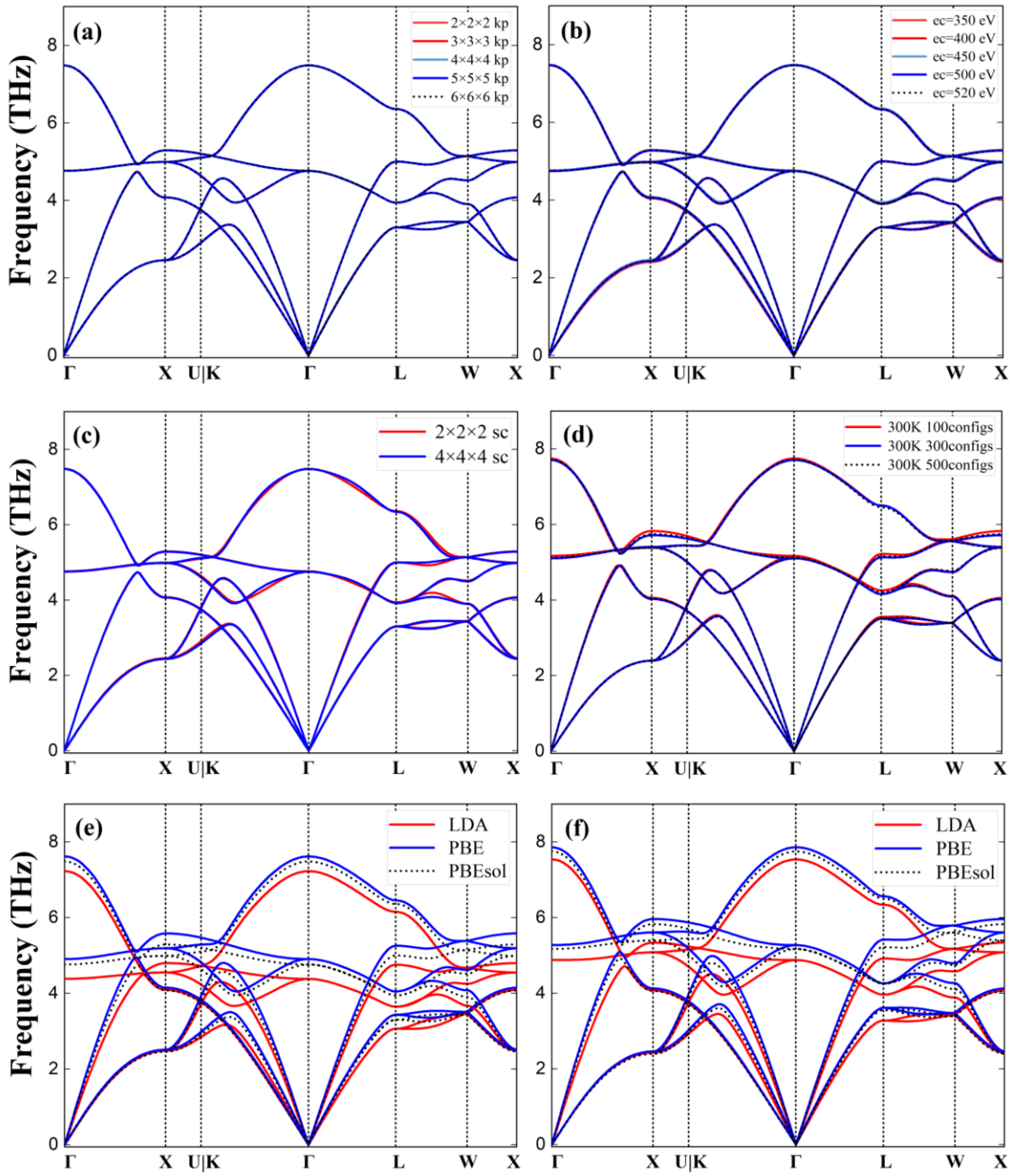

Figure 3.2. Phonon band structures of NaCl compound at 0 K where the force calculations are using different (a) *k*-point mesh samplings in Brillouin zone, (b) energy cutoff values, and (c) supercell sizes, respectively. (d) Phonon band structures of NaCl at 300 K with respect to the different atomic configurations. Phonon band structures computed using different exchange correlation functionals, i.e. LDA, PBE, PBEsol denoted as solid red, blue lines and dot black lines with the room-temperature experimental lattice constants at (e) 0 K and (f) 300 K, respectively.

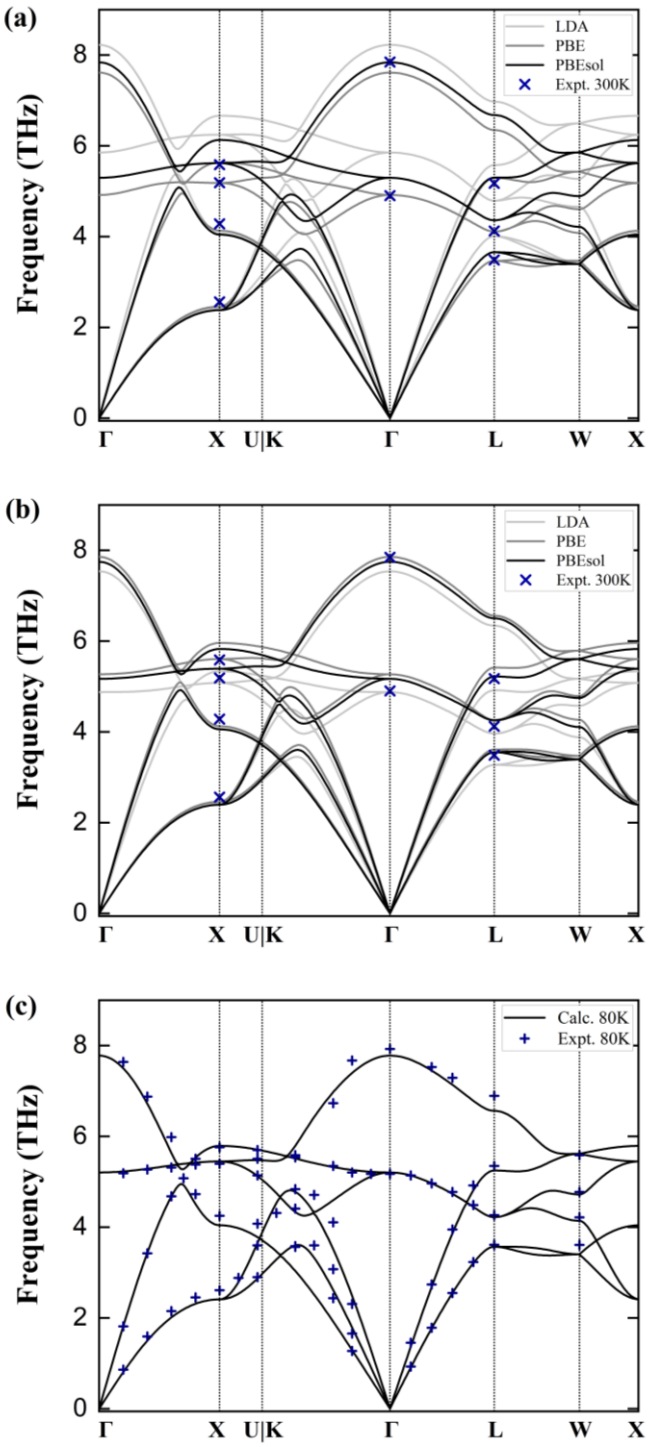

Figure 3.3. Phonon band structures of NaCl compound (a) at room temperature calculated using the different lattice constants optimized by different exchange correlation functionals, (b) at room temperature calculated using the room-temperature experimental lattice constants but different exchange correlation functionals, and (c) at 80 K calculated using the experimental lattice constants with PBEsol functional. The different exchange correlation functionals are LDA, PBE and PBEsol which are denoted as light grey, grey and black lines, respectively. The experimental data measured at 80 K marked in panel (c), and at 300 K marked in panel (a) and (b), are denoted as cross (+) and cross (×) marks, respectively [156].

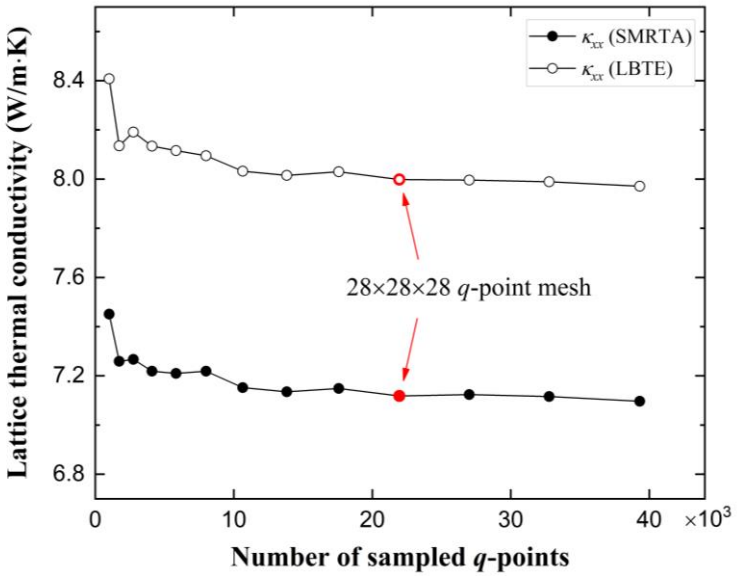

Figure 3.4. Calculated LTC values of NaCl compound at room temperature with respect to the number of sampled q-point samplings in Brillouin zone. Experimental lattice constants and exchange correlation functional of PBEsol were employed in the calculations.

3.2.3 Elastic constants and bulk modulus

The elastic constants are significant for evaluating the mechanical stability of a bulk crystal and the thermodynamic behaviors of materials at finite temperature or pressure [157]. According to the theory, the homogeneous stresses can be expressed in terms of the strains in a linear form as

$$\sigma_{ij} = c_{ijkl}\,\epsilon_{kl} \qquad (i,j,k,l = 1,2,3) \tag{3.1}$$

where σ_{ij} and ϵ_{kl} are the components of the 3 × 3 stress and strain matrix, respectively. c_{ijkl} are the components of the 3 × 3 × 3 × 3 elastic stiffness constants tensor of the bulk. By using the Voigt notation, it is possible to write Eqn. (3.1) in a compact form as

$$\sigma_i = C_{ij}\,\epsilon_j \qquad (i,j = 1,2,\dots,6) \tag{3.2}$$

where now C_{ij} are the components of the second order elastic stiffness tensor expressed by a 6 × 6 symmetric matrix. The stress and strain components are abbreviated into a single suffix given by

$$\begin{bmatrix} \sigma_{11} & \sigma_{12} & \sigma_{13} \\ \sigma_{21} & \sigma_{22} & \sigma_{23} \\ \sigma_{31} & \sigma_{32} & \sigma_{33} \end{bmatrix} \rightarrow \begin{bmatrix} \sigma_1 & \sigma_6 & \sigma_5 \\ \sigma_6 & \sigma_2 & \sigma_4 \\ \sigma_5 & \sigma_4 & \sigma_3 \end{bmatrix}$$

$$\begin{bmatrix} \epsilon_{11} & \epsilon_{12} & \epsilon_{13} \\ \epsilon_{21} & \epsilon_{22} & \epsilon_{23} \\ \epsilon_{31} & \epsilon_{32} & \epsilon_{33} \end{bmatrix} \rightarrow \begin{bmatrix} \epsilon_1 & \frac{1}{2}\epsilon_6 & \frac{1}{2}\epsilon_5 \\ \frac{1}{2}\epsilon_6 & \epsilon_2 & \frac{1}{2}\epsilon_4 \\ \frac{1}{2}\epsilon_5 & \frac{1}{2}\epsilon_4 & \epsilon_3 \end{bmatrix} \tag{3.3}$$

Elastic stiffness tensor is derived from the second-order derivative of the total energies versus strain, which the elastic energy ΔE of a bulk under strain in the harmonic approximation is given as

$$\Delta E(V,\epsilon) = E(V,\epsilon) - E(V_0,0) = \frac{V_0}{2}\sum_{i,j=1}^{6} C_{ij}\,\epsilon_i\epsilon_j \tag{3.4}$$

where $E(V,\epsilon)$ and $E(V_0,0)$ are the total energies of the lattice cells with and without strain, respectively. In fact, the number of independent elastic constants, to some degree, can be reduced by considering the crystal symmetry. Taking face-centered cubic structure as an example, there are only three independent elastic constants components, i.e., C_{11}, C_{12} and C_{44}, and the corresponding elastic energy can be calculated as,

$\Delta E(V,\epsilon) =$

$$\frac{V_0}{2}[\epsilon_1 \quad \epsilon_2 \quad \epsilon_3 \quad \epsilon_4 \quad \epsilon_5 \quad \epsilon_6]\begin{bmatrix} C_{11} & C_{12} & C_{12} & 0 & 0 & 0 \\ C_{12} & C_{11} & C_{12} & 0 & 0 & 0 \\ C_{12} & C_{12} & C_{11} & 0 & 0 & 0 \\ 0 & 0 & 0 & C_{44} & 0 & 0 \\ 0 & 0 & 0 & 0 & C_{44} & 0 \\ 0 & 0 & 0 & 0 & 0 & C_{44} \end{bmatrix}\begin{bmatrix} \epsilon_1 \\ \epsilon_2 \\ \epsilon_3 \\ \epsilon_4 \\ \epsilon_5 \\ \epsilon_6 \end{bmatrix} \tag{3.5}$$

By applying strain $\varepsilon = (0,0,0,\delta,\delta,\delta)$, $(\delta,-0.5\delta,-0.5\delta,0,0,0)$ and $(\delta,\delta,\delta,0,0,0)$ to the structure, respectively, the elastic energy can be rewritten as

$$\Delta E_1(V,\epsilon) = \frac{3}{2}\,V_0\,C_{44}\,\delta^2$$

$$\Delta E_2(V,\epsilon) = \frac{3}{2}\,V_0\,(C_{11} - C_{12})\,\delta^2$$

$$\Delta E_3(V,\epsilon) = \frac{3}{2}V_0\,(C_{11} + 2C_{12})\,\delta^2 \tag{3.6}$$

By solving Eqn. (3.6), the elastic constants C_{11}, C_{12} and C_{44} can be obtained, which thereby the bulk modulus can be computed by

$$B = \frac{1}{3}(C_{11} + 2C_{12}) \tag{3.7}$$

For each rocksalt structure in this work, the lattice parameters were set to be changed from the -0.03 to 0.03 Å with an increment of 0.005 Å along the strain axis mentioned as above. The second-order polynomial was used to fit the elastic energy and thus the elastic constants and bulk modulus can be consequently obtained.

3.2.4 LO-TO splitting and non-analytical term correction

The LO-TO splitting is a phenomenon that the degeneracy between the longitudinal optical mode (LO) and the transverse optical mode (TO) branched at the Brillouin zone center are lifted. This is happened in most of the ionic crystal structures, such as NaCl compound, for which the long-range electric fields associated with long wavelength phonons are responsible. It is known that the long wavelength optical mode is related to the opposite direction of the atomic motion in the unit cell. For the ionic crystal with different charges of the elements, this long wavelength limit will generate the different local electric field experienced by LO and TO mode due to the long-range character of the Coulomb interaction, which consequently leads to a gap between LO and TO branches in the phonon band structures.

In ionic crystal, the behavior of the dynamical matrix as $\boldsymbol{q} \to \mathbf{0}$ is better to be treated with LO-TO splitting in ionic structures. In the $\boldsymbol{q} \to \mathbf{0}$ limit, the dynamical matrix can be decomposed into the analytic and non-analytic contributions [141,158–162],

$$\begin{aligned} D_{\alpha\beta}^{NAC}(\boldsymbol{\kappa\kappa'}, \boldsymbol{q} \to \mathbf{0}) &= D_{\alpha\beta}(\boldsymbol{\kappa\kappa'}, \boldsymbol{q} = \mathbf{0}) + D_{\alpha\beta}^{NA}(\boldsymbol{\kappa\kappa'}, \boldsymbol{q} \to \mathbf{0}) \\ &= D_{\alpha\beta}(\boldsymbol{\kappa\kappa'}, \boldsymbol{q} = \mathbf{0}) + \frac{4\pi e^2}{V_0} \frac{\sum_\gamma q_\gamma Z^*_{\boldsymbol{\kappa},\gamma\alpha} \sum_{\gamma'} q_{\gamma'} Z^*_{\boldsymbol{\kappa},\gamma'\beta}}{\sum_{\alpha\beta} q_\alpha \epsilon^\infty_{\alpha\beta} q_\beta} \end{aligned} \tag{3.8}$$

where $\epsilon^\infty_{\alpha\beta}$ is the high-frequency static dielectric tensor, and $Z^*_{\boldsymbol{\kappa},\gamma\alpha}$ is the Born effective charge tensor of the atom $\boldsymbol{\kappa}$. Note that the splitting depends on the direction where one approaches the Γ point.

Therefore, nonanalytic component of the solution to the dynamical matrix is associated with the Born effective charges and the LO/TO splitting phenomenon. As a prerequisite, the static dielectric constant tensors and Born effective charge tensors should be calculated by density functional perturbation theory as implemented in VASP package, which these tensors are symmetrized by their space- and

point-group operations and a sum rule was employed in the Born effective charge tensors [163,164]. To obtain the Born effective charge tensors, the plane-wave cutoff energy of 400 eV was set and the Brillouin zones were sampled by 8 × 8 × 8 *k*-point mesh in reciprocal spaces of the unit cells of the rocksalt-type structures in calculations.

3.3 Results and discussion

3.3.1 Phonons

In this section, the phonon properties of the 32 binary compounds as mentioned in 3.2 obtaining by the temperature-dependent phonon calculations will be discussed. Before talking to the phonon results, the cation-anion radius ratios for these compounds are illustrated in figure 3.5 as a supplementary for simply determining the structural stability. Additionally, the mechanical stabilities for these rocksalt-type compounds were also examined through calculating the elastic constants and bulk moduli presented in table 3.1 and 3.2. It is obvious that the calculated bulk moduli are in good agreements with the experimental data at room temperature, which demonstrates the cells used in this work are mechanically stable.

All of the calculated phonon band structures along high-symmetry points and density of states are plotted in figure 3.6 - 3.9. In the periodic table shown in figure 3.1 (a), the atomic mass of the element from the top to the bottom of each group and that of the element from the left to the right of group becomes heavier. According to the Eqn. (2.19), for compounds in the group I-VII or II-VI, the phonon frequencies of the compound consisted of heavier cation and anion become systematically lower. It is also expected the phonon frequencies of compounds in the group I-VII become systematically lower than that in the group II-VI. For each compound, its phonon band structures consist of six branches, which are three acoustic and three optical branches, due to the primitive cell of each compound containing two atoms. From the figures, it is obvious that the longitudinal optic and transverse optic phonon modes are split at Γ center point, which is the feature of the ionic crystals. Note that at room temperature, all these rocksalt-type structures are dynamically stable without any imaginary frequencies shown in phonon band structures.

According to the lattice dynamical theory, the phonon band gap between the high and low frequency zones will be formed because of the large atomic mass difference. Here, we take LiX (X = F, Cl, Br, I) structures as the examples. For LiCl, LiBr and LiI compounds, there exists obvious band gaps between the acoustic and optic branches due to the larger atomic mass differences of 29, 73 and 120, whereas

for LiF compound there is no clear band gap due to the only small atomic mass difference of 12 between Li and F element. This can be clearly understood by the partial phonon density of states (PDOS), which describes the contributions of different atoms to the total PDOS. It is seen that, for LiF compound, the high-frequency optic phonons higher than 12 THz and the low-frequency acoustic phonons lower than 10 THz are dominated by the motion of Li and F atoms, respectively. At the frequency of 10 ~ 12 THz, there are mixed vibrational modes generated by Li and F atoms. However, the atomic mass differences, or equivalently, the mass ratios of LiCl, LiBr and LiI compounds larger than that of LiF compound lead to a separation between the high- and low-frequency branches. In general, the band gap becomes larger (smaller) as the absolute mass difference increases (decreases). Equivalently, the band gap is larger (smaller) as the atomic mass ratio increases (decreases). It should be reminded here that the atomic mass ratio is the cation and the anion mass ratio if the former is larger than the latter or the anion and the cation mass ratio otherwise. In addition, for LiCl, LiBr and LiI compounds, the high-frequency optic phonons and the low-frequency acoustic phonons are attributed to the motion of the cations and the anions, respectively. In fact, the light and heavy atoms mainly contribute to the high- and low-frequency branches, respectively. Apart from LiCl, LiBr and LiI, this is apparently observed in those compounds with an explicit band gap such as I-VII compounds of NaBr, NaI, KBr, KI, RbF, RbCl, and II-VI compounds of MgSe, MgTe, CaTe, SrO, BaO, BaS. The rest of the compounds without a band gap, the mixing contributions to the branches are quite complex.

Furthermore, the flatness of the TO branches along all of the symmetry paths of LiBr and LiI compounds are illustrated as the clearly sharpest peaks at the frequency around 6 THz in their phonon densities of states. The nearly flat TO branches can also be found in phono band structures of NaI, RbF, MgTe, SrS and BaS compounds, which the atomic mass differences of these compounds are relatively larger than that of the remaining compounds. In addition, it is found that there is an intersection of the LA and TO branches along the symmetry path of Γ-X in the phonon band structures of LiF compound. This leads to the phenomenon that for the small $\boldsymbol{q}$ vectors approaching to the Γ point, the frequencies of the TO branches should be higher than that of the LA branches, whereas for the large $\boldsymbol{q}$ vectors the LA branches are above the TO branches. For the remaining three compounds, the relationship among the four kinds of phonon branches can be observed as LO > TO > LA > TA. The LO phonon branches of all these compounds show relatively large dispersion extent along the symmetry path of Γ-X, which is explained as the atomic arrangement and bonding of the rocksalt structure.

In order to further understand the temperature dependence of the phonon properties, the phonon band structures at different temperatures are investigated. Here, still taking NaCl as an example, the phonon band structures and densities of states at 80, 300, 500, 800 and 1000 K are calculated. The phonon band structures where the lattice thermal expansion [165] is also taken into account are plotted in figure

3.10 (a). The phonon band structures soften slowly as the temperature increases from 80 to 300 K and the softening extent becomes stronger as the temperature increases from 300 K. The phonon frequencies of TO and LO branches at Γ point are changed within about 0.5 and 0.4 THz, respectively, and the phonon densities of states are slightly moved to lower frequencies as the temperature increases. On the contrary, the temperature dependence of the phonon band structures harden dramatically as the temperature increases without considering the lattice thermal expansion effect, and the phonon densities of states are moved in an opposite direction to the higher frequencies compared with those in figure 3.10 (a). From the figure 3.10 (b), it is seen that the hardening extent of TO and LO branches at Γ point are about 0.8 and 0.5 THz, respectively. As a comparison, the phonon band structures with only the lattice thermal expansion effect considered are also plotted as shown in figure 3.10 (c). The phonon band structures soften quickly as the temperature increases, which is evidently seen that the phonon frequencies of TO and LO branches at Γ point change with about 1.7 and 1 THz, respectively. Although the trend of the phonon dispersion curves with increased temperature are same as those considered with both the temperature and thermal expansion effects, the rate of phonon softening are different, which the former show a stronger temperature dependence than the latter.

The calculated temperature-dependent phonon frequencies of TO and LO branches at Γ point in Brillouin zone are illustrated in figure 3.11 (a). As a comparison, some available experimental [166] and theoretical [109] data are also presented. It is found that the calculated TO branches by including the temperature and lattice expansion effects in this work are in both qualitatively and quantitatively good match with that of the available measurements and previous phonon calculations including the 4^{th} order anharmonicity from 100 to 600 K, which all of them show the weak temperature dependence. The calculated phonon frequencies of LO braches soften by 0.2 THz from 100 to 600 K and 0.4 THz from 100 to 1000 K, respectively, and unfortunately there is no direct data to refer. It should be emphasized that despite the calculated results of the previous and present theoretical work are precisely close, the computational cost of the latter is much cheaper due to the fourth-order anharmonic term is not considered. Additionally, in the previous study, the phonon frequencies computed by phonon calculations in quasiharmonic approximation (QHA) change significantly as the temperature increases. In particular, the TO branches mostly soften by more than 1 THz from 100 to 600 K. Contrary to the poor performance of QHA calculations, our approach of the temperature-dependent phonon calculations including both of the temperature and thermal expansion effects is valid and accurate for the rocksalt-type structures at finite temperatures. This is also expected to be useful for understanding the lattice dynamical properties of those strongly anharominc materials while the conventional phonon calculations are inadequate for predicting that.

The distributions of randomly atomic displacements generated at different temperatures are displayed in figure 3.11 (b). Each sample corresponds to the displacement of one atom deviated from its equilibrium position at the current self-consistent step. The total number of one atomic configuration at each step are same, i.e., 100 atomic configurations per step, which then the total number of samples for displacements are 6400 per iteration. The probability density function of the normal distributions of the first and final step are almost overlapped at 80 and 300 K whereas those curves are different from 500 to 1000 K, which means that it is easier to obtain the convergence of the calculations at lower temperatures. As the temperature increases, the mean displacement of the samples at the finally converged step becomes larger, which is about 0.13, 0.21, 0.28, 0.33, and 0.4 Å, respectively. The variance value of the samples becomes larger manifested by that the distribution curve becomes wider and the central peak becomes shorter, which means the more randomly atomic configurations are generated by the higher temperatures. Noticed that it is more difficult to obtain the converged force constants if there exists strongly random displacements, since the lack of the crystal symmetry and even seriously distorted cell and results in more calculation iterations and computationally costs. Therefore, by the random displacements method, a number of the atomic configurations are suitably chosen per iteration, which well mimics the variously vibrations in a thermally populated supercell with the temperature-affected displacements rather than the fixed small ones.

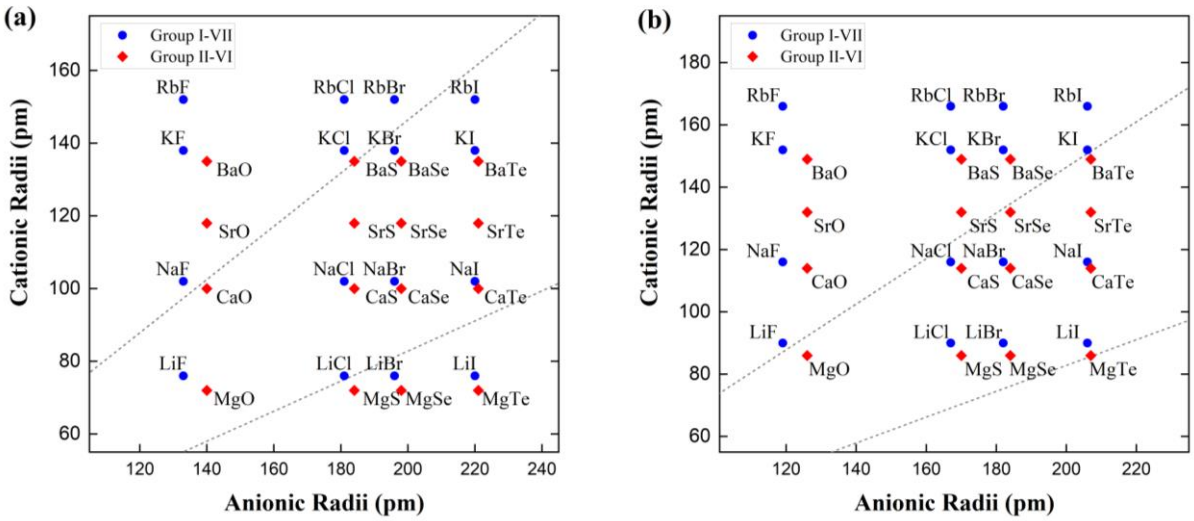

Figure 3.5. Ionic radii of cations and anions defined by (a) Pauling and (b) Shannon, respectively. Here, 32 rocksalt-type compounds of the group I-VII and II-VI compounds are denoted as blue circles and red diamonds, respectively. The dashed grey lines represent the minimum radius ratio of a stable ionic geometry of octahedron and cube, respectively.

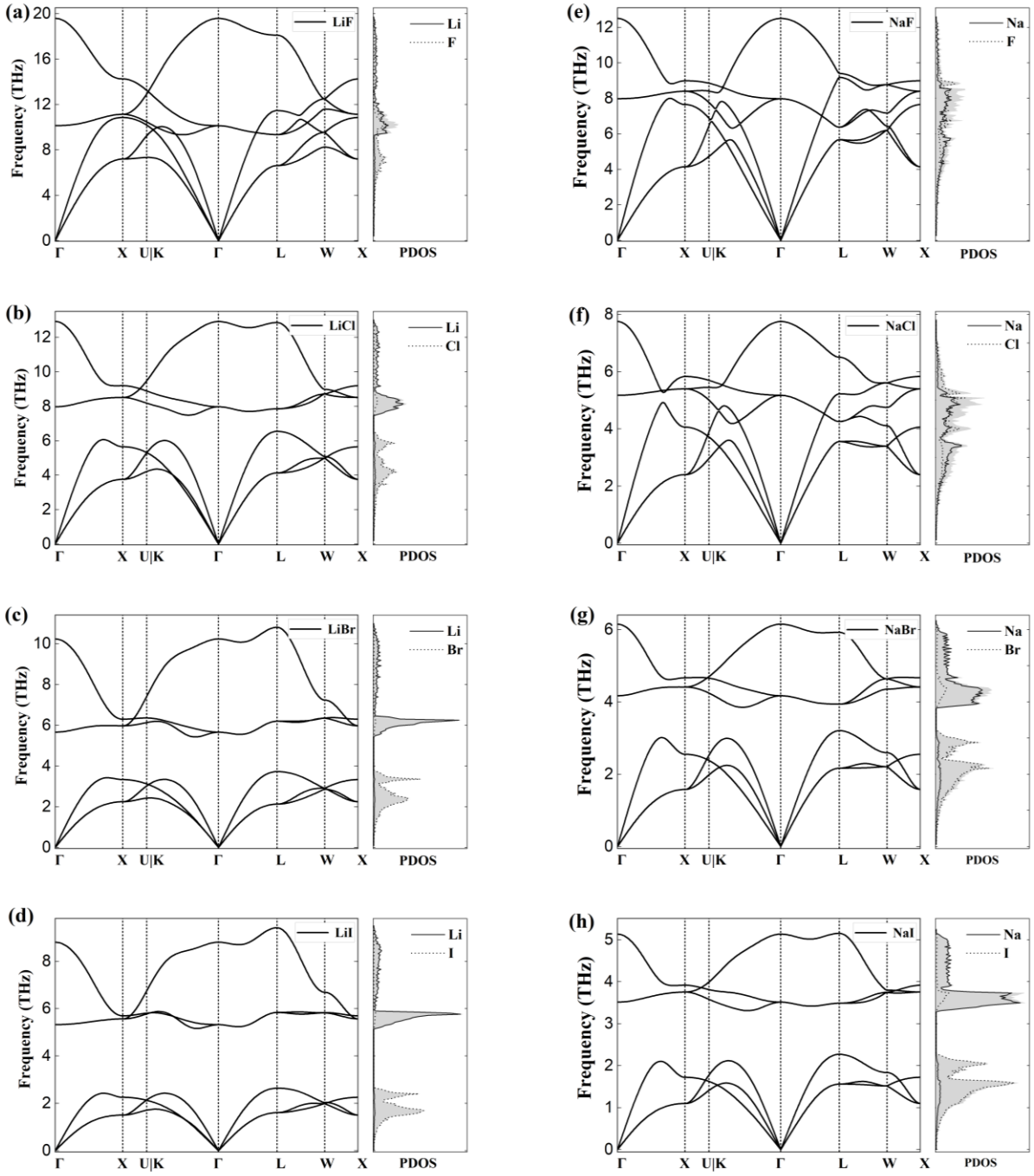

Figure 3.6. Phonon band structures and phonon densities of states (PDOS) of (a) LiF, (b) LiCl, (c) LiBr, (d) LiI, (e) NaF, (f) NaCl, (g) NaBr and (h) NaI. Each PDOS curve is plotted on the right hand side of the corresponding phonon band structure. In PDOS, contributions of cation and anion of each compound to the total PDOS (shaded area) are denoted as solid and dashed black lines, respectively.

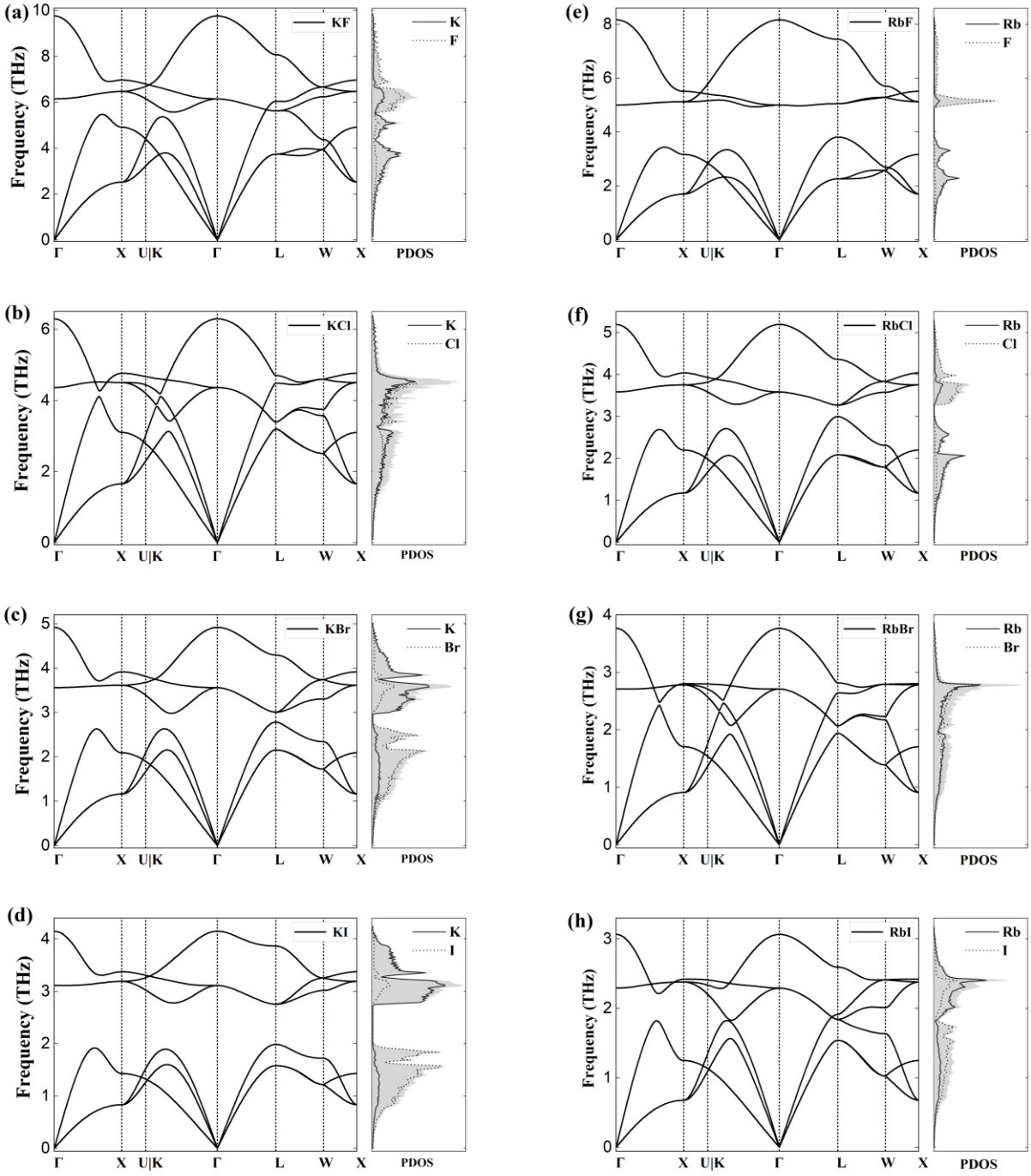

Figure 3.7. Phonon band structures and phonon densities of states (PDOS) of (a) KF, (b) KCl, (c) KBr, (d) KI, (e) RbF, (f) RbCl, (g) RbBr and (h) RbI. Each PDOS curve is plotted on the right hand side of the corresponding phonon band structure. In PDOS, contributions of cation and anion of each compound to the total PDOS (shaded area) are denoted as solid and dashed black lines, respectively.

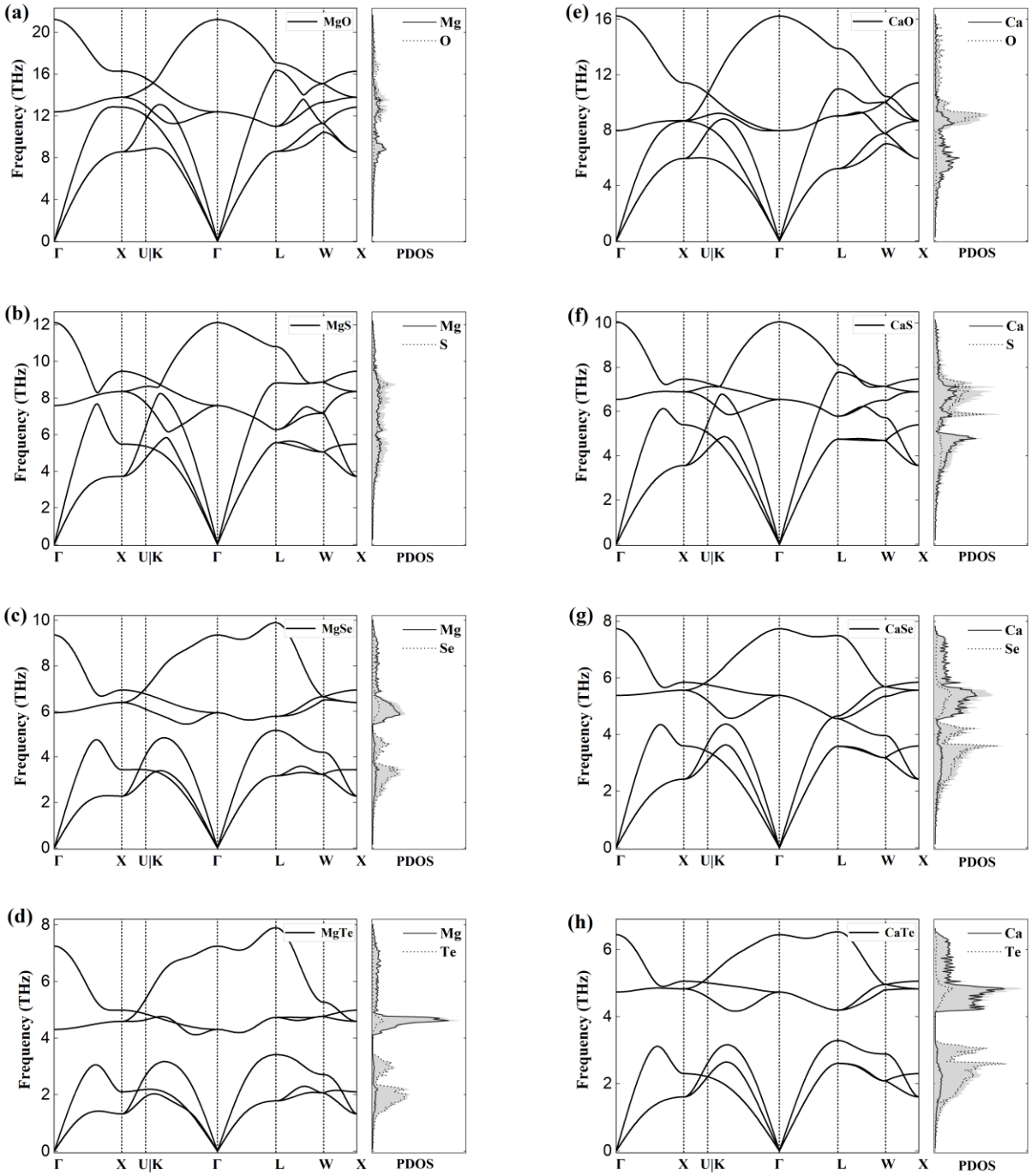

Figure 3.8. Phonon band structures and phonon densities of states (PDOS) of (a) MgO, (b) MgS, (c) MgSe, (d) MgTe, (e) CaO, (f) CaS, (g) CaSe and (h) CaTe. Each PDOS curve is plotted on the right hand side of the corresponding phonon band structure. In PDOS, contributions of cation and anion of each compound to the total PDOS (shaded area) are denoted as solid and dashed black lines, respectively.

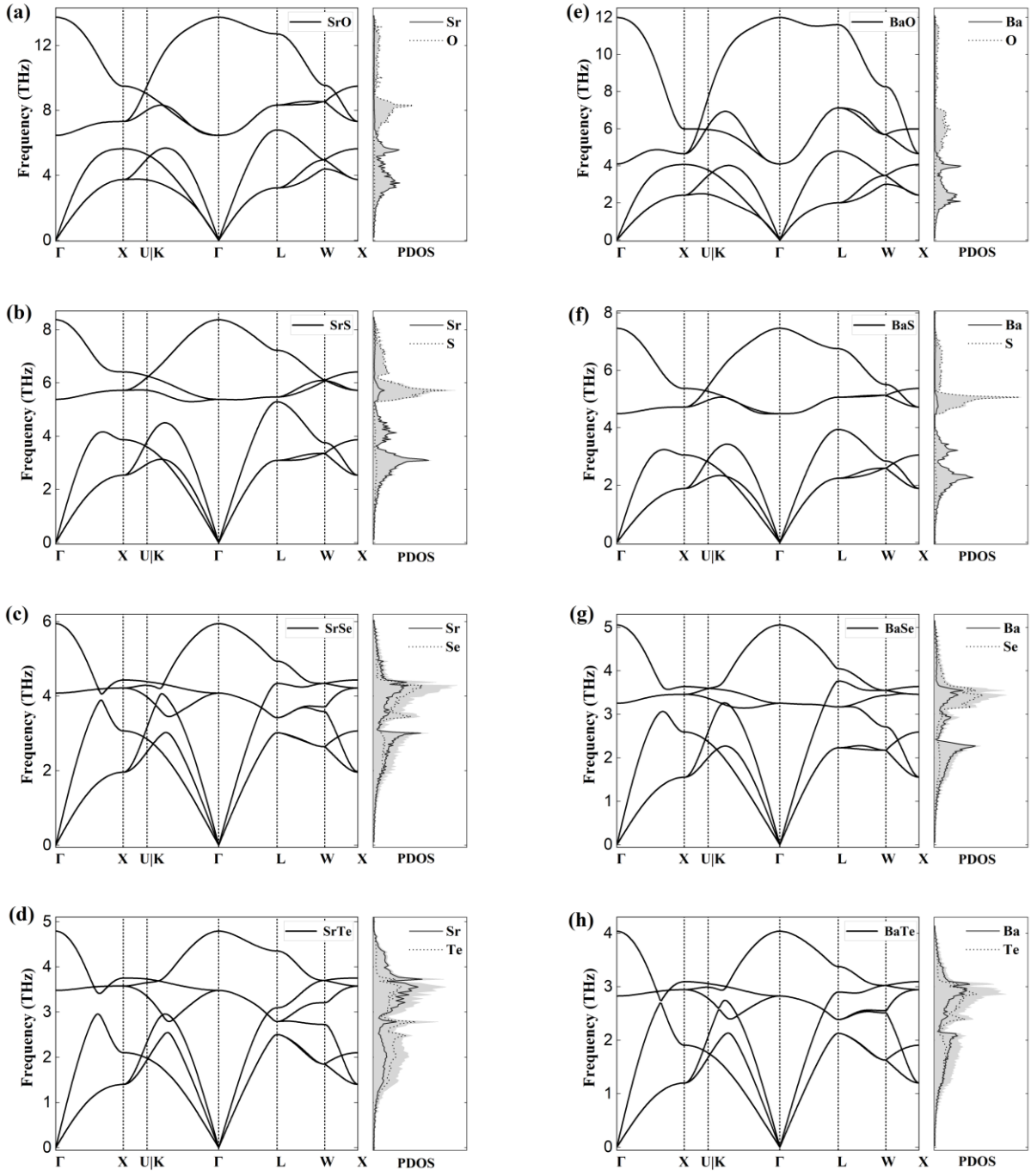

Figure 3.9. Phonon band structures and phonon densities of states (PDOS) of (a) SrO, (b) SrS, (c) SrSe, (d) SrTe, (e) BaO, (f) BaS, (g) BaSe and (h) BaTe. Each PDOS curve is plotted on the right hand side of the corresponding phonon band structure. In PDOS, contributions of cation and anion of each compound to the total PDOS (shaded area) are denoted as solid and dashed black lines, respectively.

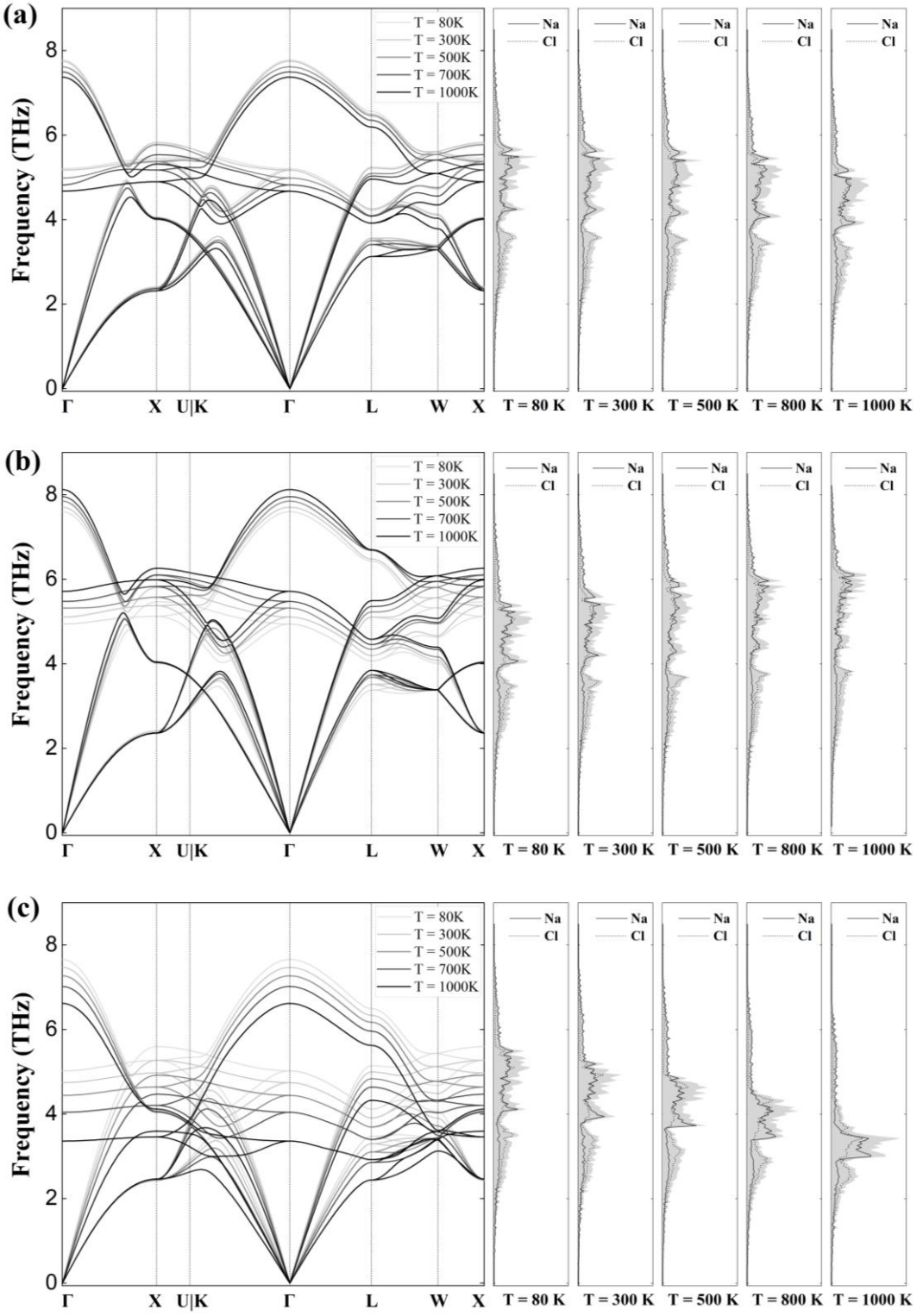

Figure 3.10. Phonon band structures and phonon densities of states of NaCl compound at 80, 300, 500, 700 and 1000 K by considering (a) temperature and lattice thermal expansion effects, (b) temperature effect, and (c) lattice thermal expansion effect. In phonon band structures, the temperature changes from low to high denoted by solid lines with the color from light to dark. In phonon densities of states, the contributions of Na and Cl atoms to the total PDOS (shaded area) are denoted as solid and dashed black lines, respectively.

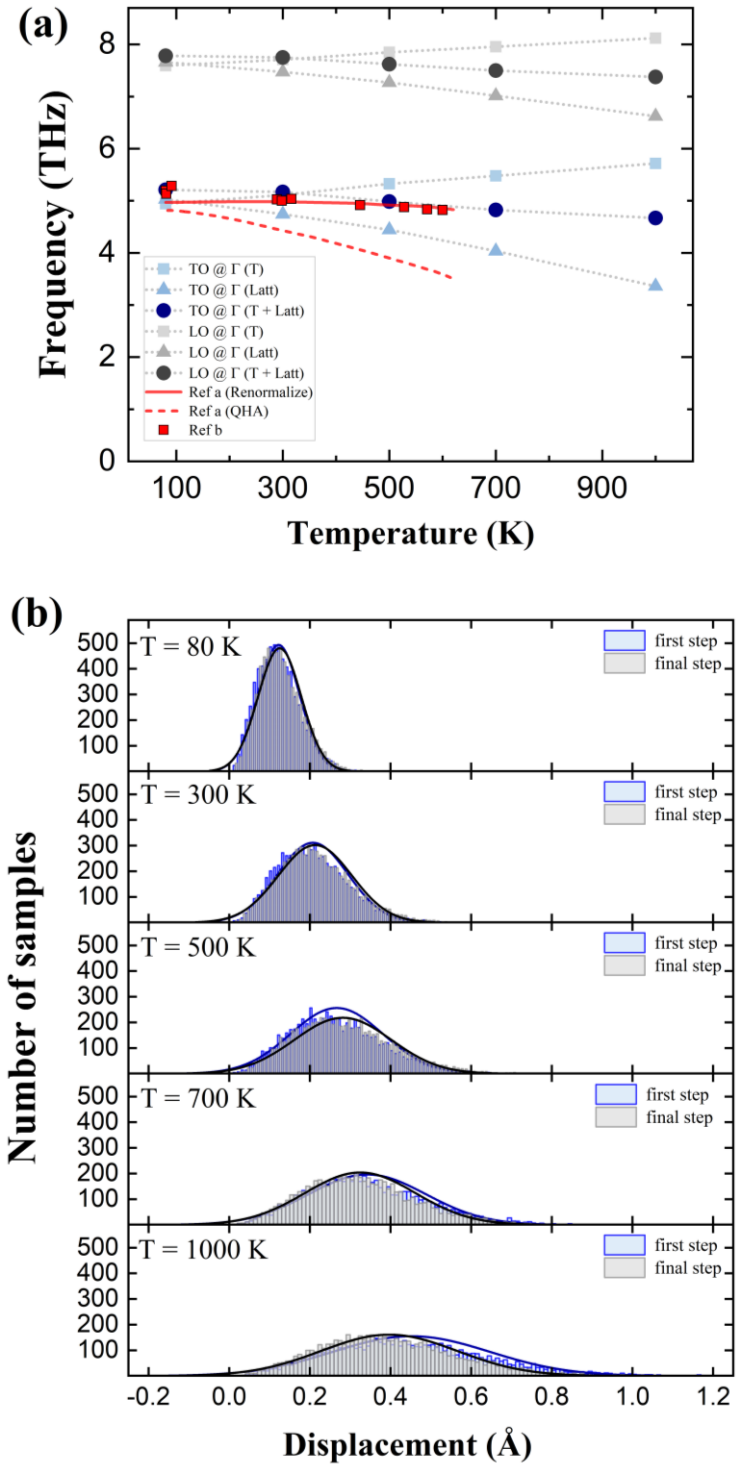

Figure 3.11. Temperature-dependent (a) phonon frequencies of the TO and LO branches at Γ point in the Brillouin zone and (b) distributions of atomic displacements generated by random displacements method. In panel (a), all the data are calculated in this work except the renormalization and QHA calculations [109] denoted as Ref. a and the measurements [166] denoted as Ref. b. In panel (b), the solid blue and black lines are the probability density function of the normal distribution to which the data fit.

3.3.2 Lattice thermal conductivity

From the previous discussion, it is known that using temperature-dependent phonon calculations, the second-order force constants can be well estimated by a large number of force-displacement datasets. In terms of the lattice thermal conductivity (LTC), it is required to estimate at least the third-order force constants for calculating the phonon-phonon interactions. In present work, the calculated LTC values of 32 rocksalt-type compounds are listed in table 3.4. As a comparison, the calculated LTC without the phonon-isotope scattering are also presented in table 3.5. It is found that for some compounds the phonon-isotope scattering effect significantly reduces the LTC value whereas for some compounds it has negligible impact. The maximum and minimum of the reductions when considering phonon-isotope scattering are about 18 % and 0.1 %, respectively. Notice that the all the LTC values in this work implicitly comprise the phonon-isotope scattering effect, since it is a natural phenomenon and generally considered by the measurements and other calculations. Additionally, in the next discussion the calculated LTC values in this work are default as the results calculated by SMRTA method, since they are much closer to the experimental data compared with that of the LBTE method.

To have a direct look of these results, the calculated LTC are shown in figure 3.12 with respect to the available measurements [167,168]. In figure 3.12 (a), 18 rocksalt compounds are shown and their calculated and experimental LTC are very close. Among them, 14 compounds are also compared with previous theoretical LTC values [110]. In figure 3.12 (b), the LTC values obtained by the conventional calculation based on the harmonic phonon calculation including the three phonon scattering as perturbation (simply called HA + 3ph) are denoted as red triangles. The LTC values calculated by solving self-consistent phonon equation considering the first-order correction from quartic-order anharmonic term (simply called SCP 3 + 4ph) are denoted as grey diamonds. It is obvious that the LTC computed by the HA + 3ph calculations tend to generally underestimate the experimental values, which is confirmed as in the same trend as the other theoretical work. By including up to four-phonon interactions into self-consistent phonon equation, the calculated LTC values tend to be lower than that of the HA+3ph calculations. Note that the LTC of NaF and BaO calculated in this work are higher than experimental values whereas they are to be largely reduced and close to the measurements in both of the HA + 3ph and SCP 3 + 4ph calculations. This is mainly due to the different lattice parameters used in calculations, which is known to all that the inclusion of the lattice thermal expansion will more or less influence the phonon frequencies. In this work, the lattice parameters are chosen to be the room temperature experimental data, which are generally smaller than those parameters optimized by PBE functional in the theoretical study. Moreover, the error of measurements and the different models of LTC may results in the discrepancies. Despite the difference exists, all these calculated LTC values are in the same order of magnitude as the experimental ones.

The calculated LTC are also shown as a function of the primitive cell volume per atom (figure 3.12 (c)) and the mass ratio of cation and anion in each compound (figure 3.12 (d)), respectively. The trend of distribution in the former scatter is similar to the previous theoretical study [169]. From the latter scatter, it is found that the LTC value tend to be lower when the discrepancy of the cation and anion mass becomes larger. From the above analyses, the high-throughput LTC values for rocksalt-type compounds calculated in this work are comparable to the experimental measurements, which verifies that this temperature-dependent phonon approach is universally applicable to the rocksalt-type structure and is important to accurately predict their heat transfer properties.

To understand the underlying mechanisms of the LTC for these rocksalt-type compounds, the $(\boldsymbol{qj})$ mode-contribution $\kappa_{\boldsymbol{qj}}$ to the LTC are analyzed, which is defined [40] based on the Eqn. (2.50) as

$$\kappa_{\boldsymbol{qj}} = \frac{1}{V_0} C_{\boldsymbol{qj}} \boldsymbol{v}_{\boldsymbol{qj}} \otimes \boldsymbol{v}_{\boldsymbol{qj}} \tau_{\boldsymbol{qj}} \tag{3.9}$$

The corresponding cumulative LTC is defined as

$$\kappa^c(\omega) = \int_0^{\omega} \frac{1}{N} \sum_{\boldsymbol{qj}} \kappa_{\boldsymbol{qj}} \delta\left(\omega' - \omega_{\boldsymbol{qj}}\right) d\omega' \tag{3.10}$$

Then the mode-contribution of LTC for each compound as a function of the phonon frequency are plotted. From the figure 3.13-3.20 (a), it is found that the high- and low-frequency phonon modes play the different roles in the LTC, since the former and the later make little and much contributions to the total LTC values, respectively. As shown in Eqn. (3.9), the mode-contribution LTC is consisted of the mode-heat capacity, group velocity and lifetime. To clearly understand how each component influence the LTC, the lifetimes and heat capacities with respect to the phonon frequencies are also displayed in figure 3.13-3.20 (b) and (c), respectively. Here, taking NaCl compound as an example to discuss. In figure 3.21 (a), as the phonon frequency increases from the 2 THz, the cumulative LTC increases rapidly, while it becomes stable as almost a constant when the frequency is higher than 5.5 THz. The cumulative LTC values are dominated up to almost 79 % by those phonon modes whose frequencies are between 2 and 5.5 THz. The distribution of the outer-product of the group velocities as a function of the phonon frequency is defined as [40],

$$w(\omega) = \frac{1}{NV_0} \sum_{\boldsymbol{qj}} \boldsymbol{v}_{\boldsymbol{qj}} \otimes \boldsymbol{v}_{\boldsymbol{qj}} \, \delta\left(\omega - \omega_{\boldsymbol{qj}}\right) \tag{3.11}$$

As shown in figure 3.21 (b), $w(\omega)$ curve shows a similar contour as the mode-contribution LTC curve, which in the former the major distribution of the phonon modes in $w(\omega)$ is assembled when the phonon frequencies are between 2 and 5.5 THz. It is evidently that the distribution still exists when the frequencies are higher than 5.5 THz while the mode-contribution LTC value is almost vanished. As a comparison, in figure 3.21 (c), most of the phonon modes whose frequencies are lower than 5.5 THz have relatively larger lifetimes while those whose frequencies higher than 5.5 THz have constantly small lifetimes. Some of the phonon modes whose frequencies are lower than 2 THz have very long lifetimes. Furthermore, the mode heat capacity of overall the phonon frequency is almost a constant. Therefore, the mode-contribution LTC of the phonon modes whose frequencies are higher than 5.5 THz, is mainly influenced by those almost vanished phonon lifetimes in spite of the nonzero distribution of $w(\omega)$ at higher frequencies.

Furthermore, the three-phonon scattering rates (inverse of phonon lifetimes) of 32 rocksalt-type compounds are illustrated in figure 3.22 (I-VII) and 3.23 (II-VI). The phonon scattering rates are found to relate to the phonon densities of states. When there are sharper peaks shown in the PDOS at a certain phonon frequency range, the corresponding phonon modes have higher phonon scattering rates. On the contrary, when the PDOS at a certain frequency range are more flatten, the corresponding phonon scattering are relatively lower. In particular, this phenomenon is apparent for the decay processes where the distributions of the phonon scattering rates at a certain frequency range are generally larger than that for the collision processes. In addition, the phonon scattering rates arising from the collision processes are generally larger than that arising from the decay processes. As discussed in section 3.3.1, the sharp peaks shown in PDOS owing to the small extent of the dispersion of the phonon branches, which is further related to the large mass differences between the cations and anions. For those compounds whose atomic mass differences are small, their PDOS curves are flatten and less sharp peaks, which thereby the phonon scattering rates over all phonon frequencies are stable. Hence, it is considered that the atomic mass difference of the cation and anion in the rocksalt structure has an important impact on the phonon scattering rates.

Table 3.4. Calculated LTC values at room temperature of 32 rocksalt-type compounds. The available experimental values [167,168] are also presented in this table.

I-VII	SMRTA	LBTE	Expt.	II-VI	SMRTA	LBTE	Expt.
LiF	17.92	19.68	17.6	MgO	60.46	68.53	60.0
LiCl	7.21	7.51		MgS	22.08	23.57	
LiBr	2.90	3.05	2.3	MgSe	9.40	9.83	
LiI	2.10	2.25		MgTe	3.11	3.15	
NaF	28.19	34.58	18.4	CaO	23.16	24.85	27.0
NaCl	7.12	8.00	7.1	CaS	26.11	29.69	
NaBr	3.33	3.49	2.8	CaSe	14.95	15.37	
NaI	1.92	2.05	1.8	CaTe	9.13	9.31	
KF	8.68	9.39	7.8	SrO	10.87	11.15	12.0
KCl	7.38	8.85	7.1	SrS	10.13	10.51	
KBr	3.32	3.41	3.4	SrSe	16.76	19.01	
KI	2.63	2.79	2.6	SrTe	10.25	10.63	
RbF	3.29	3.42	2.9	BaO	4.04	4.43	2.3
RbCl	3.15	3.23	2.8	BaS	5.95	6.22	
RbBr	3.75	4.45	3.8	BaSe	10.30	11.10	
RbI	2.27	2.41	2.3	BaTe	9.43	10.53	

Table 3.5. Calculated LTC values without the phonon-isotope scattering at room temperature.

I-VII	SMRTA	LBTE	II-VI	SMRTA	LBTE
LiF	18.27	20.30	MgO	74.104	88.25
LiCl	7.61	7.99	MgS	24.40	26.41
LiBr	2.99	3.16	MgSe	9.91	10.45
LiI	2.11	2.26	MgTe	3.19	3.24
NaF	28.19	34.58	CaO	24.46	26.52
NaCl	7.47	8.45	CaS	29.51	34.39
NaBr	3.37	3.53	CaSe	16.99	17.65
NaI	1.92	2.05	CaTe	9.60	9.83
KF	8.82	9.56	SrO	10.91	11.19
KCl	7.66	9.35	SrS	10.26	10.68
KBr	3.35	3.45	SrSe	18.79	22.12
KI	2.63	2.79	SrTe	10.74	11.22
RbF	3.30	3.44	BaO	4.05	4.44
RbCl	3.19	3.28	BaS	6.00	6.30
RbBr	3.79	4.53	BaSe	10.81	11.78
RbI	2.28	2.41	BaTe	9.93	11.26

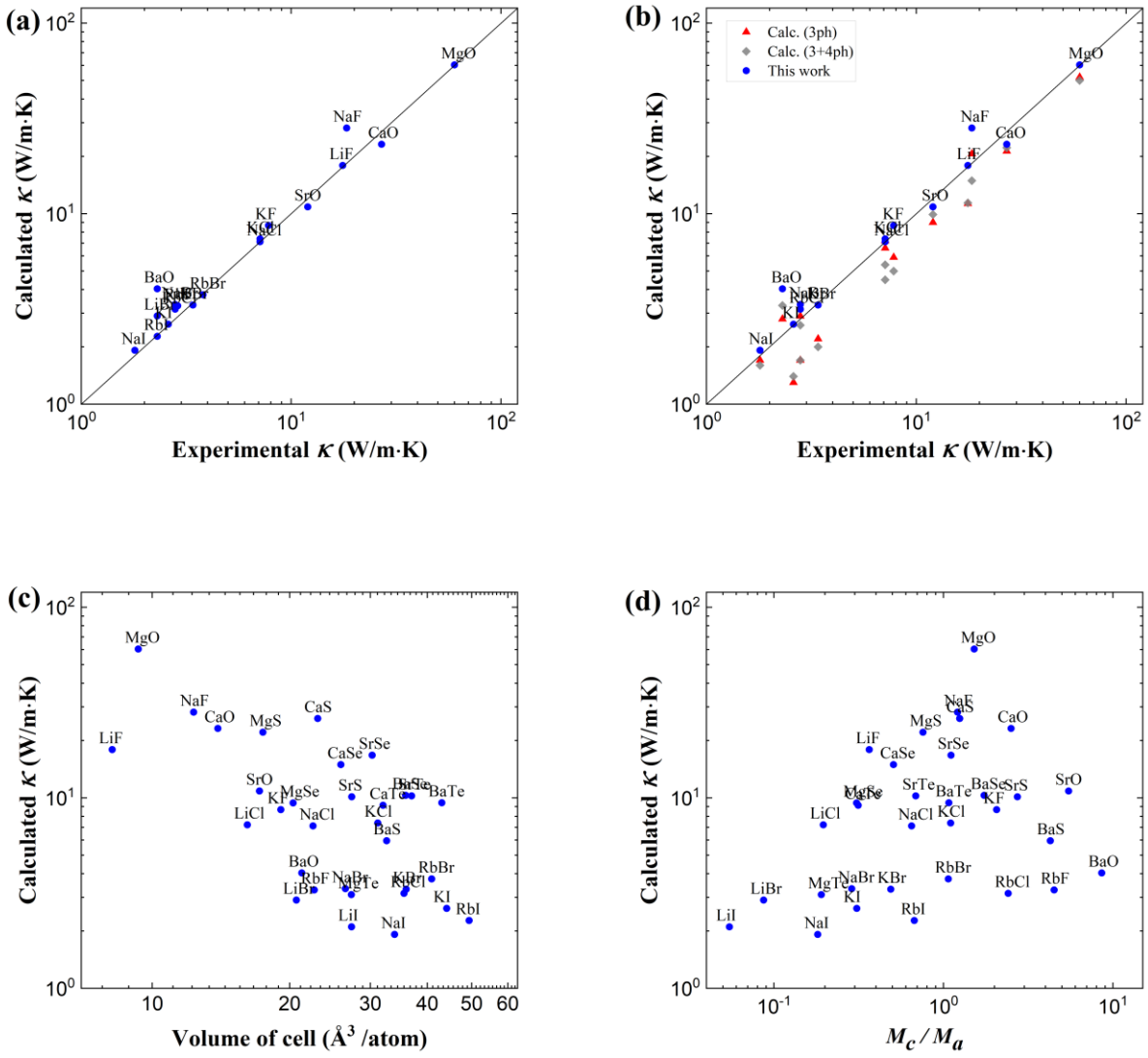

Figure 3.12. Calculated LTC values of the selected rocksalt-type compounds at 300 K with respect to (a) and (b) available experimental lattice thermal conductivities, (c) volume of the compounds, and (d) atomic mass ratio of cation and anion. All the calculated data using present approach are marked as blue circles. In panel (a) 18 rocksalt-type compounds are plotted regarding the experimental data [167,168]. In panel (b), 14 rocksalt-type compounds are shown as comparison, and the theoretical data [110] calculated considering 3-phonon and 3+4-phonon interactions in panel are marked as red triangles and grey diamonds, respectively.

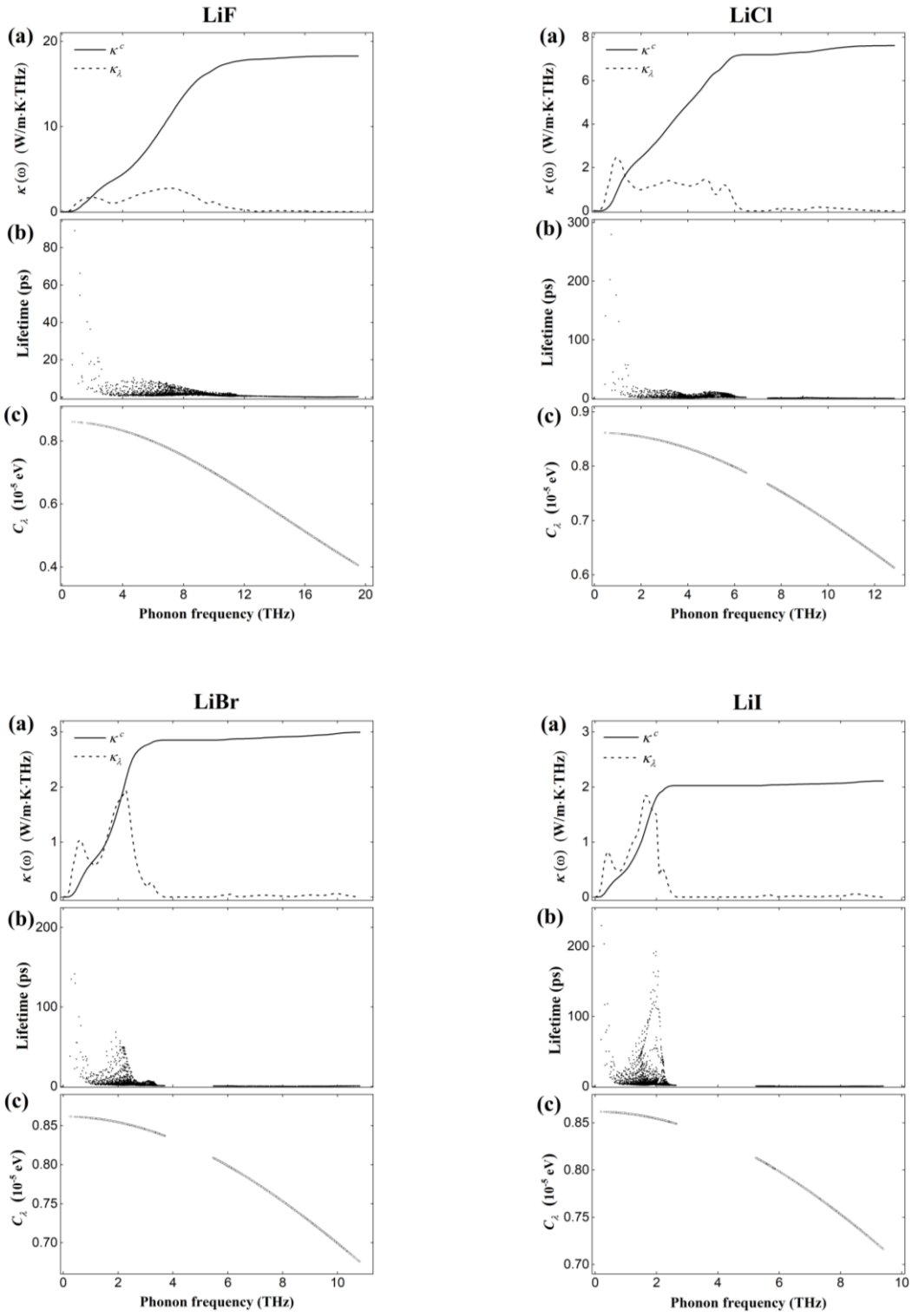

Figure 3.13. Thermodynamic properties of LiX (X = F, Cl, Br, I) compounds. (a) Cumulative (solid black lines) and mode contributions (dashed black lines) of the calculated LTC values $\kappa(\omega)$ at 300 K, respectively. (b) Phonon lifetimes at 300 K. Each dot corresponds to a phonon mode sampled in the Brillouin zones. (c) Mode heat capacities at 300 K. Each circle corresponds to a phonon mode sampled in the Brillouin zones.

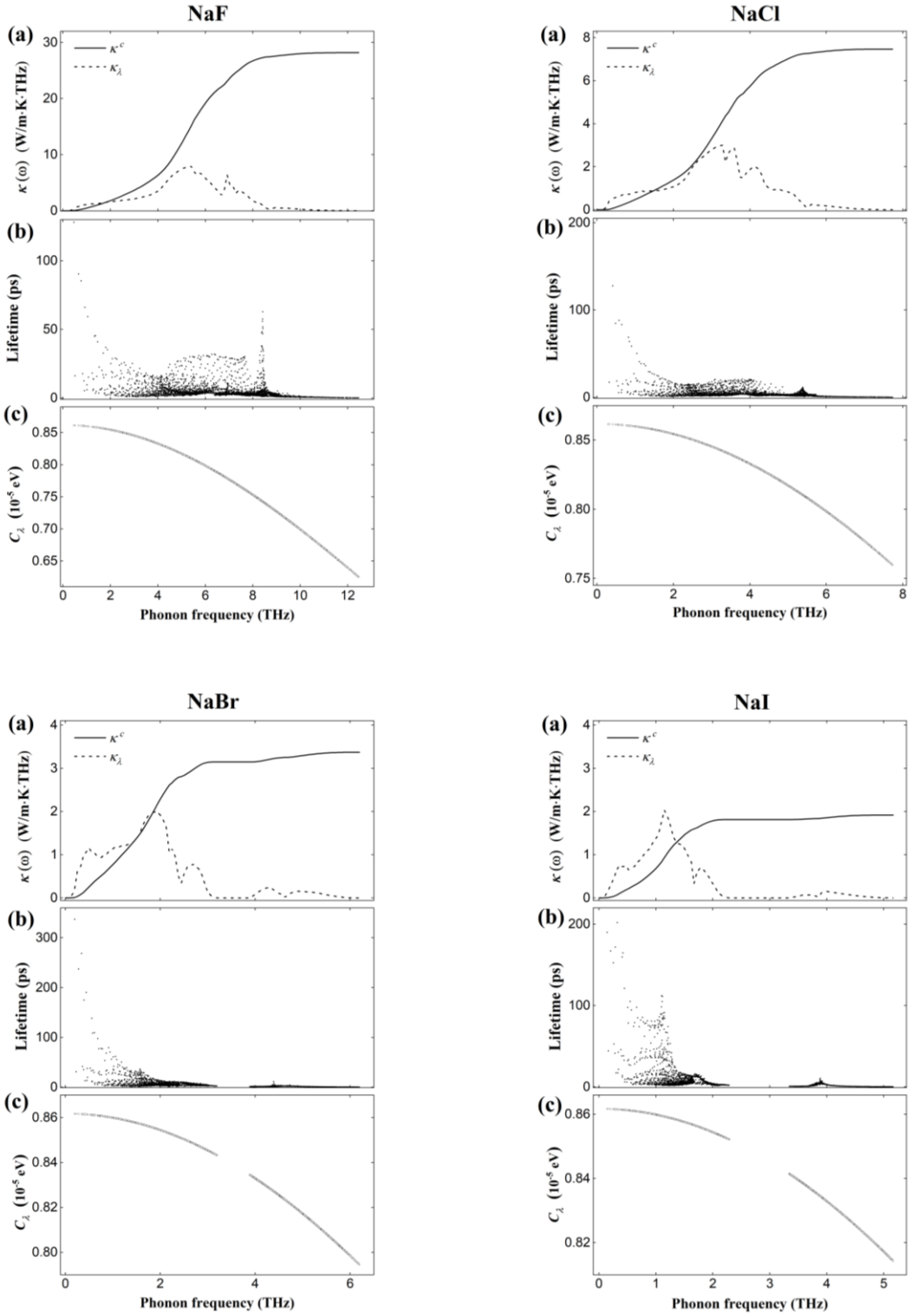

Figure 3.14. Thermodynamic properties of NaX (X = F, Cl, Br, I) compounds. (a) Cumulative (solid black lines) and mode contributions (dashed black lines) of the calculated LTC values $\kappa(\omega)$ at 300 K, respectively. (b) Phonon lifetimes at 300 K. Each dot corresponds to a phonon mode sampled in the Brillouin zones. (c) Mode heat capacities at 300 K. Each circle corresponds to a phonon mode sampled in the Brillouin zones.

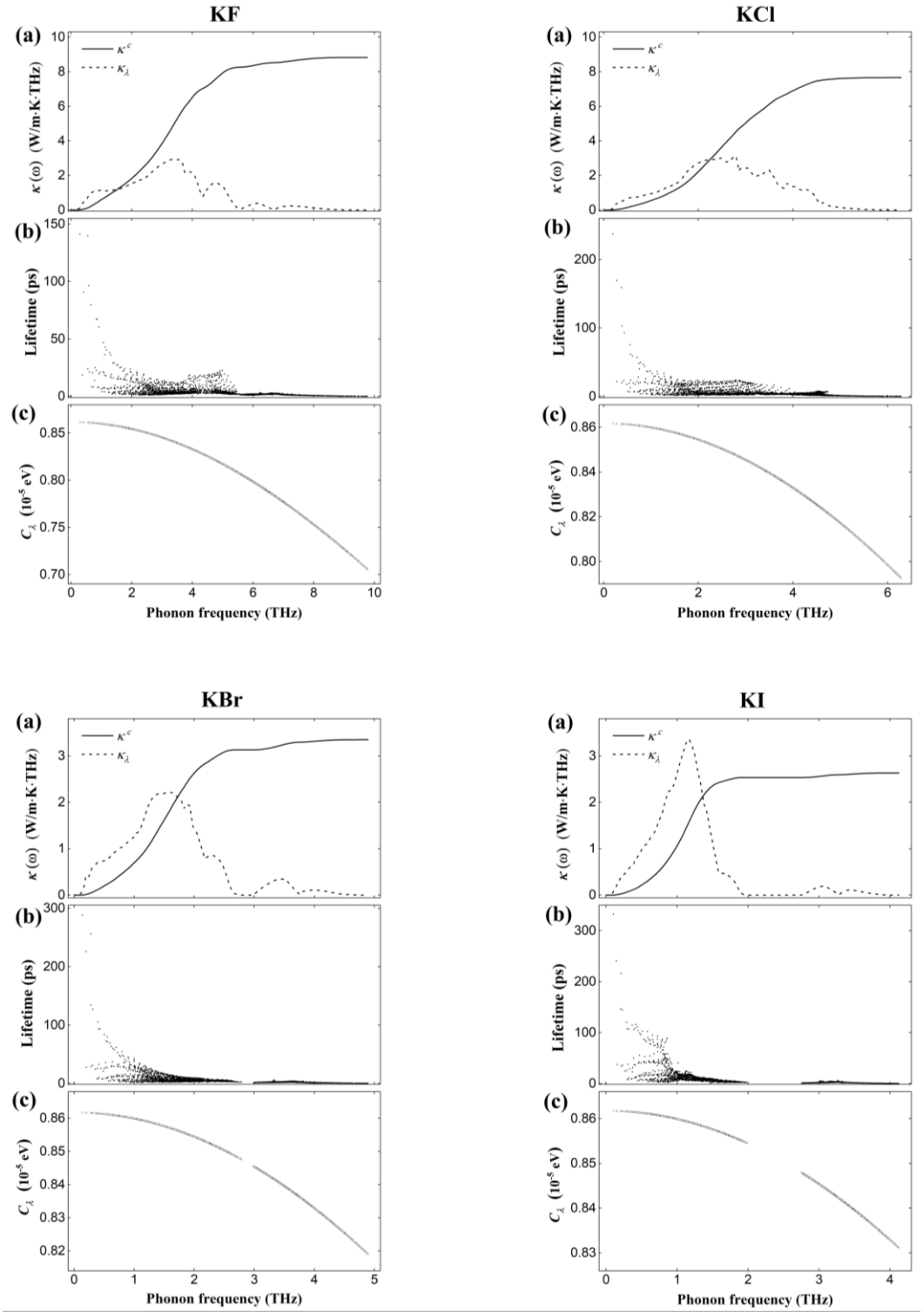

Figure 3.15. Thermodynamic properties of KX (X = F, Cl, Br, I) compounds. (a) Cumulative (solid black lines) and mode contributions (dashed black lines) of the calculated LTC values $\kappa(\omega)$ at 300 K, respectively. (b) Phonon lifetimes at 300 K. Each dot corresponds to a phonon mode sampled in the Brillouin zones. (c) Mode heat capacities at 300 K. Each circle corresponds to a phonon mode sampled in the Brillouin zones.

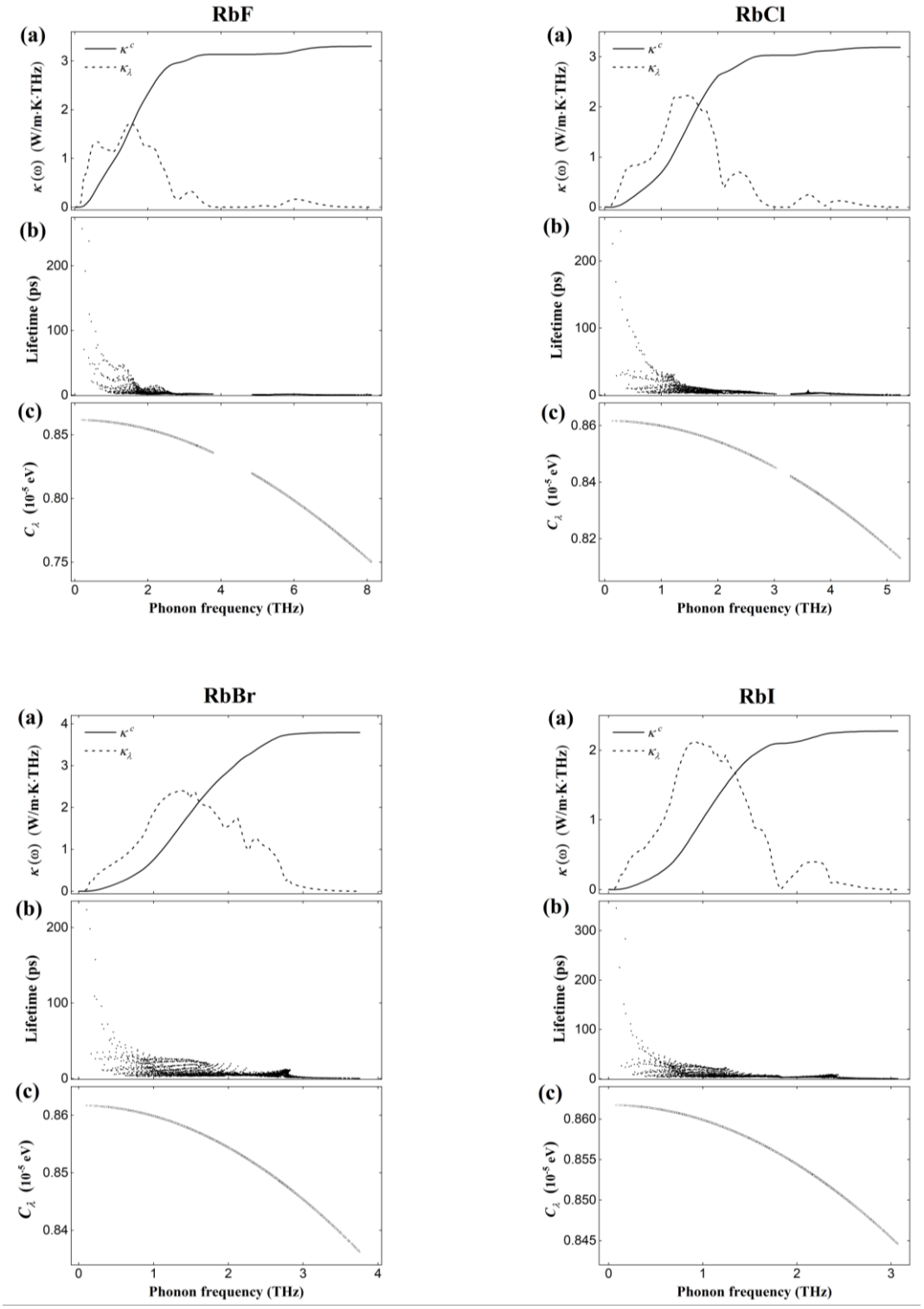

Figure 3.16. Thermodynamic properties of RbX (X = F, Cl, Br, I) compounds. (a) Cumulative (solid black lines) and mode contributions (dashed black lines) of the calculated LTC values $\kappa(\omega)$ at 300 K, respectively. (b) Phonon lifetimes at 300 K. Each dot corresponds to a phonon mode sampled in the Brillouin zones. (c) Mode heat capacities at 300 K. Each circle corresponds to a phonon mode sampled in the Brillouin zones.

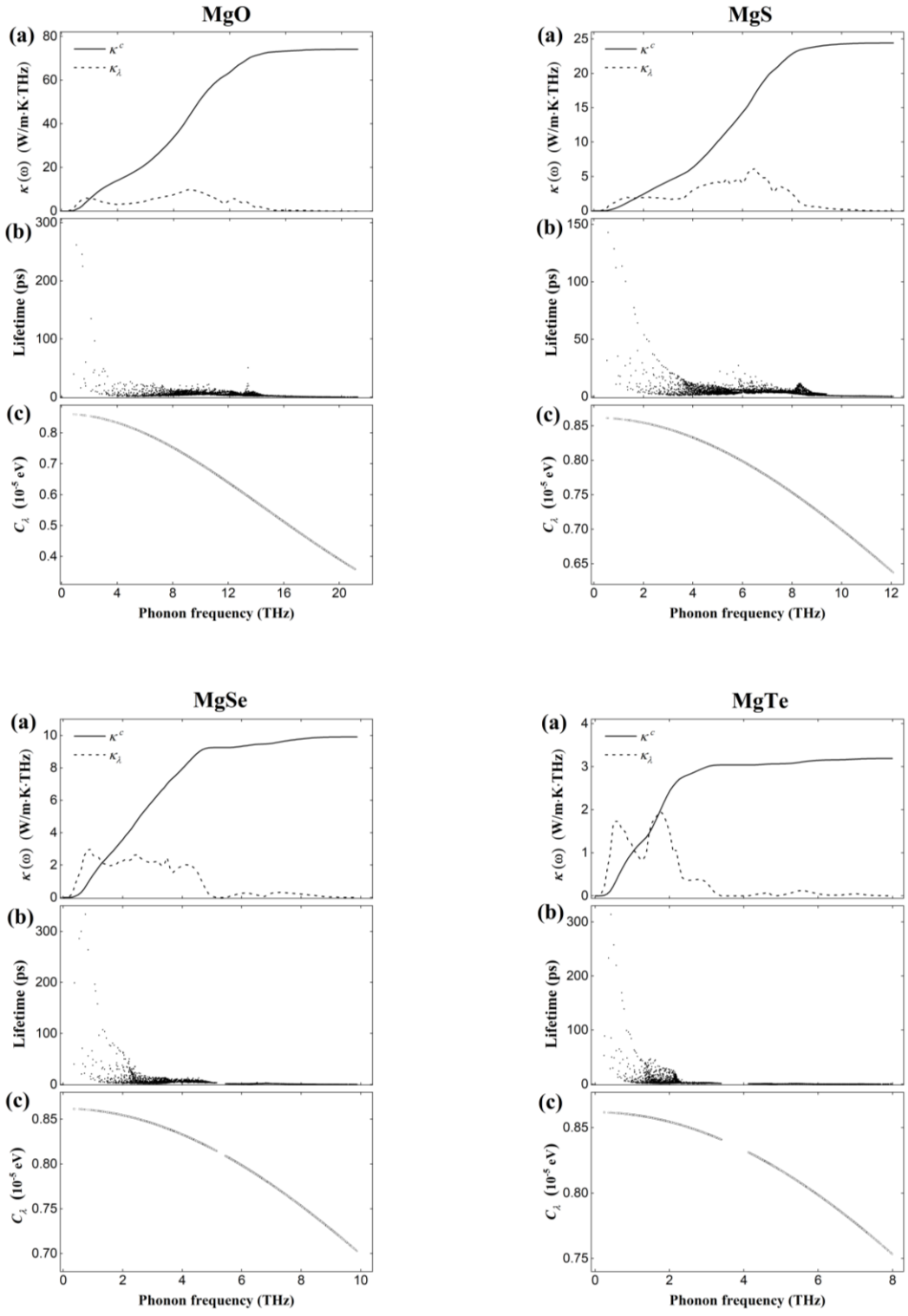

Figure 3.17. Thermodynamic properties of MgX (X = O, S, Se, Te) compounds. (a) Cumulative (solid black lines) and mode contributions (dashed black lines) of the calculated LTC values $\kappa(\omega)$ at 300 K, respectively. (b) Phonon lifetimes at 300 K. Each dot corresponds to a phonon mode sampled in the Brillouin zones. (c) Mode heat capacities at 300 K. Each circle corresponds to a phonon mode sampled in the Brillouin zones.

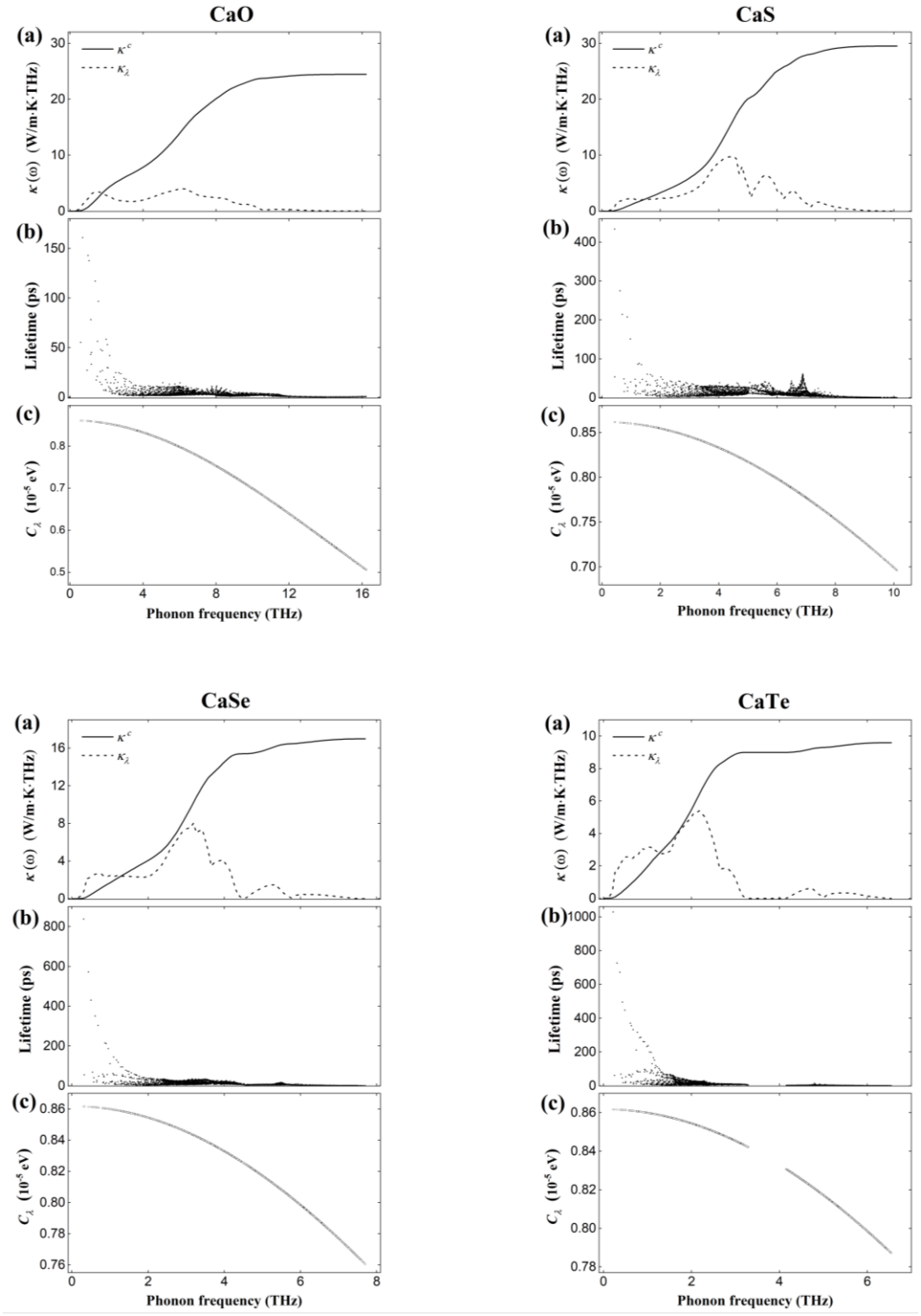

Figure 3.18. Thermodynamic properties of CaX (X = O, S, Se, Te) compounds. (a) Cumulative (solid black lines) and mode contributions (dashed black lines) of the calculated LTC values $\kappa(\omega)$ at 300 K, respectively. (b) Phonon lifetimes at 300 K. Each dot corresponds to a phonon mode sampled in the Brillouin zones. (c) Mode heat capacities at 300 K. Each circle corresponds to a phonon mode sampled in the Brillouin zones.

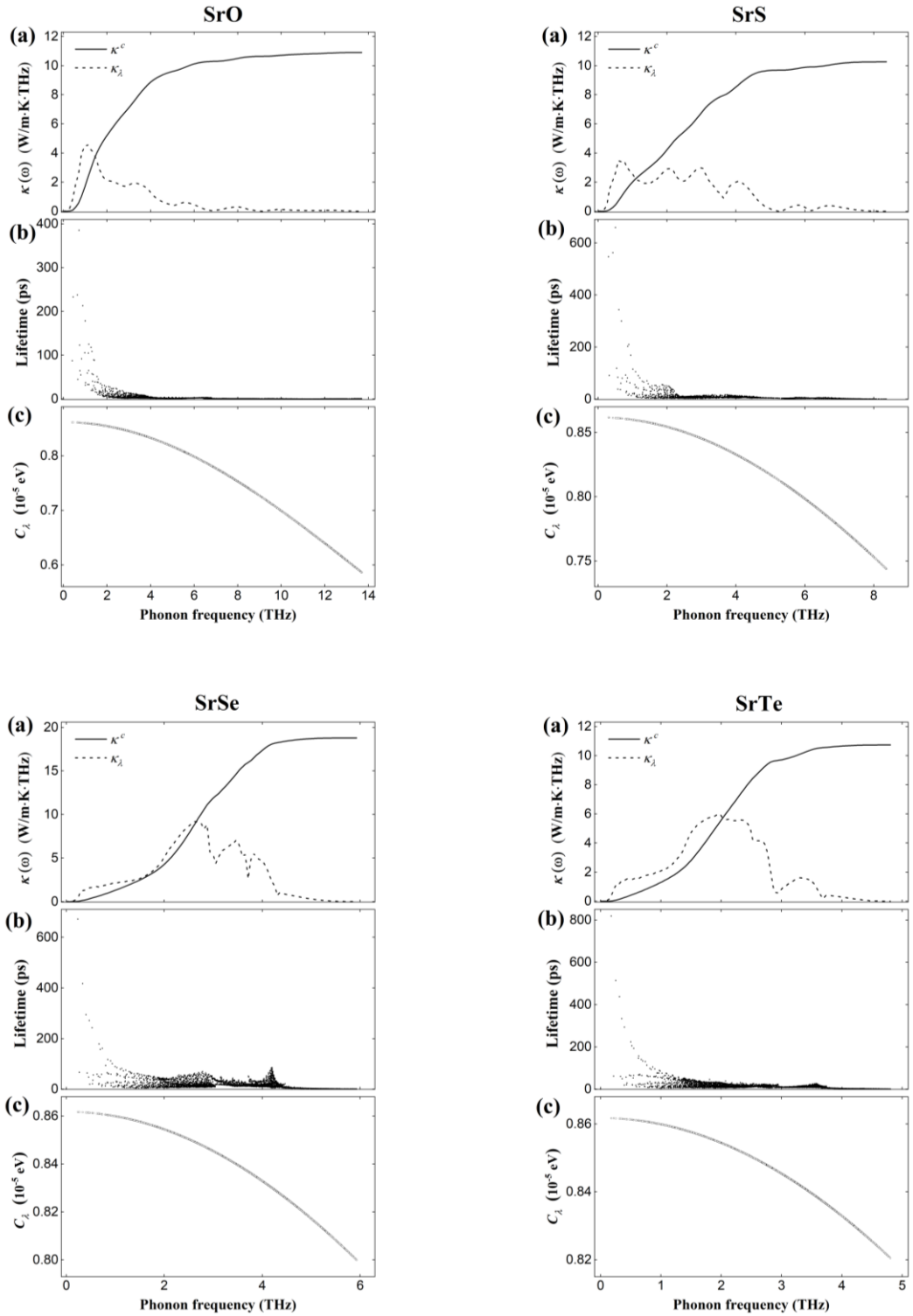

Figure 3.19. Thermodynamic properties of SrX (X = O, S, Se, Te) compounds. (a) Cumulative (solid black lines) and mode contributions (dashed black lines) of the calculated LTC values $\kappa(\omega)$ at 300 K, respectively. (b) Phonon lifetimes at 300 K. Each dot corresponds to a phonon mode sampled in the Brillouin zones. (c) Mode heat capacities at 300 K. Each circle corresponds to a phonon mode sampled in the Brillouin zones.

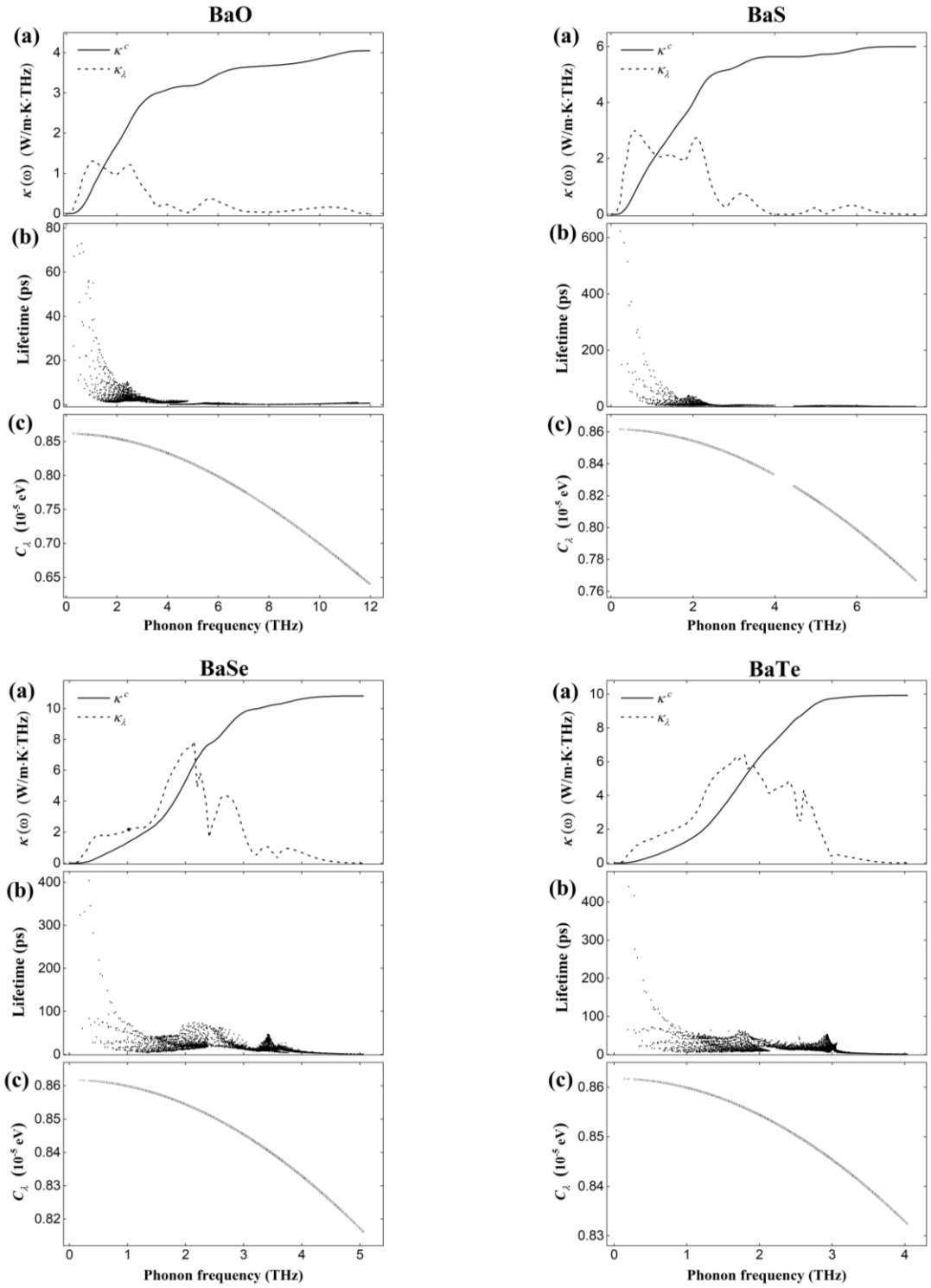

Figure 3.20. Thermodynamic properties of BaX (X = O, S, Se, Te) compounds. (a) Cumulative (solid black lines) and mode contributions (dashed black lines) of the calculated LTC values $\kappa(\omega)$ at 300 K, respectively. (b) Phonon lifetimes at 300 K. Each dot corresponds to a phonon mode sampled in the Brillouin zones. (c) Mode heat capacities at 300 K. Each circle corresponds to a phonon mode sampled in the Brillouin zones.

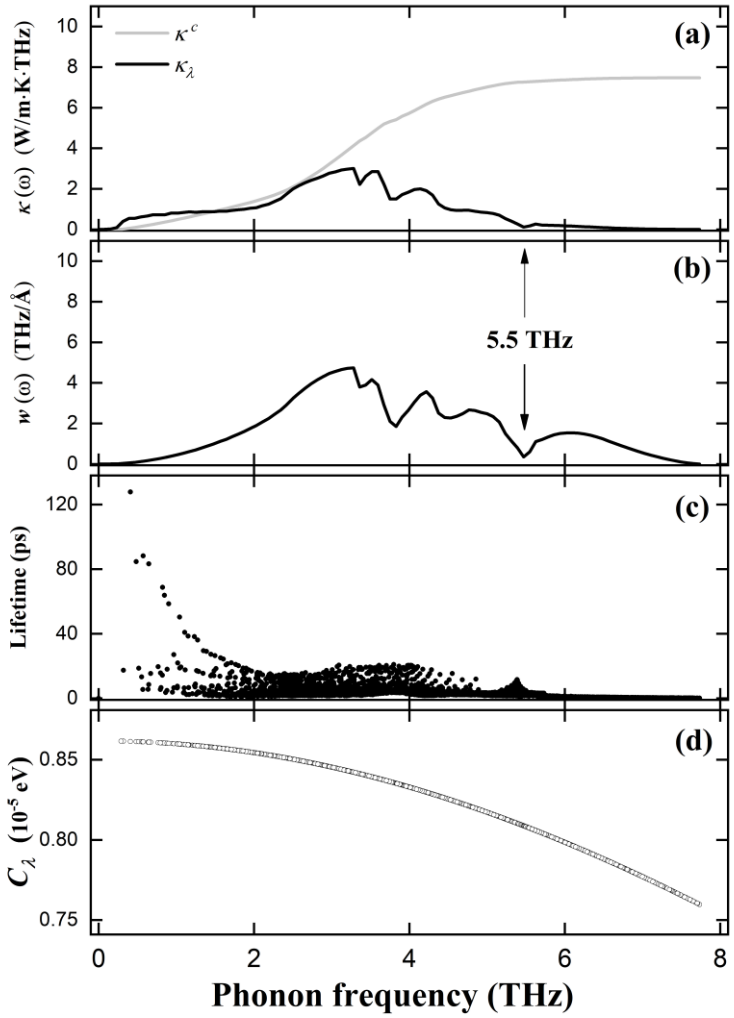

Figure 3.21. Thermodynamic properties of NaCl compound with respect to the phonon frequency at 300 K. (a) Cumulative (solid grey lines) and mode contributions (solid black lines) of the calculated LTC values $\kappa(\omega)$, respectively. (b) Distribution of the outer-product of the group velocities divided by primitive cell volume. (c) Phonon lifetime. Each dot corresponds to a phonon mode sampled in the Brillouin zones. (c) Mode heat capacity. Each circle corresponds to a phonon mode sampled in the Brillouin zones.

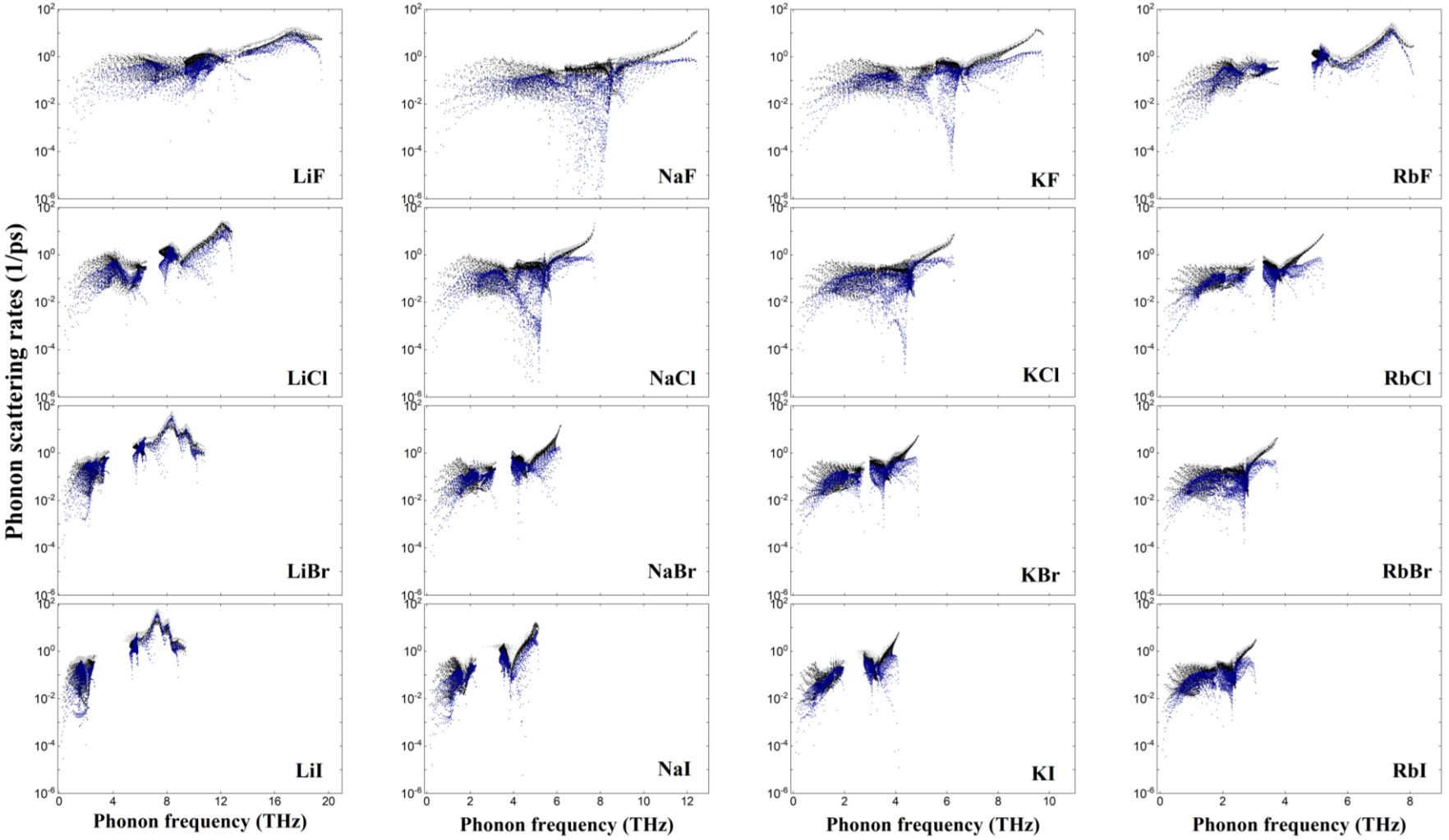

Figure. 3.22. Phonon scattering rates of MX (M = Li, Na, K, Rb; X = F, Cl, Br, I) compounds. Decomposed phonon scattering rates of the collision and the decay processes are denoted as black and blue dots, respectively. The total amount of phonon scattering rates of each phonon mode are denoted as grey dots.

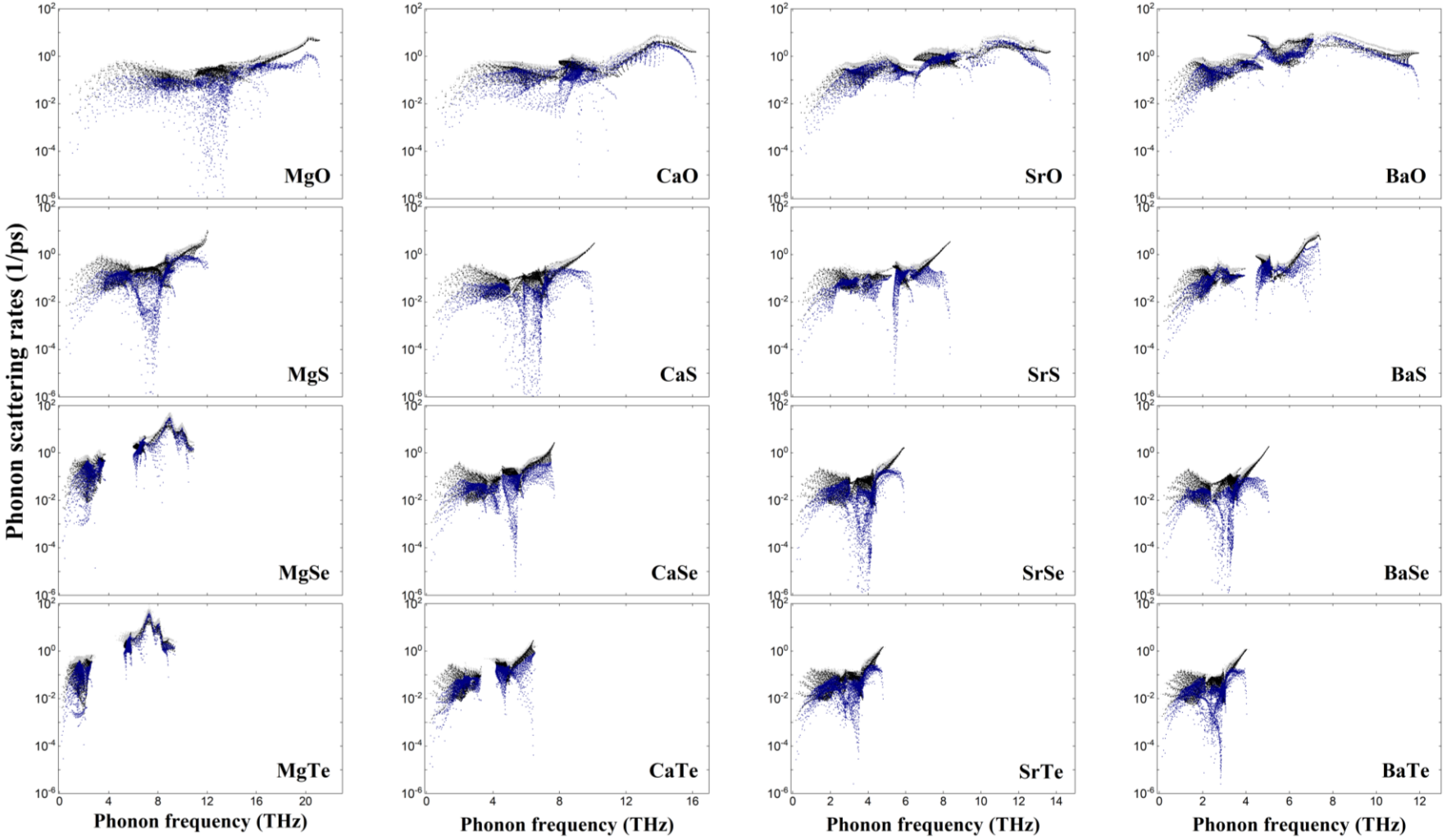

Figure. 3.23. Phonon scattering rates of MX (M = Mg, Ca, Sr, Ba; X = O, S, Se, Te) compounds. Decomposed phonon scattering rates of the collision and the decay processes are denoted as black and blue dots, respectively. The total amount of phonon scattering rates of each phonon mode are denoted as grey dots.

3.4 Conclusion

In this chapter, a series of calculations of lattice dynamics and thermal properties for the rocksalt-type compounds were conducted at finite temperatures based on our developed temperature-dependent phonon calculations. Firstly, taking NaCl compound as an example, all the potential factors may influence the calculations were carefully examined. Then, 32 rocksalt-type compounds were systematically investigated in detail by the first-principles based phonon calculations at room temperature, which give rise to the temperature dependence of the phonon band structures and densities of states. The phonon frequencies of phonon band structures at room temperature are dramatically different from that of 0 K, which can be attributed to the strong anharmonic effects in rocksalt structures.

Furthermore, the LTC values of all compounds were calculated by the SMRTA method and the LBTE method implemented within Phono3py framework, which the temperature effect was incorporated into the second- and third-order force constants. The detailed analyses of the phonon frequency dependencies of the phonon properties, such as the mode-contribution LTC, the mode heat capacity, the phonon lifetime and scattering rate were discussed, which demonstrated the relationship among these properties in the anharmonic rocksalt-type compounds. In addition, the LTC values computed by our improved first-principles anharmonic phonon calculations are accurate and in a better agreement with the measurements compared to other theoretical approaches in previous study.

In summary, the temperature-dependent phonon approach in present work provides a relatively simple and accurate way to compute the lattice anharmonic phonon and thermal transport properties at finite temperatures based on the first-principles phonon calculations instead of using the harmonic approximation where the breakdown may happen because of the strong anharmonicity. The application of this approach to a series of the rocksalt-type compounds shows useful information of the phonon band structures and LTC values. The good agreement between the calculated and experimental results demonstrates the validity of our developed approach and the universal applicability for studying the thermal properties of the materials.

Chapter 4

Lattice dynamics of cubic perovskite-type oxides ABO_3 (A = Ca, Sr, Ba; B = Ti, Zr, Hf)

4.1 Introduction

The perovskite oxides with a chemical formula ABO_3 have been extensively studied from both the experimental and theoretical viewpoints for a few decades. In perovskite-type oxide structure, A is the rare- or the alkaline-earth metal which have a coordination number of twelve, whereas the transition metal located at the B-site which have a coordination number of six. The configuration of cubic perovskite-type oxide ABO_3 is shown in figure 4.1. The A, B and O atoms are placed at the corner, body center and face center of a cubic lattice, respectively, which thereby forms the space group of $Pm\bar{3}m$. A large amount of the research of the perovskite materials focus on the applications to electronic, magnetic and energy-related devices owing to their unique piezoelectric, ferroelectric and optical properties. For example, the capacitors, ferroelectric and magnetic memories, photoelectric sensors and photovoltaics are the well-known popular utilizations of perovskite oxides. In addition, the perovskite oxides have a variety of the structural configurations. For instance, at ambient temperature and pressure, calcium titanate ($CaTiO_3$) has the orthorhombic structure and exhibits a phase sequence from orthorhombic to tetragonal and finally to high symmetry cubic structure with the increasing temperature of 1380 K, 1500 K and 1580 K, respectively [170]. Similar to $CaTiO_3$, barium titanate ($BaTiO_3$) also has a complicated phase diagram, where the symmetry changes from rhombohedral to orthorhombic to tetragonal and finally to cubic with the increasing temperature of 183 K, 278 K and 393 K, respectively [170]. The strontium titanate ($SrTiO_3$) is distinct from the above two compounds, which it undergoes a structural phase transition from the tetragonal structure with the low-symmetry to the cubic structure with the high-symmetry at about 105 K [124].

From the previous experimental and theoretical studies, it is found that the phase diagrams of the perovskite oxides are rich regarding different temperatures, which the ideal cubic structure is distorted due to many possible factors such as the rotations of octahedron, changes in atomic angles, defects and vacancies, and charge differences between A and B cations [121,122]. According to the lattice dynamical theory, when the structure is unstable the imaginary eigenvalues would be obtained as the solutions to the dynamical equation. The conventional method of the harmonic phonon calculations using the atomic forces computed through the density functional theory (DFT) and the finite displacement method breaks down when the target structure is unstable at a range of low temperatures, since the DFT calculations are defined as the computations for the electronic properties at 0 K. This is evidently manifested by the phonon band structures with occurred imaginary frequencies. Therefore, it is urgent to improve the current approaches of the phonon calculations by comprising the finite-temperature impact into the calculations. Once the tool of temperature-dependent phonon calculations is developed, the more accurate phonon properties including the temperature effects are acquired, which further improving the ability of predicting and evaluating the thermodynamic properties of the target structure.

Although much progress has been made in the experimental synthesis and characterization for the perovskite oxide compounds, the theoretical calculations of the thermodynamics are only accurate in the descriptions of the ground state properties, which impedes the sophisticated prediction of the phonon and thermal properties of these compounds. Only a few experimental and calculated data of the lattice thermal conductivity for the cubic perovskite structures are available in the related literatures. Hence, it is of great interest to study the lattice dynamics and thermal conductivities of these perovskite oxides at finite temperatures. In Chapter 4, the lattice dynamics investigations are given for the cubic perovskite-type oxides ABO_3 where cation A is and alkaline-earth metal Ca, Sr and Ba, and cation B is a tetravalent transition metal Ti, Zr and Hf. By performing the temperature-dependent phonon calculations based on the first principles phonon calculations introduced in Chapter 2, the well-converged phonon properties for all the stable compounds at both of the 300 K and 1000 K are obtained. The computational details used in the force and phonon calculations are introduced in section 4.2. Then, the phonon band structures and partial phonon densities of states of 300 K and 1000 K are plotted, respectively, and are compared with that of 0 K, in order to see the influence of the finite temperatures on their vibrational states at extreme high temperature. The vibrational phenomena for different compounds are analyzed and discussed in section 4.3. Furthermore, the lattice thermal conductivities of the compounds are calculated, whose cubic structure is dynamically stable without imaginary frequencies in phonon band structures at finite temperatures, and the changes with respect to the temperature are also presented in this section. Finally, a conclusion of the work in this chapter is presented.

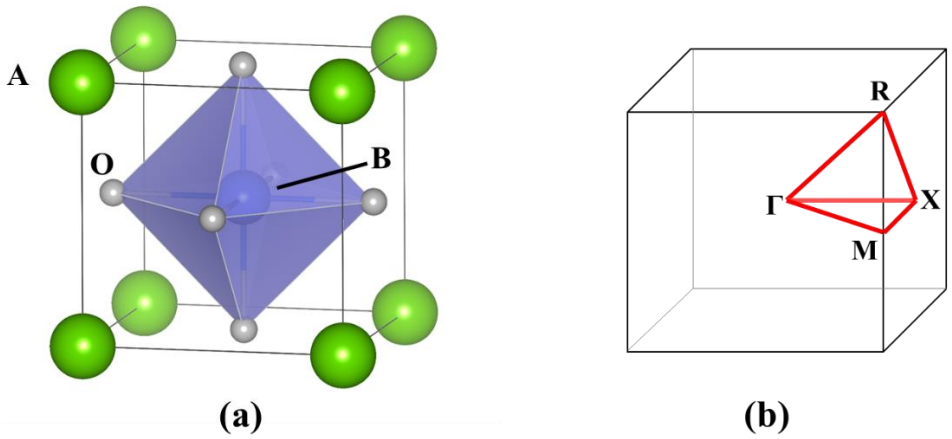

Figure 4.1. The crystal structure model of the cubic perovskite-type oxides ABO_3, where the A, B and O atoms are denoted as green, blue and grey balls, respectively.

4.2 Computational details

All of the first-principles calculations in the present work were performed within the framework of density functional theory using the projector-augmented wave (PAW) [142] potentials as implemented in Vienna *ab initio* simulation package (VASP) [127–130]. The generalized gradient approximation (GGA) [143,144] of Perdew, Burke, and Ernzerhof revised for solids (PBEsol) [145] was employed in the treatment of the exchange correlation functional because of its excellent performance to predict the lattice constants for a wide class of materials, which is important for the accuracy of the phonon calculations. In each force calculation, the total energy of each system was minimized until the energy difference between two consecutive electronic steps become less than 10^{-8} eV.

The compounds of the cubic ABO_3 structure were investigated, where the A and B elements were selected from Ca, Sr, Ba and Ti, Zr, Hf, respectively. All structures were constructed with 2 × 2 × 2 supercell size including 40 atoms, which was sufficient to obtain the accurate phonon band structures. It should be noticed that the lattice constant (see Table 4.1) of the each compound was optimized by DFT calculations using the exchange correlation functional of PBEsol due to the experimental data of most compounds at high temperature are not available. In addition, PBEsol functional has been widely used for well predicting the cell volume and phonon dispersion at 0 K. All the structures were fully relaxed until the Hellmann–Feynman force on each atom become less than 10^{-5} eV $Å^{-1}$. After evaluating the calculated parameters, the 500 eV kinetic energy cutoff was used for the plane-wave

basis set, the Brillouin zone was sampled by 2 × 2 × 2 *k*-point mesh centered at the Γ point generated by Monkhorts-Pack scheme.

The phonon calculations for all selected compounds at high temperature of 300 K and 1000 K were carried out as implemented in Phonopy package [9]. The effective harmonic force constants were computed self-consistently by a new set of 100 displaced configurations per iteration generated by the random displacements method. These iterative calculations would be stopped until the free energy convergence become less than 1 meV/atom, which leads to the well-converged phonon band structures and density of states. Considering the ionic polarization of the compounds, the non-analytical term correction to the harmonic dynamical matrix was included to treat the LO-TO splitting around the Γ point. The physical theory and technical details of the non-analytic correction have been discussed in section 3.2.4.

The lattice thermal conductivities of these compounds were calculated through Phonon3py package [40]. In present work, the second- and third-order force constants were estimated via ALM [77] interface in Phono3py from the force-displacement datasets after the temperature-dependent phonon calculations converged well. The lattice thermal conductivities were computed by solving the linearized phonon Boltzmann transport equation with single-mode relaxation time approximation (SMRTA), which are also compared with those obtained from the fully direct solutions of the linearized phonon Boltzmann transport equation (LBTE) and from experiments in previous studies. The *q*-point mesh of 28 × 28 × 28 sampled in Brillouin zone was set for the lattice thermal conductivity calculations of all the crystal compounds.

4.3 Results and discussion

The optimized lattice constants for 9 cubic perovskite-type oxides compounds are presented in table 4.1. Compared with the experimental values, the PBEsol indeed works remarkably well of predicting the lattice constants of the perovskite oxides. Here, the thermal expansion is not taken into account, since it has small effect on these compounds as temperature changes [171]. Additionally, most of their cubic phases are stable at the extremely high temperature close to 1000 K, which the correspondingly experimental data of the cubic phase are close to 1000 K.

Next, the phonon band structures at 0 and 1000 K for all these cubic structural compounds are plotted in figure 4.2. All these compounds except $BaHfO_3$ are dynamically unstable at 0 K. At 1000 K, only 4 compounds, i.e., $SrTiO_3$, $BaTiO_3$, $BaZrO_3$ and $BaHfO_3$, are dynamically stable without imaginary

frequencies. The compounds including calcium are not stable even at extremely high temperature. The phonon band structures in present work are in good agreement with previous theoretical results [172], except $SrHfO_3$ are dynamically unstable and stable at 1000 K in present and previous work, respectively, In fact, the experimental work [173] has been observed that the cubic phase exists at 1353 K, which our calculation of $SrHfO_3$ are consistent with this observation. It should be emphasized that there may exist a problem when calculating the thermal displacement matrix in Eqn. (2.67) since the negative value of σ^2 arises from the phonon modes with imaginary frequencies demonstrated in Eqn. (2.64). To deal with this problem, the imaginary eigenvalues are suggested to be fixed to an arbitrarily finite real value. In particular, those imaginary frequencies are treated as the corresponding absolute eigenvalues in this introduced approach. In addition, the phonon modes having absolute value smaller than the cutoff frequency of 0.01 THz are ignored here. In this way, the phonon frequencies are renormalized after some iterations and consequently a well-converged phonon dispersion without any imaginary frequencies can be obtained. Otherwise, if the structure is unstable at certain temperature, the imaginary frequencies will still exist in the results of the phonon band structures.

To understand the temperature dependencies of the phonon properties, the phono band structures and densities of states for the cubic $SrTiO_3$, $BaTiO_3$, $BaZrO_3$ and $BaHfO_3$ at 300 and 1000 K are computed. From figure 4.3, it is seen that lowest and highest phonon branches at 300 and 1000 K are mostly overlapped, whereas the lower frequencies especially at the high-symmetry points such as R, Γ and M point in Brillouin zone are hardening as the temperature increases. In addition, the first peak in phonon densities of states for each compound are slightly moved up, which is attributed to those hardening phonon branches. Taking cubic $SrTiO_3$ compound as an example, there are two apparent soft modes, which have been observed by previous experimental studies. One is arising from the antiferrodistortive (AFD) transition with the temperature lower than 105 K, which results in the cubic high symmetry changing to the tetragonal low symmetry by rotating the neighboring oxygen octahedra in opposite directions [125,126]. From the phonon band structures, this soft mode is centered at R point in the Brillouin zone, namely R_{25}. Apart from the R_{25} soft mode, it is found that another soft mode appears at Γ point in the Brillouin zone, namely Γ_{15}, which is associated with the loss of the ferroelectricity. By using temperature-dependent approach, both of these two soft modes existing at ground state disappear with elevated temperature. The available experimental measurements of the phonon frequencies for $SrTiO_3$ are also presented as a comparison with the calculated phonon band structures. It is seen that Γ_{15} branch is overestimated whereas R_{25} branch is slightly underestimated by the calculations. These small discrepancies maybe caused by the lattice constants, the exchange correlation functionals, and the measurement errors. Generally, the calculated phonon band structure is in a quite good agreement with the available measurements, which demonstrated that the temperature-dependent approach is applicable to the perovskite oxides for obtaining the well-converged stable phonon band structures.

As mentioned in the introduction (section 4.1), in the conventional phonon calculations of the LTC, the lowest-order anharmonicity is considered as a perturbation to the harmonic potential. In this assumption, the LTC must be calculated when the harmonic phonon frequencies are completely stable without any imaginary frequencies. Thus, it is inaccessible to the LTC of $SrTiO_3$, $BaTiO_3$, $BaZrO_3$ and $BaHfO_3$ at 300 and 1000 K, since the imaginary frequencies appear in their phonon band structures at 0 K. By using the temperature-dependent approach, the renormalized phonon frequencies of each compounds at finite temperatures are obtained, which thereby can be further used to calculate their LTC values. The calculated LTC values are presented in table 4.2. It is found that the calculated LTC values in this work are in consistent match with the experimental LTC data. For $BaZrO_3$ and $BaHfO_3$ compounds at 300 K, although the LTC values are relatively overestimated by the calculations, they are still in the same order of magnitude. Compared with the LTC values calculated by QSCAILD approach in previous study, the overall results of this work except $BaZrO_3$ and $BaHfO_3$ at 300 K are in better agreement with measurements. Therefore, the temperature-dependent approach is significant for the LTC calculations of a given structure with a stable phase at finite temperatures whereas it is dynamically unstable at ground state.

Finally, the calculated LTC values with respect to the temperature for $SrTiO_3$ are illustrated in figure 4.4 (a). It is clearly seen that the calculated LTC values in this work are systematically lower than the previously experimental data [174,175]. Although the discrepancy of the LTC between the calculation and the measurements are about 3 W/(m·K), the temperature dependence index of the LTC $\alpha = 0.7$ in $\kappa \propto T^{-\alpha}$ in the present study is in a satisfactory agreement with that of the experimental data. According to the previous studies [172], the LTC values of the cubic perovskites generally decrease more slowly than $\kappa \propto T^{-1}$ at high temperatures while that of Si and Ge decreases more quickly than the same model. The behavior of the present temperature-dependent LTC results is consistent with the those in references [76,77,172].

Furthermore, the mode-contribution of LTC $\kappa(\omega)$, the outer product of group velocity $w(\omega)$ and the lifetimes for $SrTiO_3$ at different temperatures with respect to the phonon frequency are shown in figure 4.4 (b)-(d). The major contributions to the LTC values are TO modes whereas the highest-frequency LO modes have almost no impact on the LTC. When the phonon frequencies are lower than 5 THz, the corresponding phonon modes have relatively larger lifetimes, which decrease rapidly as the phonon frequencies increase. Between 5 THz and 10 THz, $\kappa(\omega)$ are mainly influenced by $w(\omega)$ and lifetimes when the phonon frequencies are lower and higher than around 7 THz, respectively. Besides, it is apparent that as the temperature increases, $\kappa(\omega)$, $w(\omega)$ and the lifetimes become lower, which thus the LTC value become lower. Hence, by deeply investigating $SrTiO_3$ compound, the temperature-dependent phonon approach introduced in this work is demonstrated to be accurate for predicting the

LTC calculations at finite temperatures, which is expected to be applied on more perovskite compounds and even other different structures.

Table 4.1. Lattice constants of 9 cubic perovskite-type oxides compounds optimized by exchange correlation functional of PBEsol. The experimental data are also presented.

Compounds	This work (Å)	Expt. (Å)
$CaTiO_3$	3.848	3.890
$CaZrO_3$	4.100	4.138
$CaHfO_3$	4.062	3.990
$SrTiO_3$	3.899	3.905
$SrZrO_3$	4.134	4.140
$SrHfO_3$	4.096	4.060
$BaTiO_3$	3.986	3.996
$BaZrO_3$	4.191	4.194
$BaHfO_3$	4.155	4.170

Table 4.2. Calculated LTC values (in unit of W/m-K) at 300 K and 1000 K of 9 cubic perovskite-type oxides compounds. The available experimental [173,174,176–178] and other theoretical [172] values are also presented in this table. Some measurements in parentheses represent those structures are not in cubic phase.

Compounds	300 K	Calc.	Expt.	1000 K	Calc.	Expt.
$CaTiO_3$	-	-	-	-	-	-
$CaZrO_3$	-	-	-	-	-	-
$CaHfO_3$	-	-	-	-	-	-
$SrTiO_3$	7.95	6.44	10.5	3.95	2.36	4.0
$SrZrO_3$	-	-	-	-	-	-
$SrHfO_3$	-	-	(5.2)	-	2.20	(2.7)
$BaTiO_3$	5.07	4.99	(4 – 5)	2.95	2.51	-
$BaZrO_3$	8.10	5.61	5.2	3.39	2.13	2.9
$BaHfO_3$	11.91	8.26	10.4	4.48	3.04	4.5

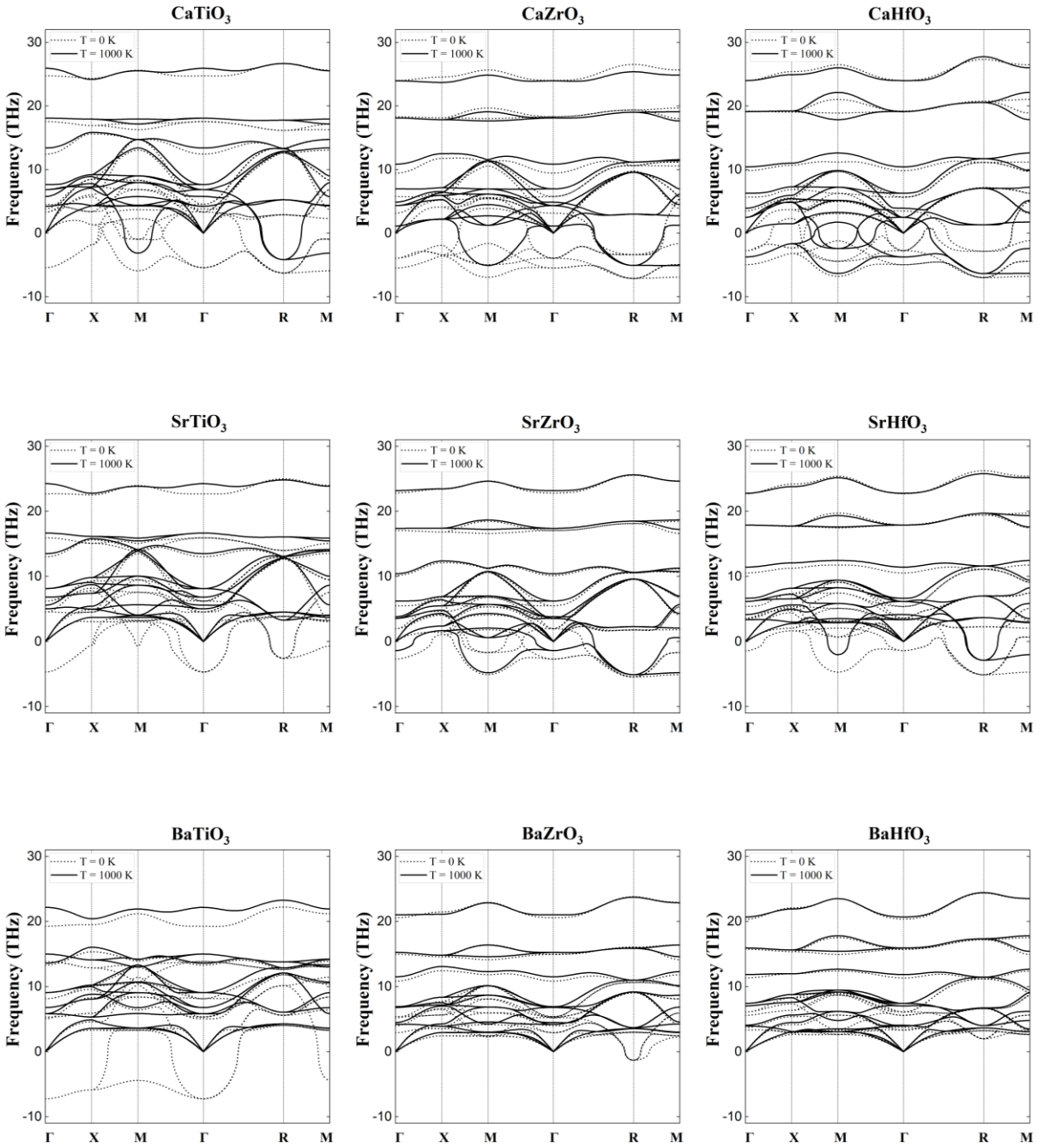

Figure 4.2. Phonon band structures of 9 cubic perovskite-type oxides ABO_3 (A = Ca, Sr, Ba; B = Ti, Zr, Hf) compounds. The phonon band structures at 0 and 1000 K are denoted as solid and dashed black lines, respectively.

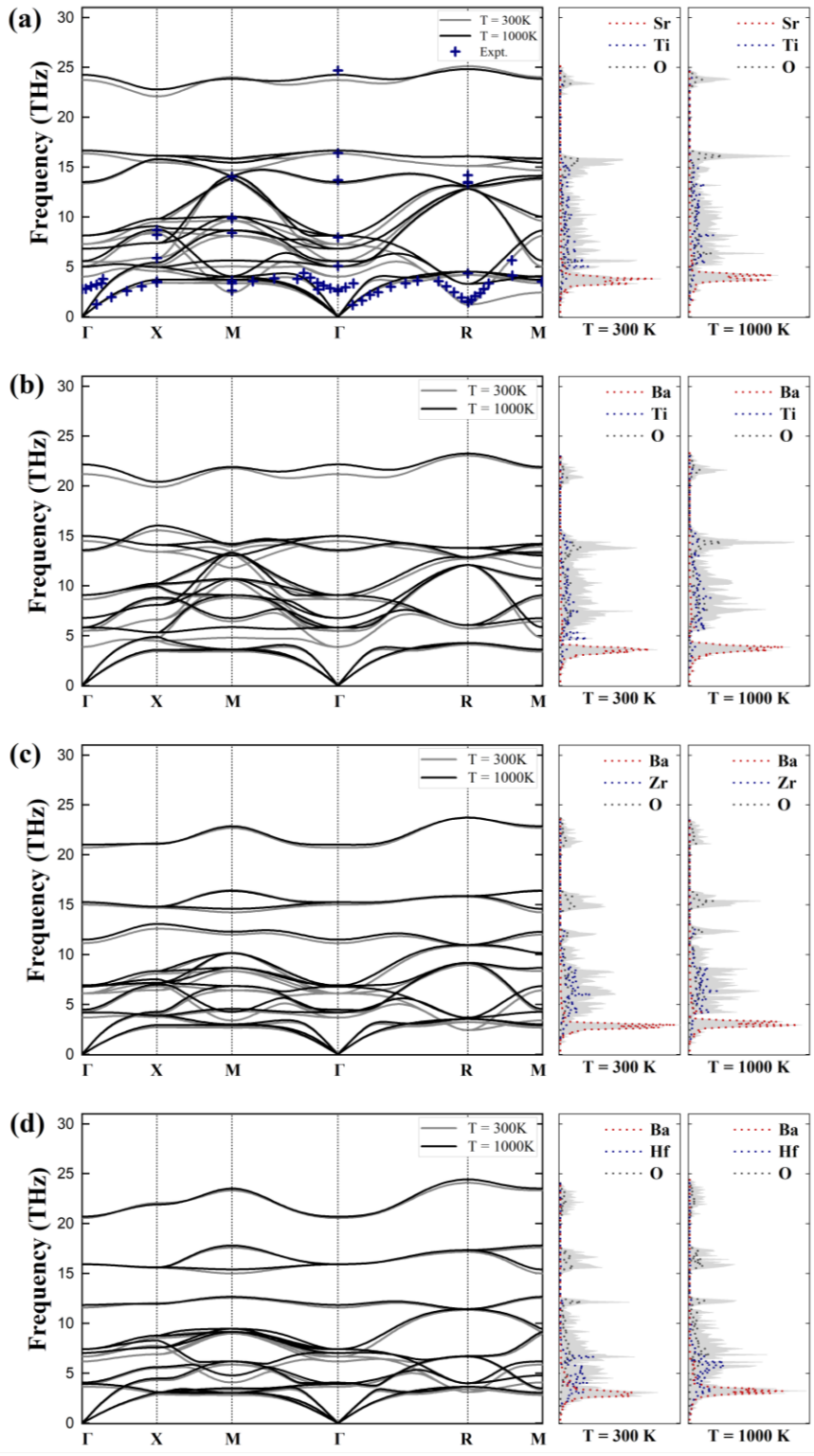

Figure 4.3. Phonon band structures and phonon densities of states (PDOS) of the cubic (a) $SrTiO_3$, (b) $BaTiO_3$, (c) $BaZrO_3$ and (d) $BaHfO_3$. The phonon band structures of 300 and 1000 K are denoted as grey and black solid lines, respectively. In PDOS, contributions of A, B and O atoms of each compound to the total PDOS (shaded area) are denoted as dashed red, blue and black dashed lines, respectively.

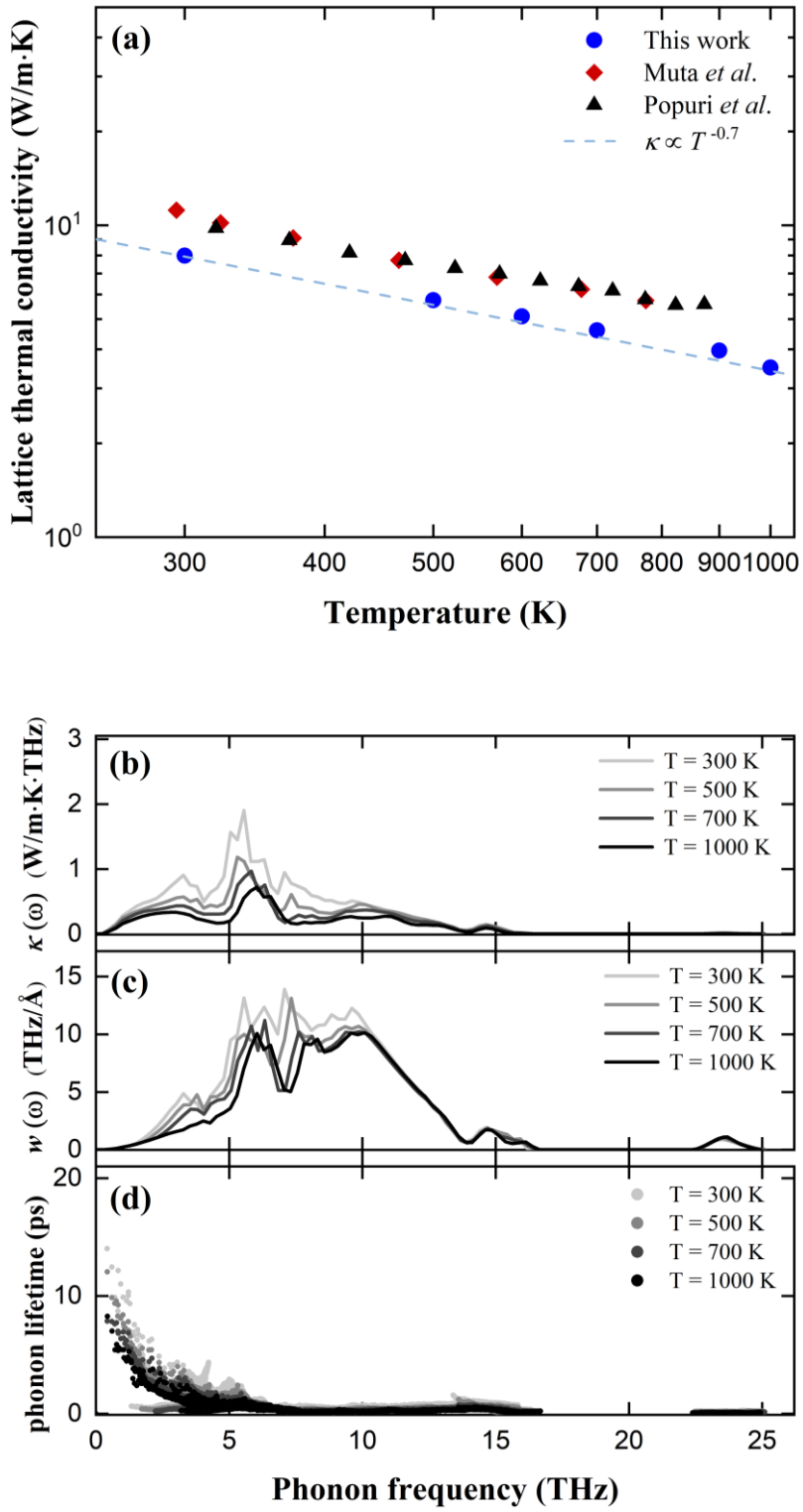

Figure 4.4. Temperature dependence of the (a) calculated lattice thermal conductivities (blue circles), (b) mode-contribution of LTC, (c) outer product of the group velocities and (d) phonon lifetimes with respect to the temperature for the cubic $SrTiO_3$. The experimental (red diamonds and black triangles) data are also presented for comparison. The dashed grey and blue lines represent the model of $\kappa \propto T^{-\alpha}$ where $\alpha = 0.7$.

4.4 Conclusion

In this chapter, the lattice dynamics of the cubic perovskite-type oxides ABO_3 compounds have been systematically investigated where A and B cations are selected from Ca, Sr, Ba and Ti, Zr, Hf, respectively. In particular, it is interested to explore the thermodynamic properties of these compounds whose the given phases are dynamically stable at finite temperatures while they are unstable at the 0 K. By using the temperature-dependent phonon approach, the phonon frequencies including the temperature information are renormalized iteratively, which consequently the self-consistent phonon band structures and densities of states are obtained. For some of the compounds dynamically unstable at 0 K through the harmonic phonon calculations, it is found that their structure are dynamically stable by incorporating the temperature effect, and thereby the imaginary frequencies in the phonon band structures vanish.

Based on the well-converged and stable phonon properties at finite temperatures, the lattice thermal conductivities then can be calculated using anharmonic phonon calculations including the three-phonon interactions. Compared with the previously experimental and theoretical data, the LTC values calculated in present work show a quite good agreement with references, which thus the proposed approach is proved to be valid on predicting the related thermal properties for the perovskite-type oxides structure. In conclusion, this temperature-dependent phonon approach is certified to be sufficient enough for the cubic perovskite oxides at the high temperatures. It overcomes the limitations arising from the conventional phonon calculations that cannot compute the LTC without the completely dynamically stable harmonic phonon band structures, which is expected to be universally applicable to the a wide of the perovskite-type compounds for a high-throughput estimation of their thermodynamics properties at finite temperatures.

Chapter 5

General conclusion

In this thesis, the temperature-dependent phonon approach based on the first-principles phonon calculations is introduced and demonstrated from the perspective of the background of the theory and methodology, and the applications to some different types of the structures, i.e., the rocksalt-type and perovskite-type compounds.

In Chapter 2, the background and evolution of the lattice dynamical calculations based on the first-principles calculations are introduced, which are stem from the solution to the single-particle Kohn–Sham equations in quantum mechanics. The theory of the lattice dynamics are elaborated including some approximations such as the harmonic and quasiharmonic approximations, and the thermodynamic and heat transfer phenomena such as the thermal expansion and lattice thermal conductivity. Then, the evolution of the temperature-dependent phonon methods in previous studies are discussed, especially the SCP-related approaches where the phonon frequencies are renormalized iteratively for incorporating the anharomonic effect. Furthermore, the introduced phonon approach is demonstrated by its physical theory and numerical process. The workflow of this approach is explicitly exhibited combing the VASP, Phonopy and ALM packages for the force calculations, phonon calculations and fitting of the effective harmonic force constants, respectively. The effective force constants are fitted to the force-displacement datasets in each iteration where the atomic displacements are generated by the random displacements with the canonical ensemble. After some iterations, the corresponding phonon band structures are self-consistent at the given temperature, which consequently the related thermodynamic properties are obtained.

In Chapter 3, the application of the temperature-dependent phonon approach to the rocksalt-type compounds are shown in order to test the validity and applicability of this present method. The calculations of 32 rocksalt-type compounds including the alkali halides and the alkaline earth chalcogenides consisted of the group I-VII and II-VI, respectively, are conducted by using the proposed approach. To test the robustness and precision of the phonon calculations, different choices of the

different factors such as the lattice parameters and exchange correlation functionals that may influence the results are urgent to be examined. After the determination of all calculated parameters, the phonon band structures and densities of states and the lattice thermal conductivities of all these rocksalt-type compounds are predicted by the phonon calculations beyond harmonic approximation. In particular, the calculated lattice thermal conductivities for these rocksalt-type compounds are discussed through the frequency dependence of the mode-contribution of the lattice thermal conductivities and the phonon lifetimes, which are generated by the anharmonic phonon-phonon interactions. It is found a good agreement between the calculated results and available experimental data, which identifies the validity of the temperature dependence of the phonon calculations. The analyses of the high-throughput phonon band structures and LTC values provide a deep insight to investigate systematically the phonon and thermal transport properties of the materials, which verifies that the temperature-dependent phonon approach offers a powerful and fundamental guidance for experiment to explore more and more new thermal materials with desired properties.

In Chapter 4, the temperature-dependent phonon calculations are performed on the cubic perovskite-type oxides ABO_3 compounds where the cation A and B are alkaline earth (Ca, Sr, Ba) and transition metals (Ti, Zr, Hf)), respectively. Taking strontium titanate ($SrTiO_3$) as an example, it undergoes a structural phase transition from the low-symmetry tetragonal structure to the high-symmetry cubic structure at about 105 K. However, the imaginary frequencies appear in the phonon band structures of its cubic phase by the harmonic phonon calculations, which is consequently inaccessible to the lattice thermal conductivity due to the dynamically unstable phonon properties. The breakdown of the harmonic phonon calculations impede the accurate description of the finite-temperature phonon properties, and the evaluation of the performance of the thermal properties such as the lattice thermal conductivity. In addition, the comprehensive evaluation of the thermal performance is highly demanded. Therefore, it is crucial to systematically investigate the LTC for the perovskite-type oxides, which in turn can be a useful guidance for the future experiment. By using the temperature-dependent phonon calculations, the phonon band structures of some cubic perovskite oxides such as $SrTiO_3$ at finite temperatures are dynamically stable without any softening modes. Furthermore, the experimentally comparable LTC values for those dynamically stable ABO_3 compounds are also obtained owing to the accurate descriptions of the phonon interactions involving the well-converged second- and third-order force constants. The good match between calculated and measured phonon band structures and LTC values demonstrate the necessity of the inclusion of the temperature effect for the perovskite-type oxides compounds. Moreover, the temperature-dependent phonon approach introduced in this work is certified to be powerful for predicting the thermodynamics properties of the perovskite structures.

In conclusion, the temperature-dependent phonon approach is significant for future phonon calculations. For those highly anharmonic crystals the harmonic and quasiharmonic approximations are insufficient to describe the phonon states, which may lead to a large discrepancy of the dynamical or thermal transport properties between the measurements and calculations. Furthermore, it is found that the conventional phonon calculations fail to accurately describe the phonon interactions for some compounds at high temperatures. These crystals with a finite-temperature structural phase are dynamically unstable at 0 K manifested by the appearance of the imaginary frequencies in phonon band structures, for which it should be considered with the temperature effect. In this way, it is impossible to access to the dynamical properties depended on the phonon scattering events such as the phonon lifetime and lattice thermal conductivity. Both of the above two issues can be dealt with the temperature-dependent phonon approach introduced in this work in spite of some limitations exist such as the computational cost and only the lowest-order phonon-phonon couplings included. Overall, it is expected to be a powerful numerical way for predicting the thermodynamic properties, which are useful for exploring more advanced materials with desired thermal properties in future materials scientific research.

References

[1] D. C. Rapaport, *The Art of Molecular Dynamics Simulation* (Cambridge University Press, 2004).

[2] J. M. Dickey and A. Paskin, Phys. Rev. **188**, 1407 (1969).

[3] B. J. Alder and T. E. Wainwright, J. Chem. Phys. **31**, 459 (1959).

[4] P. Hohenberg and W. Kohn, Phys. Rev. **136**, B864 (1964).

[5] W. Kohn and L. J. Sham, Phys. Rev. **140**, A1133 (1965).

[6] J. Kohanoff, *Electronic Structure Calculations for Solids and Molecules: Theory and Computational Methods* (Cambridge University Press, 2006).

[7] D. Vasileska and S. M. Goodnick, Mater. Sci. Eng. R Reports **38**, 181 (2002).

[8] I. Žutić, J. Fabian, and S. Das Sarma, Rev. Mod. Phys. **76**, 323 (2004).

[9] A. Togo and I. Tanaka, Scr. Mater. **108**, 1 (2015).

[10] M. Born and K. Huang, *Dynamical Theory of Crystal Lattices* (Clarendon Press, 1954).

[11] J. M. Ziman, *Electrons and Phonons: The Theory of Transport Phenomena in Solids* (Oxford University Press, 2001).

[12] A. Togo and I. Tanaka, Phys. Rev. B **87**, 184104 (2013).

[13] A. Togo, F. Oba, and I. Tanaka, Phys. Rev. B **78**, 134106 (2008).

[14] A. Togo, F. Oba, and I. Tanaka, Phys. Rev. B **77**, 184101 (2008).

[15] A. Togo *et al.*, Phys. Rev. B **81**, 174301 (2010).

[16] Y. Tamada *et al.*, Phys. Rev. B **81**, 132302 (2010).

[17] A. Seko *et al.*, Phys. Rev. B **72**, 24107 (2005).

[18] A. Matsumoto *et al.*, Phys. Rev. B **83**, 214110 (2011).

[19] N. J. Lane *et al.*, Phys. Rev. B **86**, 214301 (2012).

[20] H. Akamatsu *et al.*, Phys. Rev. Lett. **112**, 187602 (2014).

[21] Y. Ikeda *et al.*, Phys. Rev. B **90**, 134106 (2014).

[22] R. A. Cowley, Reports Prog. Phys. **31**, 123 (1968).

[23] P. Nath *et al.*, Comput. Mater. Sci. **125**, 82 (2016).

[24] A. Otero-de-la-Roza and V. Luaña, Phys. Rev. B **84**, 24109 (2011).

[25] D. Wee *et al.*, J. Electron. Mater. **41**, 977 (2012).

[26] S. Xiang *et al.*, Phys. Rev. B **81**, 14301 (2010).

[27] D. Orlikowski, P. Söderlind, and J. A. Moriarty, Phys. Rev. B **74**, 54109 (2006).

[28] B. Grabowski *et al.*, Phys. Rev. B **79**, 134106 (2009).

[29] A. Ward *et al.*, Phys. Rev. B **80**, 125203 (2009).

[30] A. Ward and D. A. Broido, Phys. Rev. B **77**, 245328 (2008).

[31] A. Ward and D. A. Broido, Phys. Rev. B **81**, 85205 (2010).

[32] Z. Tian *et al.*, Phys. Rev. B **85**, 184303 (2012).

[33] J. Shiomi, K. Esfarjani, and G. Chen, Phys. Rev. B **84**, 104302 (2011).

[34] L. Lindsay, D. A. Broido, and N. Mingo, Phys. Rev. B **82**, 115427 (2010).

[35] W. Li and N. Mingo, Phys. Rev. B **90**, 94302 (2014).

[36] K. Esfarjani, G. Chen, and H. T. Stokes, Phys. Rev. B **84**, 85204 (2011).

[37] L. Chaput *et al.*, Phys. Rev. B **84**, 94302 (2011).

[38] D. A. Broido *et al.*, Appl. Phys. Lett. **91**, 231922 (2007).

[39] T. Tadano, Y. Gohda, and S. Tsuneyuki, Phys. Rev. Lett. **114**, 95501 (2015).

[40] A. Togo, L. Chaput, and I. Tanaka, Phys. Rev. B **91**, 94306 (2015).

[41] M. Zeraati *et al.*, Phys. Rev. B **93**, 85424 (2016).

[42] R. Bianco *et al.*, Phys. Rev. B **96**, 14111 (2017).

[43] O. Delaire *et al.*, Nat. Mater. **10**, 614 (2011).

[44] I. Errea, Eur. Phys. J. B **89**, 237 (2016).

[45] I. Errea, M. Calandra, and F. Mauri, Phys. Rev. B **89**, 64302 (2014).

[46] I. Errea *et al.*, Nature **532**, 81 (2016).

[47] I. Errea *et al.*, Phys. Rev. Lett. **114**, 157004 (2015).

[48] M. Leroux *et al.*, Phys. Rev. B **92**, 140303 (2015).

[49] B. Monserrat, N. D. Drummond, and R. J. Needs, Phys. Rev. B **87**, 144302 (2013).

[50] B. Rousseau and A. Bergara, Phys. Rev. B **82**, 104504 (2010).

[51] A. Debernardi, S. Baroni, and E. Molinari, Phys. Rev. Lett. **75**, 1819 (1995).

[52] A. A. Maradudin and A. E. Fein, Phys. Rev. **128**, 2589 (1962).

[53] S. Narasimhan and D. Vanderbilt, Phys. Rev. B **43**, 4541 (1991).

[54] S. Baroni *et al.*, Rev. Mod. Phys. **73**, 515 (2001).

[55] C. Z. Wang, C. T. Chan, and K. M. Ho, Phys. Rev. B **42**, 11276 (1990).

[56] N. de Koker, Phys. Rev. Lett. **103**, 125902 (2009).

[57] O. Hellman, I. A. Abrikosov, and S. I. Simak, Phys. Rev. B **84**, 180301 (2011).

[58] O. Hellman *et al.*, Phys. Rev. B **87**, 104111 (2013).

[59] M. P. Ljungberg and J. Íñiguez, Phys. Rev. Lett. **110**, 105503 (2013).

[60] I. B. Magdău and G. J. Ackland, Phys. Rev. B **87**, 174110 (2013).

[61] D.-B. Zhang, T. Sun, and R. M. Wentzcovitch, Phys. Rev. Lett. **112**, 58501 (2014).

[62] P. Souvatzis *et al.*, Phys. Rev. Lett. **100**, 95901 (2008).

[63] P. Souvatzis and S. P. Rudin, Phys. Rev. B **78**, 184304 (2008).

[64] A. van Roekeghem, J. Carrete, and N. Mingo, Phys. Rev. B **94**, 20303 (2016).

[65] B. M, *Fest. Akad. D. Wiss. Göttingen, Math. Phys. Klasse* (Springer, 1951).

[66] D. J. Hooton, Philos. Mag. A J. Theor. Exp. Appl. Phys. **3**, 49 (1958).

[67] T. R. Koehler, Phys. Rev. Lett. **17**, 89 (1966).

[68] T. R. Koehler, Phys. Rev. Lett. **18**, 654 (1967).

[69] T. R. Koehler, Phys. Rev. **165**, 942 (1968).

[70] O. Hellman and I. A. Abrikosov, Phys. Rev. B **88**, 144301 (2013).

[71] O. Hellman and D. A. Broido, Phys. Rev. B **90**, 134309 (2014).

[72] A. H. Romero *et al.*, Phys. Rev. B **91**, 214310 (2015).

[73] N. Shulumba *et al.*, Phys. Rev. Lett. **117**, 205502 (2016).

[74] N. Shulumba, O. Hellman, and A. J. Minnich, Phys. Rev. B **95**, 14302 (2017).

[75] I. Errea, M. Calandra, and F. Mauri, Phys. status solidi **251**, 2556 (2014).

[76] T. Tadano and S. Tsuneyuki, Phys. Rev. B **92**, 54301 (2015).

[77] T. Tadano and S. Tsuneyuki, J. Phys. Soc. Japan **87**, 41015 (2018).

[78] F. Zhou *et al.*, Phys. Rev. Lett. **113**, 185501 (2014).

[79] F. Zhou *et al.*, Phys. Rev. B **100**, 184308 (2019).

[80] F. Zhou *et al.*, Phys. Rev. B **100**, 184309 (2019).

[81] N. Bonini *et al.*, Phys. Rev. Lett. **99**, 176802 (2007).

[82] T. Feng and X. Ruan, Phys. Rev. B **93**, 45202 (2016).

[83] T. Tadano and S. Tsuneyuki, Phys. Rev. Lett. **120**, 105901 (2018).

[84] Y. Xia and M. K. Y. Chan, Appl. Phys. Lett. **113**, 193902 (2018).

[85] T. Feng and X. Ruan, Phys. Rev. B **97**, 45202 (2018).

[86] X. Yang *et al.*, Phys. Rev. B **100**, 245203 (2019).

[87] X. Gu *et al.*, Phys. Rev. B **100**, 64306 (2019).

[88] M. Puligheddu *et al.*, Phys. Rev. Mater. **3**, 85401 (2019).

[89] D. W. Jepsen and R. F. Wallis, Phys. Rev. **125**, 1496 (1962).

[90] I. P. Ipatova, A. A. Maradudin, and R. F. Wallis, Phys. Rev. **155**, 882 (1967).

[91] M. Balkanski, R. F. Wallis, and E. Haro, Phys. Rev. B **28**, 1928 (1983).

[92] G. Lang *et al.*, Phys. Rev. B **59**, 6182 (1999).

[93] J. E. Eby, K. J. Teegarden, and D. B. Dutton, Phys. Rev. **116**, 1099 (1959).

[94] M. F. Merriam, R. Smoluchowski, and D. A. Wiegand, Phys. Rev. **125**, 65 (1962).

[95] R. F. Wood, Phys. Rev. Lett. **15**, 449 (1965).

[96] E. R. Cowley, R. A. Cowley, and W. Cochran, Proc. R. Soc. London. Ser. A. Math. Phys. Sci. **287**, 259 (1965).

[97] E. R. Cowley, R. A. Cowley, and W. Cochran, Proc. R. Soc. London. Ser. A. Math. Phys. Sci. **292**, 209 (1966).

[98] M. S. Hybertsen and S. G. Louie, Phys. Rev. B **32**, 7005 (1985).

[99] J. R. Chelikowsky, Phys. Rev. B **34**, 5295 (1986).

[100] S.-G. Lee and K. J. Chang, Phys. Rev. B **52**, 1918 (1995).

[101] G. K. Wertheim *et al.*, Phys. Rev. B **51**, 13675 (1995).

[102] H. Tatewaki, Phys. Rev. B **60**, 3777 (1999).

[103] G. Q. Lin, H. Gong, and P. Wu, Phys. Rev. B **71**, 85203 (2005).

[104] E. Bousquet, N. A. Spaldin, and P. Ghosez, Phys. Rev. Lett. **104**, 37601 (2010).

[105] M. A. Zwijnenburg and S. T. Bromley, Phys. Rev. B **83**, 24104 (2011).

[106] Y. Hinuma *et al.*, Phys. Rev. Mater. **2**, 124603 (2018).

[107] D. Zakiryanov, M. Kobelev, and N. Tkachev, Fluid Phase Equilib. **506**, 112369 (2020).

[108] M. Häfner and T. Bredow, Phys. Rev. B **102**, 184108 (2020).

[109] N. K. Ravichandran and D. Broido, Phys. Rev. B **98**, 085205 (2018).

[110] Y. Xia *et al.*, Phys. Rev. X **10**, 041029 (2020).

[111] M. S. Dresselhaus *et al.*, Adv. Mater. **19**, 1043 (2007).

[112] D. J. Singh and I. Terasaki, Nat. Mater. **7**, 616 (2008).

[113] G. J. Snyder and E. S. Toberer, Nat. Mater. **7**, 105 (2008).

[114] T. Feng, L. Lindsay, and X. Ruan, Phys. Rev. B **96**, 161201 (2017).

[115] J. Suntivich *et al.*, Science (80-.). **334**, 1383 (2011).

[116] M. A. Green, A. Ho-Baillie, and H. J. Snaith, Nat. Photonics **8**, 506 (2014).

[117] S. Ghosh, D. Di Sante, and A. Stroppa, J. Phys. Chem. Lett. **6**, 4553 (2015).

[118] J. F. Schooley, W. R. Hosler, and M. L. Cohen, Phys. Rev. Lett. **12**, 474 (1964).

[119] I. Grinberg *et al.*, Nature **503**, 509 (2013).

[120] A. K. Tomar *et al.*, Coord. Chem. Rev. **431**, 213680 (2021).

[121] H. Thomas and K. A. Müller, Phys. Rev. Lett. **21**, 1256 (1968).

[122] R. J. Angel, J. Zhao, and N. L. Ross, Phys. Rev. Lett. **95**, 25503 (2005).

[123] Y. Luspin, J. L. Servoin, and F. Gervais, J. Phys. C Solid State Phys. **13**, 3761 (1980).

[124] K. A. Müller and H. Burkard, Phys. Rev. B **19**, 3593 (1979).

[125] R. A. Cowley, Phys. Rev. **134**, A981 (1964).

[126] G. Shirane and Y. Yamada, Phys. Rev. **177**, 858 (1969).

[127] G. Kresse and J. Hafner, Phys. Rev. B **47**, 558 (1993).

[128] G. Kresse and J. Hafner, Phys. Rev. B **49**, 14251 (1994).

[129] G. Kresse and J. Furthmüller, Comput. Mater. Sci. **6**, 15 (1996).

[130] G. Kresse and J. Furthmüller, Phys. Rev. B **54**, 11169 (1996).

[131] N. W. Ashcroft and N. D. Mermin, *Solid State Physics* (Holt, Rinehart and Winston, New York London, 1976).

[132] E. Kaxiras, *Atomic and Electronic Structure of Solids* (Cambridge University Press, 2003).

[133] G. P. Srivastava, *The Physics of Phonos* (Routledge, 1990).

[134] D. C. Wallace, *Thermodynamics of Crystals* (Dover, New York, 1998).

[135] L. Chaput, Phys. Rev. Lett. **110**, 265506 (2013).

[136] A. van Roekeghem, J. Carrete, and N. Mingo, Comput. Phys. Commun. **263**, 107945 (2021).

[137] A. Togo, Phonopy, https://github.com/phonopy/phonopy (n.d.).

[138] K. Parlinski, Z. Q. Li, and Y. Kawazoe, Phys. Rev. Lett. **78**, 4063 (1997).

[139] G. Kresse, J. Furthmüller, and J. Hafner, Europhys. Lett. **32**, 729 (1995).

[140] T. Tadano, ALM, https//github.com/ttadano/ALM (n.d.).

[141] Y. Wang *et al.*, J. Phys. Condens. Matter **22**, 202201 (2010).

[142] P. E. Blöchl, Phys. Rev. B **50**, 17953 (1994).

[143] J. P. Perdew, K. Burke, and Y. Wang, Phys. Rev. B **54**, 16533 (1996).

[144] J. P. Perdew, K. Burke, and M. Ernzerhof, Phys. Rev. Lett. **77**, 3865 (1996).

[145] J. P. Perdew *et al.*, Phys. Rev. Lett. **100**, 136406 (2008).

[146] A. P. Mills and W. S. Crane, Phys. Rev. B **31**, 3988 (1985).

[147] J. R. Hardy and A. M. Karo, Phys. Rev. B **26**, 3327 (1982).

[148] A. M. Karo, J. Chem. Phys. **31**, 1489 (1959).

[149] Y. Ekinci and J. P. Toennies, Surf. Sci. **563**, 127 (2004).

[150] S. Duman *et al.*, Phys. Rev. B **73**, 205201 (2006).

[151] G. Kalpana, B. Palanivel, and M. Rajagopalan, Phys. Rev. B **50**, 12318 (1994).

[152] T. Yamamoto and T. Mizoguchi, Ceram. Int. **39**, S287 (2013).

[153] Z. Charifi *et al.*, J. Phys. Condens. Matter **17**, 4083 (2005).

[154] M. Souadkia *et al.*, Comput. Mater. Sci. **50**, 1701 (2011).

[155] A. S. Verma, Phys. status solidi **246**, 345 (2009).

[156] G. Raunio, L. Almqvist, and R. Stedman, Phys. Rev. **178**, 1496 (1969).

[157] J. F. Nye, *Physical Properties of Crystals: Their Representation by Tensors and Matrices* (Oxford University Press, 1985).

[158] W. Cochran and R. A. Cowley, J. Phys. Chem. Solids **23**, 447 (1962).

[159] A. H. MacDonald, S. H. Vosko, and P. T. Coleridge, J. Phys. C Solid State Phys. **12**, 2991 (1979).

[160] R. M. Pick, M. H. Cohen, and R. M. Martin, Phys. Rev. B **1**, 910 (1970).

[161] P. Giannozzi *et al.*, Phys. Rev. B **43**, 7231 (1991).

[162] X. Gonze and C. Lee, Phys. Rev. B **55**, 10355 (1997).

[163] X. Wu, D. Vanderbilt, and D. R. Hamann, Phys. Rev. B **72**, 35105 (2005).

[164] M. Gajdoš *et al.*, Phys. Rev. B **73**, 45112 (2006).

[165] K. K. Srivastava and H. D. Merchant, J. Phys. Chem. Solids **34**, 2069 (1973).

[166] E. R. Cowley, J. Phys. C Solid State Phys. **5**, 1345 (1972).

[167] S. Pettersson, J. Phys. Condens. Matter **1**, 361 (1989).

[168] C. Toher *et al.*, Phys. Rev. B **90**, 174107 (2014).

[169] A. Seko *et al.*, Phys. Rev. Lett. **115**, 205901 (2015).

[170] V. V Lemanov *et al.*, Solid State Commun. **110**, 611 (1999).

[171] A. Okazaki and M. Kawaminami, Mater. Res. Bull. **8**, 545 (1973).

[172] A. van Roekeghem *et al.*, Phys. Rev. X **6**, 41061 (2016).

[173] B. J. Kennedy, C. J. Howard, and B. C. Chakoumakos, Phys. Rev. B **60**, 2972 (1999).

[174] H. Muta, K. Kurosaki, and S. Yamanaka, J. Alloys Compd. **392**, 306 (2005).

[175] S. R. Popuri *et al.*, RSC Adv. **4**, 33720 (2014).

[176] S. Yamanaka *et al.*, J. Alloys Compd. **359**, 1 (2003).

[177] T. Maekawa, K. Kurosaki, and S. Yamanaka, J. Alloys Compd. **407**, 44 (2006).

[178] M. Tachibana, T. Kolodiazhnyi, and E. Takayama-Muromachi, Appl. Phys. Lett. **93**, 92902 (2008).

Acknowledgement

The author would like to express her heartfelt gratitude and appreciation to Professor Isao Tanaka at Kyoto University for continuous guidance, support and encouragement throughout the three years of research and life, helping the author successfully fulfill her dream of Ph.D. study. The author would also like to express her deep gratitude to Dr. Atsushi Togo for continuous discussion and helpful advices on research work. The author wishes to express her deep gratitude to Professor Hiroyuki Nakamura and Professor Hideyuki Yasuda for carefully reading this dissertation and offering suggestion.

The author acknowledges Associate Professor Atsuto Seko and Assistant Professor Hiroyuki Hayashi for their productive advice on the research work. The author also greatly appreciates the kindness of Ms. Makiko Orita for the management of the research activities, the daily communications and the suggestion, which are very helpful for a foreigner student living and studying abroad. The author appreciates the interesting discussion with Keiyu Mizokami and Kohei Shinohara during the doctoral course. The author would like to express her sincerely thanks to the whole Tanaka research group and to the Kyoto University for offering the great research environment.

Finally, the author would like to express her gratefully acknowledgement to the financial support from China Scholarship Council (CSC), sponsoring the author for her life and study abroad. The author would also like to express her deepest appreciation to her family for enduring support, encouragement and love.